University of Alberta

Femtosecond Laser based X-ray Sources and their Applications in Phase Contrast Imaging

by

Atif Ali

A thesis submitted to the Faculty of Graduate Studies and Research in partial fulfillment of the requirements for the degree of

Master of Science
in
Photonics and plasmas

Department of Electrical and Computer Engineering

Spring 2010
Edmonton, Alberta

Examining Committee

Dr. Robert Fedosejevs, Electrical and Computer Engineering

Dr. Ying Tsui, Electrical and Computer Engineering

Dr. Wojciech Rozmus, Physics

Abstract

The focus of this dissertation is to study the keV X-ray emission from different Z material to develop compact, quasi-continuous tabletop K_α sources for the application of in-line phase contrast imaging, X-ray diffraction experiments and X-ray microscopy. The emission occurs from plasma produced by focusing 120 fs, 800 nm and 300 μJ Ti:Sapphire laser pulses up to an intensity of few times 10^{16} W/cm^2 on Cu, Fe and Ag metal targets. The main interest of these experiments is to characterize the fast electrons and X-ray emission from the laser plasma interaction. The investigation of X-ray emission energy and spectral characteristics is carried out by employing three detector systems which include filtered pin-diode, Charge Coupled Device and CdTe pulse height detectors. Scaling of photon flux as a function of incident laser energy is measured and related to the dynamics and absorption mechanisms involved in laser matter interaction.

Specifically the construction and evaluation of K_α X-ray sources operated at 1 kHz repetition rate is reported with a photon flux of ~ 7×10^9 photon/s, 3×10^9 photon/s and 1.4×10^7 photon/s around the K_α line for Cu, Fe and Ag respectively. These K_α fluences correspond to energy conversion efficiencies of around $\eta_{Cu} = 3\times10^{-5}$, $\eta_{Fe} = 1.06\times10^{-5}$ and $\eta_{Ag} = 2\times10^{-7}$. The Cu and Fe K_α X-ray sources are applied to thin biological specimens and low atomic number (Z) materials to record in-line phase contrast images. It is demonstrated that the laser based K_α

sources can serve as alternative sources for conventional X-ray radiography of biological samples in clinical applications.

Dedicated

to

My

Late Grand Father and Mother
Their sacrifices make this possible

I Love you and miss u a lot

Acknowledgements

First of all I would like to express my gratitude to my advisor Prof. Robert Fedosejeves for giving me an opportunity to join Laser Plasma interaction research group. The experimental work done in this dissertation was only a dream without his guidance, teachings, profound and far-reaching ideas in the filed of laser and plasmas. I am also grateful to Prof. Ying Tsui for his support, contribution and valuable discussions.

I would like to thank Dr. Juzer Ali Chakera and Dr. Henry Tiedje, without their technical, experimental and data analysis skills this thesis would not have come to conclusion. I am also obliged to Blair Harwood for his enthusiastic and invaluable support to maintain laser in a good condition for the experiments. In particular, I would like to acknowledge my lab fellows particularly, Lei Pan and Yogesh Godwal for their help and valuable discussion in experiments and data analysis.

In addition I would like to acknowledge my friends, particularly Nauman Tehsin, G. Mustafa, and Hyder to encourage and support me during all the memorable moments.

I wish to honor my grandfather Kareem Busk, grandmother Bakhshai bibi, father Muhammad Ali, Mother Aziza, Sweet sisters Rabia, Sadaf, Aasma, Mehvish, Saima, Sadia, Uzma, Huma, Mani, and Brothers Wasif, Waqar and Umer Farooq for their unconditional love and support. The completion of this work was not possible without their continued encouragement in happy and especially in grief (loss of my grand parents) moments of my life.

Finally, I wish to thank my fiancée, for her love, care and motivation to complete this work.

Table of Contents

List of Figures

List of Tables

Chapter 1 Introduction

Since the discovery of X-rays by C. Rontgen in 1895, X-ray emission has become a valuable tool for many applications. Different X-ray sources (conventional X-ray tubes and synchrotron sources) have been developed to study the X-ray diffraction patterns from materials which is used to analyze the structure of crystalline solids with atomic distance measurement resolution and high imaging resolution. X-ray based research has become as one of the major fields in the physics [1], chemistry [2] and biology [3].

The interaction of focused laser pulses with matter provide a way to create a hot dense plasma in front of matter, which can be characterized and optimized for a variety of applications e.g inertial confinement fusion (ICF), X-ray sources, X-ray lasers etc. Laser produced X-rays are in turn an important diagnostic to study the physics and scaling of hot electron and K_α X-ray generation in the non-relativistic (10^{16} W/cm^2) and fully relativistic (>10^{18} W/cm^2) interaction regimes, which still need to be explored in detail. Experiments have shown significant progress towards a better understanding of laser mater interactions [4] and K_α emission [5]. X-ray yield is directly related to electron density scale length, the electron energy distribution function and the effects of target preheating have been measured using K_α radiation [6, 7, 8]. The rapid growth in laser technology

has opened new horizons with the advent of ultrafast high intensity laser pulses. Compact laser systems based on the chirped pulse amplification (CPA) technique have the capability to deliver ultra-short pulses, which can be focused up to 10^{16}-10^{20} W/cm^2. These intense laser pulses can be focused onto solid targets to generate ultra-short duration hot electrons bunches and characteristic radiation. When ultrashort pulses strike metal surfaces they rapidly ionize the target surface and create very steep density gradient plasma with negligible expansion during the interaction. Suprathermal (kinetic energy much greater than plasma temperature) electrons produced in this interaction stream back and penetrate into the solid to produce continuous bremsstrahlung emission and characteristic X-ray radiation. Key advantage of these X-ray sources is that they are of small size, wide spectral range and short pulse duration i.e. X-ray pulse duration is approximately comparable to the duration of the laser pulse. These features of laser based X-ray sources make them suitable for improved imaging quality and time resolved studies of molecular and phase transition processes. Laser produced X-rays also have an advantage due to reduced expense and ease of maintenance compared to ultra short hard X-rays pulses produced by synchrotron sources, which require a large facility and are expensive to operate. Hard x-rays generated from laser plasmas is an economical alternative to huge synchrotron facilities. The energy range of X-rays from laser produced plasmas varies from less than a keV (soft X-rays) to MeV (hard X-rays). The hard X-rays are due to the contribution

of suprathermal (hot) electrons generated in the ultrafast and ultrahigh intensity interactions.

The processes of phase transitions and chemical reactions in matter happen on a timescale corresponding to one vibrational period, which is typically of the order of 10^{-13}s (100 fs) [5]. One way to study this dynamic behaviour of matter is to use temporal resolution smaller than 100 fs and with probes that can to resolve the lattice spacing. However typical Synchrotron radiation sources are too long (tens of picosecond) to investigate time resolved X-ray diffraction experiments. Thus they mainly have been used to analyze biological samples. These experiments demonstrate multipicosecond to nanosecond time resolution but many experiments indicate that initial structure changes are within tens or hundreds of femtoseconds [9]. The ideal way to study such structural changes in matter is with femtosecond X-rays emitted from laser plasma interactions. Such laser based sources will offer an alternative to new femtosecond FEL laser sources which are just now becoming available at DESY and Stanford [10, 11, 12, 13].

Recently, new laser based X-ray sources that can generate X-ray pulses with duration of a few picoseconds (10^{-12} s) down to femtosecond (10^{-15} s) level have been developed with the advent of chirped pulse amplification technique. These laser produced plasma X-ray sources are widely used in number of applications such as X-ray nanolithography [14], Extended X-ray absorption fine structure [15], microscopy [16], time resolved X-ray diffraction and phase contrast

imaging [17, 18, 19]. Moreover study of X-ray and hot electron generation from laser produced plasma is very important to understand ICF target design and hard X-ray imaging of plasma is used as one of the basic diagnostics in fusion studies.

The main goal of this thesis is to develop a laser based X-ray source operating at kilohertz repetition rate. These tabletop femtosecond lasers have the capability to provide sufficiently small (micron size) K_α sources which can then be used for applications in X-ray microscopy and phase contrast imaging. This technique can provide superior resolution in the image which is not visible in conventional absorption imaging and even more so for a weakly absorbing samples.

Experiments have been successfully reported to generate K_α radiation sources from different metal targets using laser pulse energy from few tens to hundreds of mJ and repetition rate of 10 Hz [18, 19]. Using such laser conversion efficiency into characteristic radiation of 10^{-5} to 10^{-4} has been observed into 2π sr. These sources have been employed for successful imaging of test and biological samples. As these lasers have traditionally used high pulse energy, they are more prone to frequent optical damage and thus high maintenance and operating cost. The high pulse energy restricts their operation to less than the order of 100 Hz or so. Furthermore, the large pulse energy generates more continuum bremsstrahlung emission, which is not as suitable for medical imaging as stated above. On the other hand, a laser based source based on a small pulse energy, can be more durable, quasi-cw in output and low in continuum emission, but they are generally lower in x-ray conversion efficiency [20, 21, 22, 23]. If high X-ray conversion

efficiencies similar to that of a multi-mJ laser pulses can be achieved using smaller energy laser pulses then such sources will be very useful for the above application. Recently, we have demonstrated a kHz, 130 fs Ti:Sapphire laser based Cu-K_α source produced by sub-mJ laser pulses [24]. The X-ray conversion using sub-millijoule laser based Cu-K_α X-ray emission [17, 24] has started to approach that using the multi mJ laser pulses [25, 26, 27]. The higher conversion efficiency was achieved by optimizing the laser intensity and pre-pulse on the solid copper target [24, 28]. However, this source was limited in operating time to few tens of minutes due to limited supply of fresh solid target surface for the laser firing at kHz repetition rate. In this dissertation we have focused on investigating an operating kHz X-ray source based on a Cu-wire target, which can be continuously feed through a spool eliminating the limitation on operating time. The source has a similar higher conversion of $4x10^{-5}$ consistent with our earlier result. Using this source we have demonstrated X-ray phase contrast imaging of test samples confirming the source coherence properties and sufficient X-ray flux. In addition other metal targets including Fe and Ag have been characterized in the same geometry. The source has been put to use for few hours continuously. To our knowledge this would be the first sub-mJ laser based X-ray source which has been used in phase contrast imaging and has the potential to realize as a compact durable X-ray source for clinical imaging application.

Chapter 2 Background Theory

The physics involved in this work is based on ultrashort intense laser interaction with solids and plasmas. The investigation of these physical phenomena including K_α line emission and hot electron measurements from different metal targets using high repetition laser pulses is reported in Chapter 4. The experimental techniques and details are presented in chapter 3. Basic theory related to these interaction effects is discussed in the present chapter, which includes basic plasma physics concepts along with absorption processes important in intense laser fields. The table-top laser systems based on the chirped pulse amplification (CPA) [29] technique had made it possible to generate ultrashort X-ray pulses from solid, gases [4] and liquid jets [30]. These femtosecond lasers with peak power from the terawatt to petawatt range are now available and one can focus these light pulses up to intensities greater than 10^{21} W/cm^2. This new advancement in technology has given the opportunity to explore the behavior of matter under this powerful and intense light interaction regime. The basic principle of femtosecond laser interaction with solid density matter along with hard X-rays emission due to line and bremsstrahlung processes in the light of various absorption mechanisms will be discussed in this chapter.

2.1 Basic Plasma parameters and Laser plasma interaction

Plasma also called fourth state of matter is defined as a highly ionized gas consists of free electrons and ions interacting with each other via electromagnetic potentials and exhibiting quasi-neutrality and collective behavior. Electron density and temperature are two conventional parameters to describe plasma characteristics and plasma temperature is directly expressed in terms of eV, an energy equivalent of the temperature with the Boltzmann constant $K_{BeV}T$ where $K_B = 8.617 \times 10^{-5}$ eV/K. The other important basic parameters used to characterize the plasma are Debye length λ_D and plasma frequency ω_P. The Debye length is defined by

$$\lambda_D = \left(\varepsilon_\circ K_B T_e / n_e e^2\right)^{1/2} \tag{2.1}$$

Where ε_o is the permittivity of free space, K_B is the Boltzmann constant, T_e is the electron temperature, n_e is the electron density and e is the elementary charge. The Debye length provides a measurement of range beyond which the electric field of a single charge is shielded by the surrounding charges. This implies that one needs to consider the effects and collisions of individual particle on spatial scales shorter than λ_D. In order to reach qausi-neutrality and collective behavior, the Debye length must be smaller than or equal to the dimension of plasma and there must exist a large numbers of charge species in the Debye sphere (a sphere given by the Debye radius) for shielding. These two basic conditions for plasma are: i)

$\lambda_D << L$, ii) $N_D = 4/3\ (\pi\lambda^3_D n_e) >> 1$ where L is the dimension of the plasma and N_D is the number of electrons in Debye sphere.

Due to charge quasi-neutrality collective behavior exists in plasmas, where any electron fluctuation creates a non-equilibrium state in which a restoring electric field is generated proportional to displacement. If the disturbing agent is laser light the electrons oscillate within plasma leading to a dispersion relation given by

$$\omega_L = \omega_p + k_L^2 c^2 \tag{2.2}$$

Where ω_L and k_L are the angular frequency and wave vector of the laser light and c is the speed of light in vacuum. When perturbed and released the motion of electrons creates electrostatic oscillations at a frequency ω_p which is dependent on the density of electron n_e within the plasma.

$$\omega_P = \left(e^2 n_e / \varepsilon_o m_e\right)^{1/2} \tag{2.3}$$

This characteristic frequency is called the plasma frequency (ω_P). This is the resonance frequency of plasma in which electrons oscillate about their equilibrium position. It is an important plasma parameter the inverse of which also describes the timescale in which plasma electrons respond to disturbances.

In the case of laser solid interaction, the leading edge of the laser pulse creates a pre-plasma on the surface which a gradually increases in density towards the solid. This interaction of laser pulses with solid targets depends on the temporal

contrast and for a better understanding of the electron density gradient profile it is important to have good knowledge of long and short pulse interaction physics. If electromagnetic wave (EM) has a frequency $\omega_L > \omega_P$, then the EM wave can penetrate easily into the plasma because the electric field associated with the EM wave oscillates rapidly compared to the response of plasma electrons. This state of plasma is known as underdense plasma. In the opposite case of $\omega_L < \omega_P$ the electrons within the plasma respond rapidly to cancel the disturbances and prohibit the EM wave from propagating further. This state is said to be overdense plasma. There is also a condition when the plasma frequency becomes equal to the laser frequency $\omega_L = \omega_P$ at this point in the plasma there is a resonant response and no EM wave can propagate beyond this point. This point is defined as the critical density n_{cr}.

$$n_{cr} = \omega_L \varepsilon_o m_e / e^2 = \frac{1.11 \times 10^{21}}{\lambda_L^2 (\mu m)} [cm^{-3}] \qquad (2.4)$$

At this density the plasma electrons are driven to large resonant oscillations by the incoming EM wave and cause reflection of laser light from the overdense plasma region $(n_e > n_{cr})$. Laser absorption is a complex process but in a very simplified manner maximum energy transfer from laser pulses to the plasma occurs when the density of plasma electrons become equal to the critical density. Beyond this critical layer no further propagation of laser pulses is possible. The critical density

is a function of wavelength, so that shorter wavelength radiation has the capability to propagate deeper into plasma than longer wavelength pulses.

The interaction physics of long (nanosecond) and short (femtoseond) laser pulses with metal targets is substantially different in various aspects. For ultra-short laser pulse expansion of the plasma is limited due to the quick transfer of laser energy into the plasma and limited time for plasma expansion. A typical density scalelength is only a fraction of a wavelength during the interaction. In the case of nanosecond laser pulses, energy is transferred to the ions and atomic lattice, but in case of ultra-short laser pulses the energy is mainly transferred to electrons. In femtoseond solid interactions, the plasma has a very steep density gradient with a scale length of less than laser wavelength which is different from nanosecond laser produced plasma, because of significant expansion of plasma during the much longer interaction time. A schematic of laser plasma interaction is shown in Figure 2.1.

The plasma density scalelength which is in the direction perpendicular to the surface of the solid is given by ion expansion at the ion acoustic velocity giving

$$L = c_s \tau \tag{2.5}$$

Where c_s is the ion sound speed $\left(c_s = \left(ZkT/M\right)^{1/2}\right)$ and τ is pulsewidth of the laser and M is the ion mass.

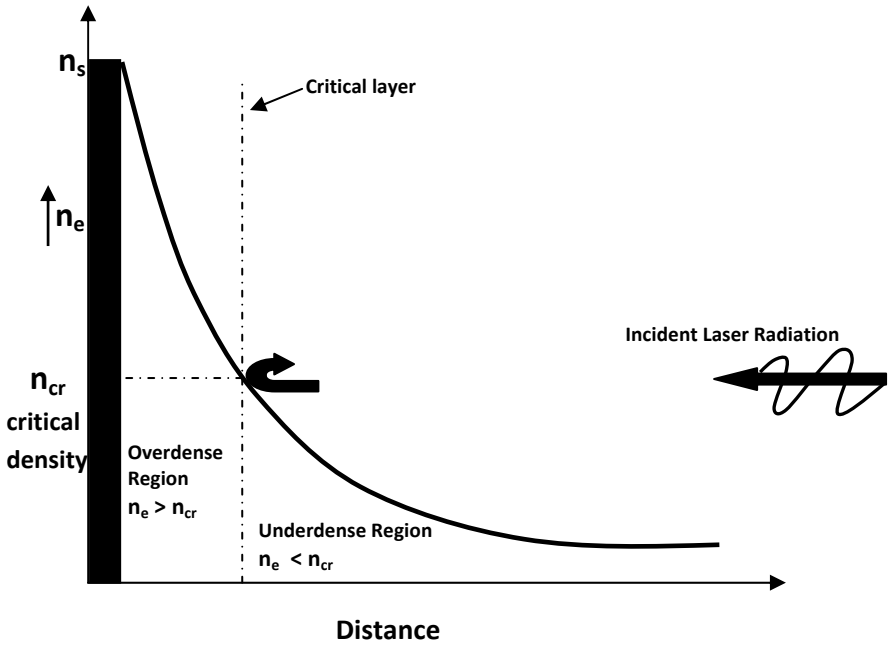

Figure 2.1 Schematic diagram of electron density profile during the laser plasma interaction on a solid surface.

Another important characteristic property, which defines different regions of the density profile for the laser plasma interaction, is the refractive index of the plasma given by

$$\eta = \left[1 - \left(\omega_p / \omega_L\right)^2\right]^{1/2} = \left[1 - \left(n_e / n_{cr}\right)^2\right]^{1/2} \qquad (2.6)$$

Which is directly related to density of the local plasma through the frequency ω_p and the frequency of the incident light. The index of refraction decreases as the density of the plasma increases from vacuum to the critical density. The refractive index becomes zero at the density point known as critical density as defined earlier. So the relation (2.6) gives two conditions (1) when $n_e < n_{cr}$ the refractive index is real and less than 1, which means that up to this point laser light can

penetrate within plasma and (2) when $n_e > n_{cr}$ the refractive index becomes imaginary and no further propagation of light is possible.

The laser interaction and energy transfer to solid target involve a number of absorption processes which in turn depend on laser and plasma parameters. The Fig. 2.2 [4] provides a macroscopic picture of processes responsible for different phenomenon in intense laser solid interactions. The wavelength scaled laser irradiance $I\lambda^2$ is the most commonly used parameters for the scaling of various laser plasma interaction effects. The interaction of intense electromagnetic field with the target starts with ionization which then leads to absorption processes involving the electrons. Further interaction with ionized material creates a strongly ionized plasma with free electrons and ions in front of target.

The free electrons oscillate in the electromagnetic field of the light and transfer energy to the plasma. This oscillatory motion of electron at the frequency of laser light is called quiver motion and is defined in terms of quiver velocity

$$\upsilon_{osc} = \frac{eE_o}{m_e \omega_L} \tag{2.7}$$

The quiver energy stored by the electrons in this oscillatory motion is

$$U_P = \tfrac{1}{2}\, m\upsilon_{osc}^2 \tag{2.8}$$

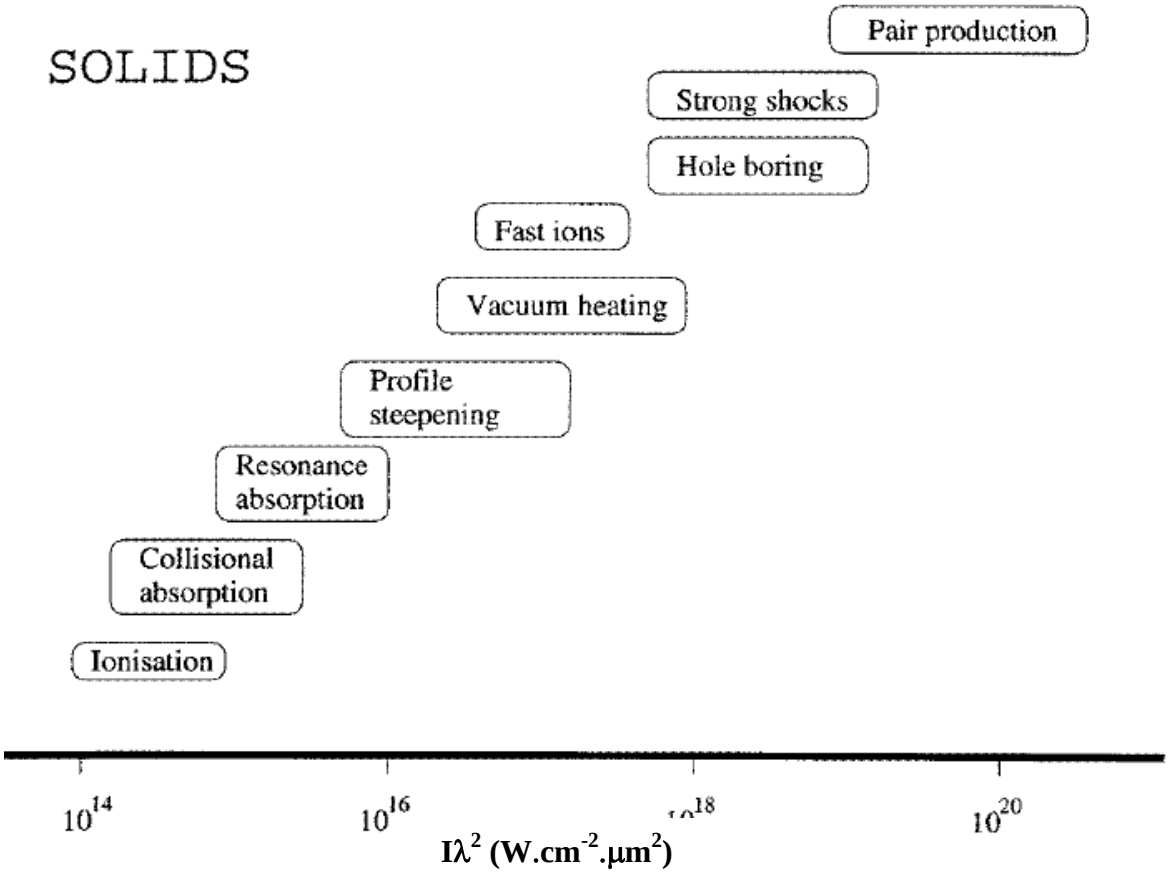

Figure 2.2 Scaling of short laser plasma interaction phenomena with solid targets as a function of incident intensity [4].

This energy when taken as the average kinetic energy over one cycle of laser is also known as the pondermotive potential and can be expressed in terms of electric field amplitude and intensity of the laser:

$$U_P = \frac{e^2 E_o^2}{4 m_e \omega_L^2} = \frac{e^2 I_o}{2 m_e \omega_L^2 c \varepsilon_o} \tag{2.9}$$

Where E_o for linearly polarized and ω_L are given by

$$E_o = \left(\frac{2I_o}{\varepsilon_o c}\right)^{0.5} = 2.75 \times 10^{11} . \sqrt{I_{16}} \quad [\text{V/m}] \tag{2.10}$$

$$\omega_L = \frac{2\pi c}{\lambda_L} = \frac{1.88 \times 10^{15}}{\lambda_L[\mu m]} \quad [\text{s}^{-1}] \tag{2.11}$$

Where I_{16} is the laser intensity in units of 10^{16} W/cm^2 and λ_L is the laser wavelength in microns. For a linearly polarized plane wave with wavelength of 0.8 μm and intensity 10^{16} W/cm^2 the pondermotive potential of an electron is $\approx 600eV$. The quiver motion of electrons was initially considered in a homogeneous plane wave, however the laser beam ideally has a gaussian transverse and temporal profiles so it has strong radial gradients with finite temporal and spatial envelopes. The electrons experience an additional acceleration due to these gradients towards lower intensities. This nonlinear acceleration is called the pondermotive force which expels the electrons from the high intensity region (centre) towards lower intensities (edges). The pondermotive force can be obtained by averaging over laser oscillations and written as

$$F_P = -\frac{e^2}{4m_e\omega^2}\cdot\nabla E^2(r) = -\nabla U_P \sim -\nabla I \qquad (2.12)$$

This force is most prominent around the highest intensity region near the focus of the guassian laser pulse. Electrons respond to this force and massive ions ($m_i >> m_e$) are also expected to feel pondermotive force but this effect is negligible due to their larger mass. Absorption due to the pondermotive force of sub-picoseconds laser pulses has been investigated in different experiments and using different models for moderate and high intensities (≥ 10^{16} W/cm^2) [31, 32].

As the laser consists of electric and magnetic fields which are perpendicular to each other, at lower intensities the force exerted on electrons is primarily due to the electric field component of the laser and the magnetic field term is lower by a

factor $\frac{\upsilon_{osc}}{c}$. As the intensity increases, the linear quiver velocity becomes of the order of velocity of light and magnetic field term also contributes to induce strong nonlinear effects on the dynamics of the electrons. The nature of interaction in this relativistic regime is determined by introducing a common dimensionless parameter a_o.

$$a_o = \frac{\upsilon_{osc}}{c} = \frac{eE_o}{\omega_L m_e c} \tag{2.13}$$

Physically this dimensionless variable can be understood as a normalized vector potential and in practical units this parameter can be written as

$$a_o = \sqrt{\frac{I_L \cdot (\lambda(\mu m))^2}{1.37 \times 10^{18} W \cdot cm^{-2}}} \tag{2.14}$$

When the irradiance $I_L \cdot \lambda_L^2$ exceeds $\approx 10^{18} W.cm^{-2}.\mu m^2$ relativistic effects start to appear and electrons motion becomes nonlinear because of normalized vector potential $a_o \sim 1$.

The invention of high intensity pulses using the CPA technique has led to impressive progress in characterizing and investigating ultrafast dense plasmas on a laboratory scale. As the laser interacts with matter, energy coupling from electromagnetic field to the solid and plasma i.e. the absorption processes becomes particularly important. It is important to understand these processes in the light of the numerous applications like the generation of hot electrons, ICF studies and ultrafast X-ray emission. In order to understand the absorption

mechanisms a number of theoretical and experimental studies have been reported for short pulse lasers with intensities in the range of 10^{12} W-cm^{-2} to 10^{16} W-cm^{-2} [33, 34, 35]. The laser absorption starts with collisional and collisionless heating processes depending on the irradiance ($I_L \cdot \lambda_L^2$) of the laser. For short pulse lasers collisional inverse bremsstrahlung and resonance absorption [36] are dominant in the intensity range of $10^{12} W \cdot \mu m^2 \cdot cm^{-2} < I\lambda^2 < 10^{17} W \cdot \mu m^2 \cdot cm^{-2}$. Above $I\lambda^2 \simeq 10^{16} W \cdot \mu m^2 \cdot cm^{-2}$ the absorption of ultrashort high intensity laser pulses are influenced by some new collisionless mechanisms which include vacuum heating, Brunel effect [37], relativistic $j \times B$ heating and the collisionless skin effects [38]. It has been reported that half of the laser energy can be transferred to electrons within the plasma at high intensities [39]. Understanding the physical phenomena involved in these absorption mechanisms is necessary for the development of practical applications. The absorption processes involved in experiments within the intensity range of 10^{15} to $10^{17} W \cdot cm^{-2}$ are of importance to this thesis and will now be described in detail.

2.2 Inverse Bremsstrahlung

Inverse bremsstrahlung is a collisional absorption process in which absorption of a photon by an electron occurs while passing through the electric field of an ion. The electrons oscillate in the electric field of the laser and this oscillation energy transfer into thermal energy via electron-ion collisions, a process known as inverse bremsstrahlung. The Coulomb interaction between the moving electron

and heavy immobile ions lead to an effective electron-ion collision frequency given by [36]

$$\nu_{ei} = \frac{4}{3}\frac{(2\pi)^{1/2} Z n_e e^4 \ln\Lambda}{(4\pi\varepsilon_o)^2 (k_B T_e)^{3/2} (m_e)^{1/2}} \sim 3\times 10^{-6}\,\frac{Z n_e \ln\Lambda}{T_e^{3/2}} [s^{-1}] \qquad (2.15)$$

Where Z is the degree of plasma ionization or ion charge, n_e is the electron density, T_e is the electron temperature and $\ln\Lambda$ is the coulomb logarithm.

In the case of laser propagation through plasma, energy damping is led by inverse bremsstrahlung absorption and is defined by absorption coefficient κ_{ib}, which can be obtained using the equation of motion of electrons including the collision term given by equation 2.15 and then solved using Maxwells equations and the dispersion relation to derive a relation for the wave vector k which is

$$k = \frac{\omega_L}{c}(1-\frac{\omega_P^2}{\omega_L^2})^{1/2}[1 + i\frac{\nu_{ei}\omega_P^2}{2\omega_L\omega_L^2}\cdot\frac{1}{1-\omega_P^2/\omega_L^2}] \qquad (2.16)$$

The absorption coefficient κ_{ib} is twice the imaginary part of k and is given by

$$\kappa_{ib} = 2\,\mathrm{Im}\,k = \frac{\nu_{ei}}{c}\frac{\omega_P^2}{\omega_L^2}(1-\frac{\omega_P^2}{\omega_L^2})^{-1/2} \qquad (2.17)$$

The density and frequency are directly related by the definition of critical density given by equation 2.4

So one can write the damping coefficient κ_{ib} in terms of density as

$$\kappa_{ib} = \frac{\nu_{ei}(n_c)}{c}\frac{n_e^2}{n_c^2}(1-\frac{n_e}{n_c})^{-1/2} \propto \frac{Z_i n_e^2}{T_e^{3/2}}(1-\frac{n_e}{n_c})^{-1/2} \qquad (2.18)$$

It is clear from the above relation that large amount of absorption due to inverse bremsstrahlung occurs close to critical density.

Suppose the laser is propagating along z direction and its intensity decreases as it passes through plasma. This change in intensity is described by

$$\frac{dI}{dz} = -\kappa_{ib} I \tag{2.19}$$

The absorption coefficient A_{ib} for a plasma of length l is given by

$$A_{ib} = \frac{I_{in} - I_{out}}{I_{in}} = 1 - \exp(-\int_0^l \kappa_{ib} dz) \tag{2.20}$$

Where I_{in} represents incoming laser intensity entering the plasma and I_{out} is the outgoing laser intensity after passing through the plasma. The laser energy absorption fraction for an exponential density profile with a scale length of l, $n_e = n_c \exp[-z/l]$, is given by [36]

$$A_{ib} = 1 - \exp[-\frac{8}{3}\frac{\nu_{ei(n_{cr})} l}{c}] \tag{2.21}$$

Inverse bremsstrahlung absorption is dominant only if there are enough collisions between electrons and ions. One can show from equation 2.15 that electron-ion collision frequency is inversely related to electron temperature so with the increase in temperature this collisional heating effect becomes less efficient.

For higher intensities ($I > 10^{15} W/cm^2$) the absorption coefficient κ_{ib} depends on laser intensity due to the change in collision frequency ν_{ie} induced by the

higher laser electric field. The electron oscillations velocities in such higher intensity interactions become comparable to the electron thermal velocity and the absorption coefficient κ_{ib} scales as $I_L^{-3/2}$ or E_L^{-3}. This means that with the increase of laser intensity inverse bremsstrahlung absorptions becomes less effective. This reduction in absorption has been reported in various experiments where a low atomic number target material such as aluminum is used for absorption measurements using laser pulses of different wavelengths and durations as shown in Figure 2.3.

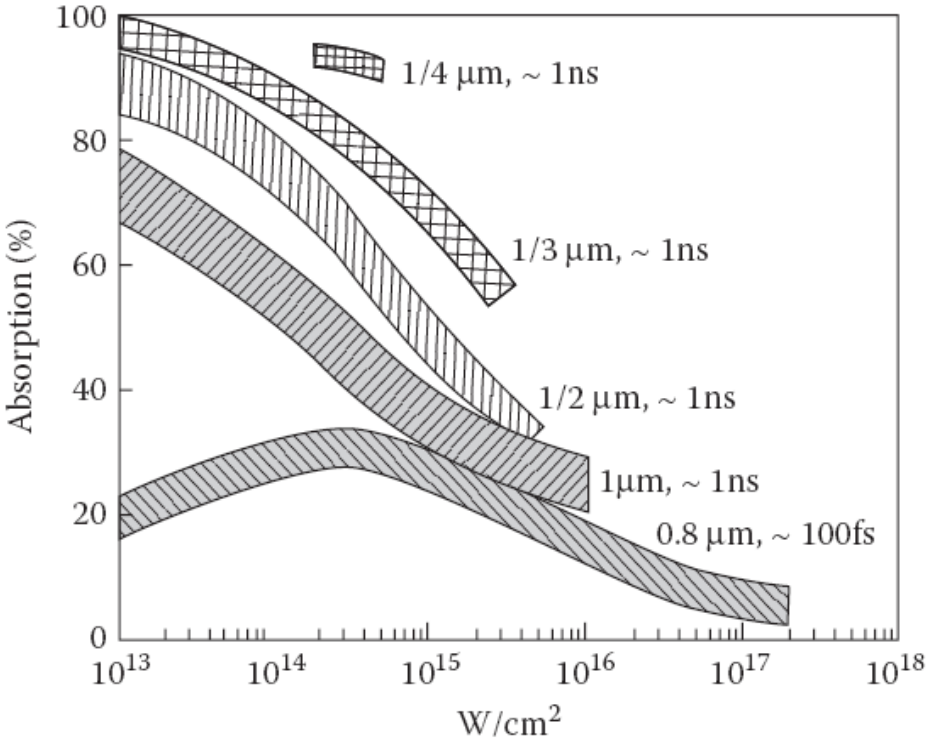

Figure 2.3 Summary of experimental absorption data for laser pulses normally incident onto low atomic number solid targets [45].

The results of Figure 2.3 provide a picture that for increasing laser intensities and shorter pulse duration collisional absorption becomes less effective and inverse bremsstrahlung absorption process is unable to account for experimental values observed for laser absorption [40, 41, 42]. However other major collisionless processes exist that can couple energy into plasma. The most important and efficient of them for intermediate intensities is resonance absorption.

2.3 Resonance absorption

Resonance absorption involves the creation of a density gradient profile of plasma from solid target by a p-polarized laser light wave obliquely incident at an angle θ. If the electric field component of the laser is parallel to the plasma density gradient ($\vec{E}_L \cdot \vec{\nabla} n_e \neq 0$) the parallel component can tunnel into the critical density surface when the laser angular frequency matches with plasma frequency and leads to the resonant excitation of the electrostatic electron plasma wave within the plasma. In this resonant process an efficient energy transfer occurs from laser field to the electron plasma wave. The damping of the electrostatic wave further leads to conversion of the laser energy into thermal energy, which heats the plasma. The whole process of conversion of laser energy into thermal energy due to the resonantly excited wave is known as resonance absorption. An overview picture of this process is illustrated in Figure 2.4.

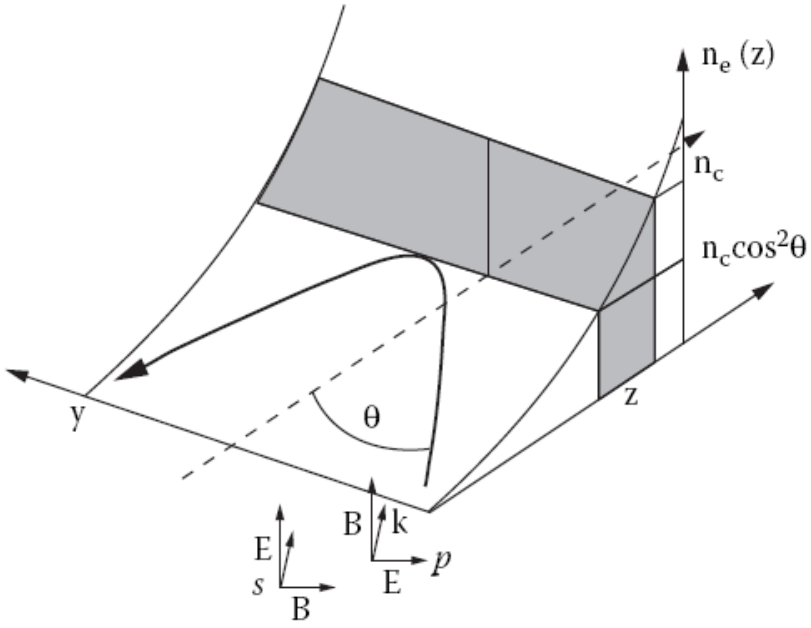

Figure 2.4 Schematic representation of resonance absorption in case of p-polarized EM-wave [43]

The damping of the waves can be due to both collision and collisionless processes (e.g Landau damping and wave breaking) depending on the intensity of the laser beam. As the electromagnetic wave is incident at an angle θ and then propagates through the plasma towards the overdense region it will be deflected by refraction in the density profile and will only propagate up to a maximum penetration density a turning point, where reflection occurs at a density given by

$$n_e = n_c \cos^2 \theta \tag{2.22}$$

The electric field component of the laser at the turning point is in the direction of density gradient and can tunnel through the plasma as an evanescent field up to the critical density point to resonantly excite the electron plasma wave. The maximum absorption depends on an optimum incident angle for the laser. For

grazing incidence the laser light only penetrates to a very low density and the evanescent wave has to propagate through a much longer distance and therefore is unable to efficiently drive a plasma wave. For normal incidence, $\theta = 0,$ there is no laser electric field component parallel to the plasma density gradient exist, and thus there is no electric field component to excite the resonant plasma wave effectively. The maximum energy coupling depends on the density scale length of the plasma and wave vector leading to an optimum incident angle for which about half of laser energy is transferred to the plasma as given by the relation

$$\theta_{opt} \cong \arcsin[(0.5kl)^{1/3}] \tag{2.23}$$

Where $k = \omega/c = 2\pi/\lambda_L$ is the wave vector and l is the density scale length.

The fractional absorption for a linear density profile is given by

$$f_{ra} \approx \frac{1}{2}\phi^2(\tau) \tag{2.24}$$

Where function ϕ and τ are defined as [38, 43, 44]

$$\varphi(\tau) \approx 2.3\tau \exp(-2\tau^3/3) \tag{2.25}$$

and

$$\tau = (kl)^{1/3} \sin\theta \tag{2.26}$$

Another relation of absorption fraction using p-polarized EM wave for a linear density profile is given by [43, 45]

$$f_{ra} \approx 36\tau^2 \frac{[Ai(\tau)]^3}{\left|dAi(\tau)/d(\tau)\right|} \tag{2.27}$$

Where Ai is the Airy function and τ is defined by 2.26. A maximum of 50% ($f_{ra} \sim 0.5$) laser energy transfer through resonance absorption is possible given by

substituting $\tau \sim 0.8,$ in equation 2.26, $\sin\theta = 0.42\,\lambda_L / l$. In the case of short pulse interaction where the plasma scale length is of the order of the wavelength $l \cong \lambda_L$ maximum fractional absorption due to resonance occurs at an angle of about 25^o as shown in the Figure 2.5 [43].

Resonance absorption is one of major processes for generation of hot electrons due to the breaking of the plasma waves and the dependence of absorption on incident angle and plasma scale length has been studied extensively [35, 46]. It is also clear from the above results that resonance absorption is a polarization dependent mechanism.

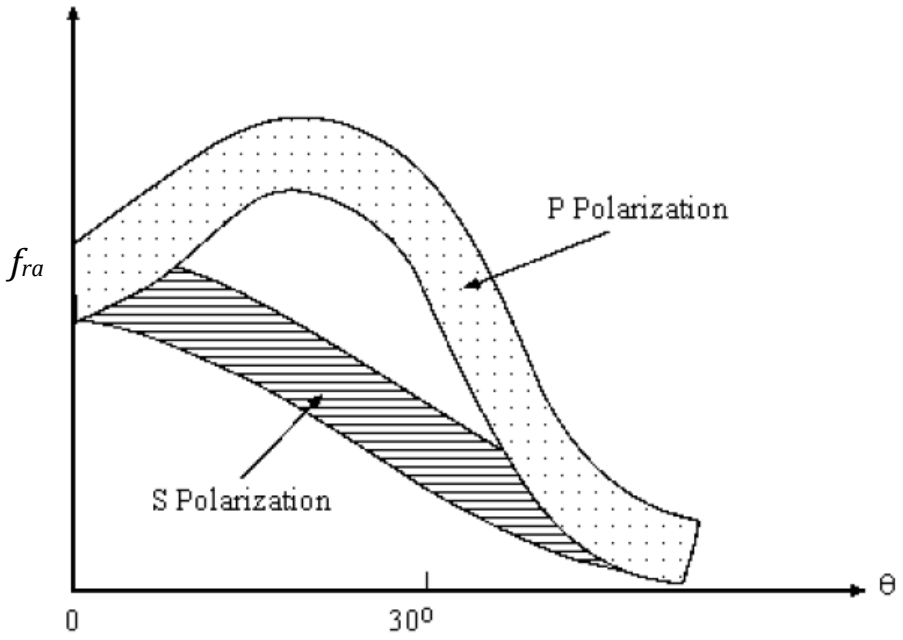

Figure 2.5 Schematic of absorption fraction for S and P-polarized laser as a function angle of incidence [43].

One can also show the polarization dependence of resonance absorption using plasma dielectric constant term $\varepsilon = 1 - n_e / n_{c,}$ Poisson equation for plasma $\vec{\nabla} \cdot (\vec{\varepsilon E}) = 0,$ and $\vec{\nabla} . \vec{E} = -4\pi e \delta n_e,$

Solving for electron density perturbation of the plasma wave δn_e one can get

$$\delta n_e = \frac{\vec{\nabla} n_e \cdot \vec{E}}{4\pi (n_e - n_c)} \tag{2.28}$$

For s-polarized laser radiation the electric field component of the laser is perpendicular to the density gradient i.e $(\vec{\nabla} n_e \cdot \vec{E} = 0)$, which means that it is unable to drive the electron plasma wave, but for the p-polarized wave, the electric field vector is parallel to density gradient $(\vec{\nabla} n_e \cdot \vec{E} \neq 0)$, so the δn_e increases sharply due to the resonant matching condition at critical density $(n_e = n_c)$.

2.4 Brunel effect

In 1987, Brunel was the first to propose an absorption process with the title not-so-resonant resonance absorption [37]. This absorption mechanism is called the Brunel effect or vacuum heating. The vacuum heating absorption is a complementary mechanism to resonance absorption in which p-polarized laser radiation is obliquely incident on a steep density gradient and then interacts with the electrons at the critical density layer to couple electromagnetic wave energy non-resonantly into an electron plasma wave. This absorption mechanism is

important in high intensity, short laser pulses in which electric field associated with laser pulses is large with a very steep density profile and such that the plasma density scale length l is smaller than the electron oscillation amplitude $d_{osc} \sim eE_L / m_e\omega^2 = \upsilon_{osc}/\omega > l$. The thermal electrons while oscillating in the first half cycle of the laser electric field can be pulled out from the surface of target towards vacuum and then stream back into the plasma with a velocity of the order of the quiver velocity υ_{osc} as the laser electric field reverses its direction. As the electric field of the laser is unable to propagate deep into the overdense region but only can penetrate over a skin depth of $\sim c/\omega_p$, the electrons move deeper into the solid target and deposit their energy through collisions. So in this effect is responsible for hot electron generation during each laser cycle. The electron acceleration while streaming back into matter is normal to the surface of the target as the electric field of the laser has to be perpendicular to the surface. The schematic representation of Brunel effect is depicted in Figure 2.6.

A simple analysis can be carried out based on a model in which p-polarized laser radiation with electric field $E = E_L \sin\omega t$ is obliquely incident on a smooth, flat, mirror like surface of solid. For the low intensity regime where absorption due to magnetic component of wave can be ignored, the eclectic field component perpendicular to the target surface will act as a driving field for the electrons on the surface. The amplitude of this driving electric field is $E_d = 2E_L \sin\theta$, where θ

is the angle of incidence. The vacuum heating effect is found to be more efficient for higher driving field strength and larger angle of incidence.

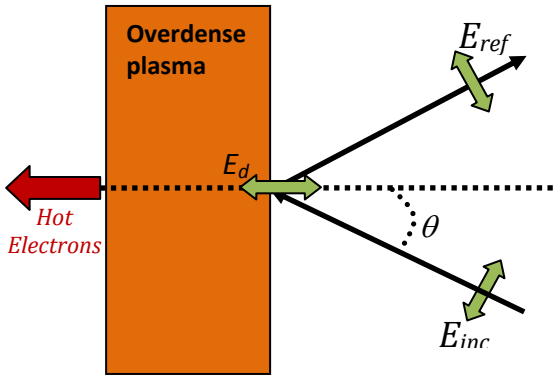

Figure 2.6 Schematic of fast electron acceleration in vacuum heating as an absorption mechanism.

The fraction of laser energy absorbed is given by [37].

$$f_{vh} = \frac{\eta}{2\pi} \frac{\upsilon_d^3}{\upsilon_{osc}^2 c \cos\theta} \tag{2.29}$$

Where υ_d is quiver velocity due to deriver field E_d normal to the target surface and η is an efficiency factor which provides an estimate of conversion of oscillatory motion into thermal energy within plasma. Brunel derived $\eta \approx 1.75$ and later it is found [47] that absorption has a dependence on plasma density given by the relation $\eta \approx (1 - \frac{\omega_L^2}{\omega_P^2})^{-1}$. This simple absorption model has been further extended theoretically, numerically and experimentally [41, 48, 49, 50, 51] for different density scale lengths and laser intensities. Gibbon and Bell [48]

performed analysis of Brunel mechanism using $1\frac{1}{2}$D PIC simulations for plasma with density scale lengths of $l/\lambda = 0.01$ to 2 and laser irradiance $I\lambda^2$ varying from $10^{14} W \cdot \mu m^2 \cdot cm^{-2}$ to $10^{18} W \cdot \mu m^2 \cdot cm^{-2}$. They observed the dependence of absorption as a function of the plasma density profile laser intensity and incident angle demonstrating maximum absorption for an angle of incidence of about 45^o. For irradiance $I\lambda^2 \sim 10^{16} W.\mu m^2 \cdot cm^{-2}$ and using the optimum angle, approximately 70% absorption is observed for $l/\lambda = 0.1$ and this deceases down to 10% for a steep density profile of $l/\lambda = 0.01$. There are other collisionless absorption mechanisms found to be important responsible in the context of ultrashort, high intensity laser solid interactions such as the relativistic $J \times B$ heating and collisionless skin effects. These mechanisms are not part of this thesis, but a detailed review article of these effects is given in references [38, 52].

2.5 Hot Electron Generation

"Hot electron" is a term associated with electrons having a kinetic energy much greater than the thermal Maxwellian distribution. The evidence of these suprathermal electrons can be observed as long tails with much higher temperature T_h superimposed on a simple thermal Maxwellian population which is characterized by a temperature T_e. These hot electrons are generally generated from wave particle interaction typically involving electron plasma waves from

resonance absorption, Raman scattering, two plasma decay and other absorption mechanisms as discussed earlier. The collisionless Landau damping is more effective in the case of hot inhomogeneous plasma than normal collisional damping effects. All these mechanisms are collectively responsible for production of hot electrons and depend on laser intensity, pulse duration, plasma density scale lengths and angle of incidence, so it is difficult to isolate these effects in simulations and experimental measurements. The measurement of X-ray emission from laser matter interactions provides evidence of hot electron generation with quasi-Maxwellian distribution functions. Collisional damping is an effect in which amplitude of the oscillating electron wave is reduced as a result of collisions of oscillating electrons with their neighboring ions. In this process electron-ion collision transform coherent electron oscillations into random motion. The rate at which electron dissipates its kinetic energy is given by [36]

$$\frac{\nu E^2}{8\pi} = \nu_{ei} \frac{nm\upsilon_{osc}}{2} \tag{2.30}$$

Where υ_{osc} is quiver velocity as mentioned above, E is the amplitude of plasma wave, n is the density of plasma, ν_{ei} is the electron-ion frequency and $\nu = \omega_P^2 \nu_{ei} / \omega^2$, where ω_P and ω are the plasma and laser frequency respectively.

Besides collisional damping mechanism, there is another damping effect known as collisionless or Landau damping which involves the exchange of energy from an electron wave to its surrounding particles. This transformation of energy

is based on a resonance effect by which those electrons are accelerated whose velocity matches with the phase velocity of electron wave. Under these conditions, the electrons experience a constant electric field so that they can be accelerated or decelerated in order to exchange energy with the electron wave. The rate at which the electrons gain or lose energy is expressed mathematically as [36]

$$\frac{dE}{dt} = -\frac{\pi q^2 E^2}{2m|k|}\frac{\omega}{k}\frac{\partial f}{\partial \upsilon}\left(\frac{\omega}{k}\right) \tag{2.31}$$

Where f is the electron velocity distribution function, ω is the angular frequency and k is the wave number. The rate of exchange of energy depends on the slope of electron velocity distribution at the phase velocity of the electrostatic wave which determines the resonant electrons. The particles with velocity slightly less than ω/k gain energy while those with slightly higher velocity than ω/k lose energy. A strong collisionless damping of electron waves is observed at a phase velocity given by [53]

$$\frac{\omega}{k} \le 3\upsilon_{th} \tag{2.32}$$

Where υ_{th} is the thermal velocity given by $\upsilon_{th} = \sqrt{KT_e/m_e}$.

Wave breaking [36, 54] of electron plasma waves is another mechanism to accelerate particles in a nonlinear interaction manner. In this nonlinear regime higher amplitude electron waves have large field which can trap particles of

different velocities into resonance, which is quite different from the linear treatment where a small amplitude wave is damped by particles with velocities close to the phase velocity of the electron wave. The strong effect of wavebreaking can trap non-resonant electrons into the plasma wave and the energy of this wave is damped suddenly due to acceleration of many low velocity electrons. These electrons in the breaking plasma wave gain kinetic energy efficiently from the plasma wave into a velocity spectrum around the phase velocity of the original wave. The theoretical and experimental evidence of wavebreaking phenomena under different conditions have been reported in the literature [54, 55] and is an important ingredient in recent laser wakefield acceleration experiments [56, 57, 58, 59]. The plasma waves can also be driven by wave-wave interactions such as the Raman, 2-plasmon or Brillouin instabilities which can in turn accelerate electrons.

The hot electrons generated by short laser pulses can then be used to generate a controlled source if radiation. The most important radiation lies in the XUV to hard X-ray range. Before going into the detail of radiation emission in the hard X-ray range from hot electrons, the emission processes in plasmas will be briefly reviewed.

2.6 X-ray Emission processes

The X-ray emission processes in plasmas are divided into line radiation (bound-bound transition), recombination (free-bound transition) and bremsstrahlung (free-free transition) [60].

2.6.1 Line radiation (bound-bound transition)

Line radiation is emitted as a result of an inner shell transition of electrons between two discrete energy levels of an atom or ion. In this process energy is provided to a bound electron via absorption of radiation or a collision to excite it to a higher energy state. In order to fill the vacancy and re-establish equilibrium an electron from a higher energetic level of this atom (ion) will fill the vacant position. In this way the extra energy of the electron can be released in the form of a photon. The energy of the photon is exactly equal to the energy difference between the two bound levels between which the transition occurs. These photons are known as line (characteristic) radiations due to their discrete emission wavelength and well defined character.

Consider line emission when an electron makes a transition from upper level (u) to lower level (l), then the emissivity between two discrete levels is given by

$$J_\nu = n_u A_{ul} \frac{h\nu_{ul}}{4\pi} \varphi(\nu) \tag{2.33}$$

Where n_u, A_{ul}, ν_{ul} and $\varphi(\nu)$ represents population density of upper state u (cm^{-3}), spontaneous radiative rate (Hz), radiation frequency for the transition u to l and the normalized line profile function respectively.

The absorption coefficient of this transition is given by

$$\kappa_\nu = \frac{\pi e^2 n_l}{m_o c}(1-\frac{n_u}{n_l}\frac{g_l}{g_u}) f_{lu}\varphi(\nu)\ [cm^{-1}] \tag{2.34}$$

Where g_u and g_l are statistical weights of the upper and lower levels respectively and f_{lu} is the absorption oscillator strength of the transition from lower state l to upper state u. The spontaneous decay rate A_{ul} and absorption oscillator strength f_{lu} can be related using Einstein coefficients for atomic spectral line emission given by

$$A_{ul} = \frac{8\nu^2\pi^2 e^2}{m_e c^3}\frac{g_l}{g_u} f_{lu} \tag{2.35}$$

2.6.2 Recombination (free-bound transition)

In the process of recombination a free electron is trapped by an ion of charge state Z while passing close to it and forms an ion of charge state Z-1 or a neutral atom in an excited state. The excess energy results in emission of a photon whose energy is the sum of the kinetic energy of the free electron and the ionization potential of the bound level. The emissivity for such emission from an ion state $i+1$ recombining to a state i is given by [60]

$$J_\nu = 1.01\times10^{-42} n_{i+1} n_e \frac{g_i}{g_{i+1}} g_{fb} \frac{I_P^{2.5}}{T_e^{1.5} Z}\exp(-\frac{h\nu - h\nu_{I_P}}{kT_e}) \quad [erg/cm^3/s/Hz/sr] \quad \text{for } \nu \geq \nu_{I_P} \tag{2.36}$$

$$J_\nu = 0\ [erg/cm^3/s/Hz/sr] \text{ for } \nu \leq \nu_{I_P}, \tag{2.37}$$

Where I_P is the ionization potential in electron volts and ν_{I_P} is the frequency corresponding to the ionization potential of state i, n_e and n_{i+1} are the number densities of the electrons and upper state ions in units of cm^{-3}, g_i and g_{i+1} are the statistical weights of the ionization states i and $i+1$ respectively. g_{fb} is factor for free-bound transition known as the Gaunt factor.

The corresponding absorption coefficient of this transition is [60]

$$\kappa_\nu = 4.13\times10^{26}\frac{n_i I_P^{2.5}}{Z\nu^3} g_{bf} \times[1-1.66\times10^{-22}\frac{n_{i+1}}{n_i}\frac{g_i}{g_{i+1}}\frac{n_e}{T_e^{1.5}}\exp(-\frac{h\nu - h\nu_{I_P}}{kT_e})]\ [cm^{-1}] \quad \text{for}$$

$$\nu \geq \nu_{I_P} \tag{2.38}$$

Where I_p and T_e are in units of eV and densities are in units of cm^{-3}.

$$\kappa_\nu = 0\ [cm^{-1}] \text{ for } \nu \leq \nu_{I_P}, \tag{2.39}$$

2.6.3 Bremsstrahlung (Free-Free transition)

The process of bremsstrahlung is the radiative interaction of electrons with the coulomb potential of the ions. The electron passing in the vicinity of ion changes its direction due to coulomb forces of attraction and energy is emitted in space as electromagnetic radiation from the acceleration of electron. This process is also known as 'braking radiation' due to deceleration of the electron during the interaction. The bremsstrahlung is also called continuum radiation because it is detected as a continuous background spectrum overlapping the characteristic lines. The emissivity for free-free transition assuming electrons having a Maxwellian distribution with temperature T_e is given by [60]

$$J_\nu = \frac{32\pi}{3}\sqrt{\frac{2\pi}{3kT_e}}\frac{n_e e^6}{m_e c^3}\sum_i n_i Z_i^2 \exp(\frac{h\nu}{kT_e}) \quad (2.40)$$

$$= 5.05\times10^{-41}\frac{n_e}{T_e^{1/2}}\sum_i n_i Z_i^2 \exp(\frac{h\nu}{kT_e})[erg/cm^3/s/Hz/sr] \quad (2.41)$$

Where T_e, n_e and n_i are the electron temperature (eV), electron density and ion density (cm^{-3}) respectively.

Continuum emission measurements from the laser plasma interaction provides a strong signature of hot electron generation. Depending on the laser and plasma parameters bremsstrahlung radiation from these suprathermal electrons range from a few keV to MeV and of the order of duration nearly equal to the laser pulse. Hot electrons have received considerable study because of their importance in laser driven inertial confinement fusion [61]. In initial stages of fusion experiments these electrons were found to preheat the fusion pellet which in fact prevents its effective inertial compression. In general, these electrons are an excellent source of hard X-rays which have applications in time resolved studies [5] and high resolution imaging [18, 19].

The spectral density of bremsstrahlung X-rays for a Maxwellian distribution of electrons having temperature T_h is given by

$$W(E) \propto \frac{1}{T_h^{1/2}}\exp(-\frac{E}{kT_h}) \quad (2.42)$$

The hot electron temperature can be deduced by taking the slope of the exponential tail in semi-log coordinates of the experimental bremsstrahlung spectrum in the region $E >> KT_h$. However it has been reported in theory [36], simulation [49] and experiments [62] that the hot electron bremsstrahlung spectrum itself is far from thermodynamic equilibrium and electrons often have a distribution function which is bi-maxwellian due to multiple sources. This means that the electrons have multiple temperatures one due to the thermal electron distribution and others due to the hot electron distribution.

The hot electron temperature scales with laser intensity for each interaction process according to well-established scaling laws [52] described in theory, simulations and experiments. Now we will review some theoretical scaling laws and compare these with different experimental results.

In 1977, David Forslund [63] used two dimensional Particle-in-Cell (PIC) modeling to simulate the interaction of intense lasers with inhomogeneous plasma and studied resonance absorption for the non-relativistic regime as a source of hot electrons with quasi-maxwellian distribution. According to the results obtained the hot electron temperature scales as [63]

$$T_h^F(keV) = 14(I_{16}\lambda_{\mu m}^2)^{1/3} T_c^{1/3}[keV] \qquad (2.43)$$

Where T_h is hot electron temperature in keV, I_{16} is the laser intensity in units of $10^{16} W/cm^2$, λ is the wavelength of laser in micrometers and T_c is the background electron temperature in keV.

Brunel [37] provided a different absorption mechanism as stated earlier in which electrons are accelerated directly by the interaction of the laser with a step like density profile. According to this model [37] hot electron temperature is proportional to square of quiver velocity.

$$T_h^B = \frac{m\upsilon_{osc}^2}{2} \cong 3.71(I_{16}\lambda_{\mu m}^2)[keV] \tag{2.44}$$

Where I_{16} and $\lambda_{\mu m}$ are laser intensity ($10^{16} W/cm^2$) and wavelength in microns respectively. This model does not include relativistic effects which lead to a reduction in scaling at higher intensities.

Gibbon and Bell [48] used PIC simulations to determine vacuum heating as the dominant absorption mechanism for obliquely incident laser pulses on a steep but finite density gradient $L/\lambda \leq 0.1$. This simulation assuming fixed ions provided hot electron temperature scaling given by [48]

$$T_h^{GB} \cong 7(I_{16}\lambda^2)^{1/3}[keV] \tag{2.45}$$

The scaling laws introduced dealt with non-relativistic motion of electrons, but in the last few year's lasers with power up to the petawatt level and irradiance

above $10^{21} W \cdot \mu m^2 / cm^2$ have been developed. The electron motion becomes relativistic at intensity greater than $10^{18} W / cm^2$. So taking relativistic effects into account Wilks [31] predicted a scaling law, which provides electron energy accelerated by pondermotive potential as $T_h^W \propto e\phi_p$, Where ϕ_p is the pondermotive potential.

$$T_h^W \approx 511((1+\frac{I\lambda_{\mu m}^2}{1.37\times 10^{18}})^{1/2}-1)[keV] \tag{2.46}$$

The scaling law obtained from experiments using laser pulses focused on plane targets results in a hot electron temperature given by Beg et al. [64]

$$T_h^{Beg}(keV) = 215(I_{18}\lambda_{\mu m}^2)^{1/3} \tag{2.47}$$

Results of reported hot electron temperature measurements are summarized in Table 2.1 and Figure 2.7.

Table 2.1 Experimental reported hot electron temperatures T_{hot} with different laser and target parameters

Reference	$I(W/cm^2)$	$T_h(keV)$	**Prepulse Contrast Ratio**	θ_{inc}	**Target**	$t_L(fs)$	$\lambda(nm)$
Chen [65]	1×10^{18}	60 110	10^{-4} ps	45p	Cu	60	400
Rettig [66]	4×10^{18}	~5		45p	Mo	45	800
Hou [67]	2.2×10^{18}	18.5 17 20 34 48	10^{-6} ns	45p	Cu Ge Mo Ag Sn	22	800
Hou [68]	2.2×10^{18}	19		45p	Mo	22	800
Rajeev [69]	2×10^{15}	6	10^{-5} ps	45p	Cu	100	806
Zhavoronkov [70]	$\sim10^{17}$	19	10^{-5}	20p	Cu	45	800
Li [71]	2×10^{18}	305	$\sim10^{-5}$	70p	Al	30	800
Chen [26]	2.2×10^{18}	25	10^{-4}ps 10^{-5}ns	56p	Ag	70	800
Chen [26]	4×10^{18}	40	10^{-4}ps 10^{-5}ns	56p	Ag	70	800
Kutzner [22]	2×10^{15}	4.31	10^{-3}	45	Fe	25	800
Hagedorn [21]	2×10^{14} 2×10^{14} 2×10^{14} 2×10^{14}	1.50 2.62 2.79 2.34	10^{-3}	45	Ti Ni Cu Zn	35	800

Reference	$I(W/cm^2)$	$T_h(keV)$	**Prepulse Contrast Ratio**	θ_{inc}	**Target**	$t_L(fs)$	$\lambda(nm)$
Zamponi [72]	10^{18}	19		20	Cu	35	800
Liao [73]	2.8×10^{15}	3.6	$2.5\text{x}10^{-5}$	45p	Ni	300	1064
Fourmaux [74]	8×10^{17}	13	10^{-5}	~p	Mo	35	400
Toth [19]	3×10^{18}	16	10^{-5}	N.G	Ag	70	400
Chen [75]	3×10^{15}	3	10^{-5}	60p	Al/Si	1300	1050
Rousse [25]	2×10^{16}	8.5	Optimum	7p	Al/Si	100	620
Bastiani [76]	4×10^{16}	19	10^{-5}	45p	Si	120	800
Eder [77]	$\sim10^{17}$	40	10^{-4}	45p	Cu	200	790
Schnuerer [78]	5×10^{17}	66	10^{-6}	45p	Ta	700	1056
Yu [79]	5×10^{17}	25	Higher	45p	Ag	400	530
Teubner [80]	1×10^{18}	8	10^{-7}	45p	Al/Si	400	248
Pretzler [81]	2×10^{18}	200		45p	Cu/Si	130	800
Kmetec [82]	3×10^{18}	300	10^{-6}	30p	Ta	120	807
Schnuerer [83]	3×10^{18}	250	10^{-5}	45p	Ta	80	800
Serbanescu [24]	4×10^{16}	7.7	5×10^{-4}	30p	Cu	120	800

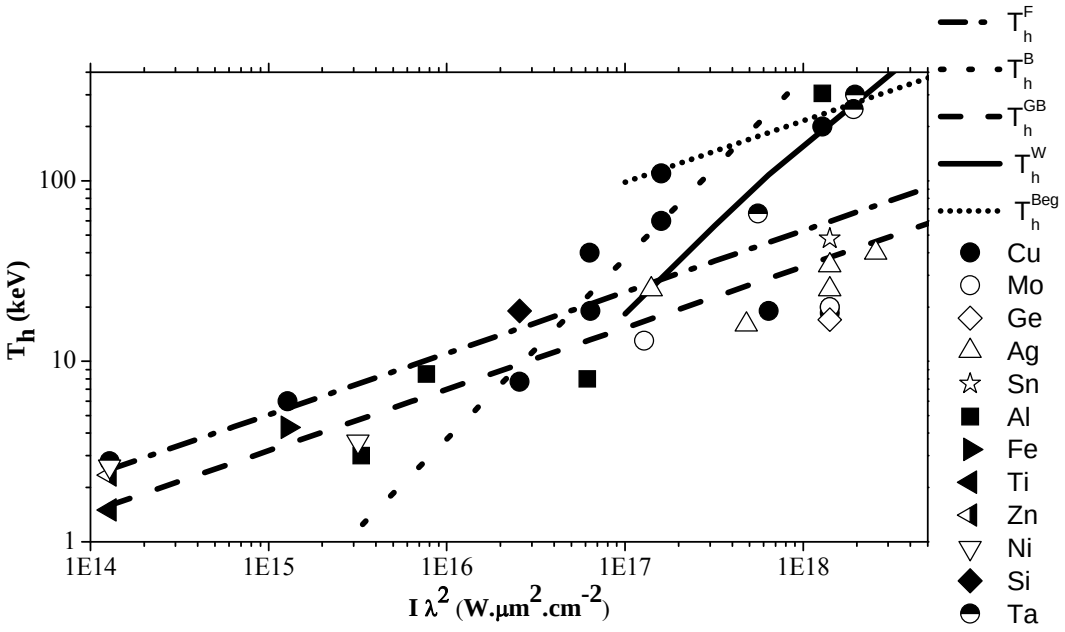

Figure 2.7 Measurements of the hot electron temperature T_{hot} from laser produced plasma using short laser pulses for different metal targets. Four theoretical models for Thot are superimposed on the experimental results: Forslund (equation 2.43 assuming Tc = 0.5 keV), Brunel (equation 2.44), Gibbon & Bell (equation 2.45), Wilks (equation 2.46) and Beg (equation 2.47) (Following Gibbon [52]) .

A review of experimentally observed hot electron temperature using different measurement methods is plotted along with five scaling laws in Figure 2.7. The experimental results are given in Table 2.1 along with their references. It is clear from the plot that hot electron temperature makes a transition from resonance absorption to vacuum heating scaling for irradiance between $I\lambda_{\mu m}^2 > 10^{16} W \cdot cm^{-2} \cdot \mu m^2$ to $I\lambda_{\mu m}^2 > 10^{17} W \cdot cm^{-2} \cdot \mu m^2$ and then another transition to hot electron scaling of Wilks at high irradiances $I\lambda_{\mu m}^2 > 10^{18} W \cdot cm^{-2} \cdot \mu m^2$ due to relativistic effects. All these measurements show general agreement with scaling at different intensities, but the contrast ratio (ratio of prepulse to main

pulse) is also an important factor which can enhance the generation of hot electron generation and K_α X-ray emission along with incident angle, pulse duration and polarization.

2.7 K_α Emission from femtosecond laser produced plasmas

The collective processes such as resonance absorption start to dominate with the interaction of laser irradiance ($I\lambda^2$) above $10^{15} W \cdot \mu m^2 / cm^2$ with matter. These absorption processes are the source of energetic or hot electrons having energies from tens to hundreds of electron volts dependent on the laser intensity. The hot electrons generated in this process have the ability to penetrate deeply into the target to knock out electrons from inner shells of the atoms thus resulting in a vacant positions. The radiative de-excitation of electrons from outer shells can result then in characteristic X-ray line radiation. The main advantage of X-ray flashes from short pulse laser plasmas over other sources is the ultrashort pulse duration and very small source size. These multi-keV X-ray pulses have potential application in the field of ultrafast X-ray diffraction, high resolution X-ray imaging such as phase contrast imaging of thin tissues and imaging for high energy density physics. In order to make these sources practical a lot of research effort has been devoted in the past two decades and still is in progress to improve and optimize characteristic emission from such ultra-intense, short laser pulses [5, 17, 18, 19 , 21, 24]. The studies of hard X-ray emission from laser plasmas initially started with low repetition rate laser pulses with energies from millijoules to joules per pulse. Using these laser systems scientists were able to report

significant X-ray flux per pulse which increased with laser intensity. The high intensity lasers available with peak powers from terawatts to petawatts may not be necessarily required to achieve the highest K_α photon flux [84]. The higher laser intensities will give rise to high temperatures for hot electrons produced which spread laterally and penetrate more deeply into the target resulting in an increase of pulse duration and source size. With the generation of K_α photons by hot electrons penetrating deeply into the target, a large number of the X-ray photons will be reabsorbed on their way to the surface of target. In addition the higher energies and the self generated electric and magnetic fields tend to modify the orbit of the hot electrons to spread them over a larger area of the target surface.

Analytical models [84, 85, 86] have been presented to clarify the processes involved in producing ultrashort (sub-ps) K_α X-ray emission using laser interaction with solid targets. Using these models hot electron penetration into the solid and the K_α yield associated with this process can be studied in detail. Riech et al. [84] showed from simulations that the optimum K_α yield can be obtained from low Z targets using moderate laser intensities of about $<10^{17}\,W/cm^2$, but higher intensities from 10^{18} to $10^{19}\,W/cm^2$ were required for high Z materials to provide maximum K_α efficiency as shown in Figure 2.8.

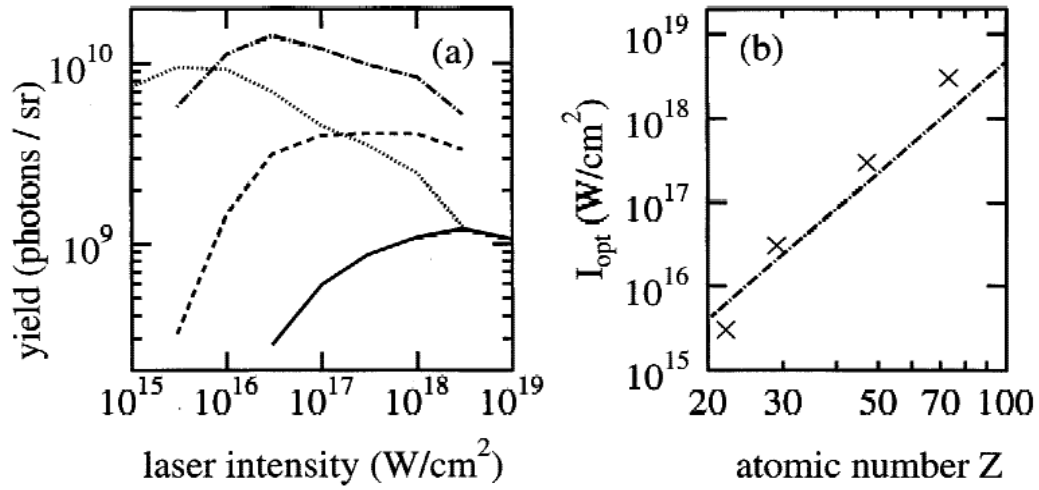

Figure 2.8 (a) simulated results of K_α yield as a function of laser intensity for Ti (Z=22 (dotted line)), Cu (Z=29 (dash-dot line)), Ag (Z=47 (dashed line), and Ta (Z=73 (solid line) assuming laser energy 100mJ. (b) Simulated (cross points) from (a) along with analytical model results (line), show the dependence of optimum intensity for different metal targets. From Reich et al. [84].

Quantitative analysis of hot electrons temperature and K_α flux as a function of foil thickness and atomic number was carried out by Salzmann et al. [85]. Using an analytical model they plotted K_α efficiency as a function of various target atomic number (Z) and typically an order of magnitude higher conversion efficiency in their model predictions compared to experimental measurement predicted. The Figure 2.9 shows a comparison of predicted scalings versus reported experimental measurements.

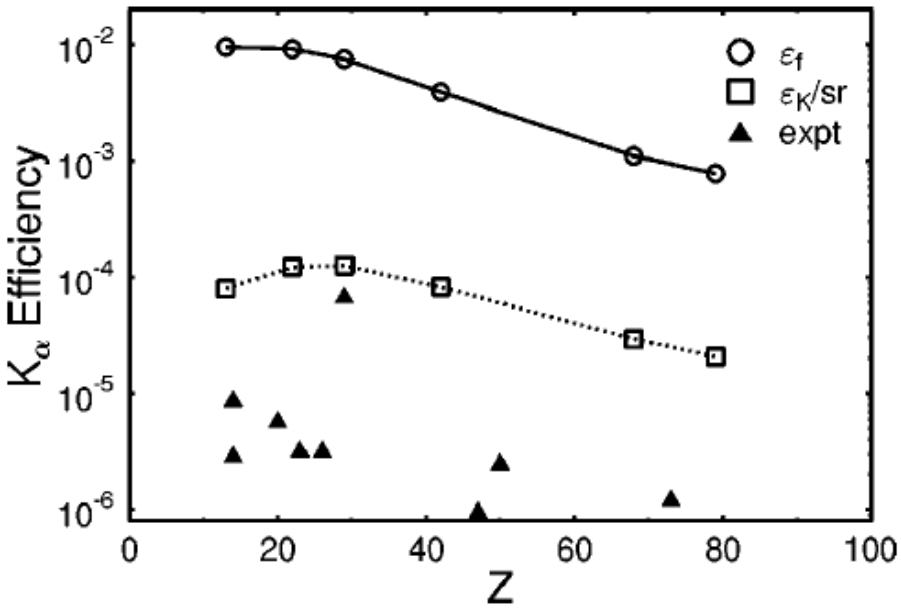

Figure 2.9 K_α efficiencies for different Z materials under optimum conditions. Open circles represent photons per electron, open squares represent conversion efficiency of K_α photons emitted per unit solid angle, and closed triangles experimental measurements. From Salzmann et al. [85].

Different groups are working around the world in order to achieve high K_α conversion efficiency using femtosecond lasers and in order to develop these sources in practical forms for different application. The current focus is on using small table-top kilohertz laser systems with low energy to obtain the required X-ray flux. These laser systems are easy to operate with low maintenance cost, but X-ray fluxes reported using these compact lasers is low as compared to larger, high energy laser systems. Figure 2.10 and Table 2.2 provides a brief summary of reported K_α conversion efficiencies obtained by various groups using femtosecond laser plasma X-ray sources.

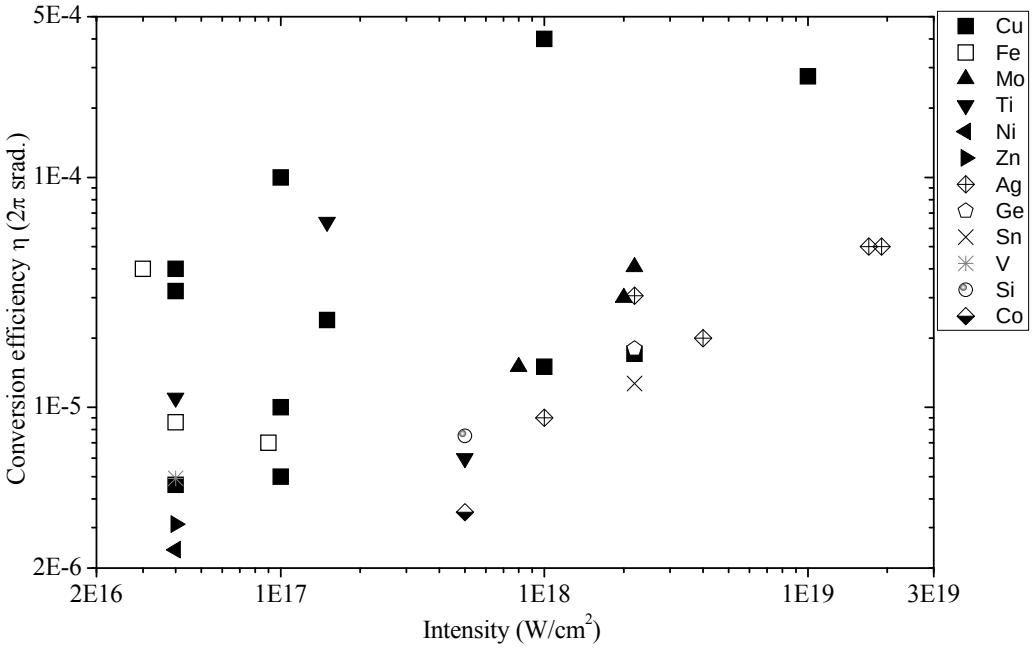

Figure 2.10 Experimental reported K_α conversion efficiency results given in table 2.2 are plotted as a function of laser intensity.

Table 2.2 Experimental reported K_α efficiencies into 2π steradian with different laser and target parameters

Reference	**Atomic number (Z)**	k_α **X-ray Energy [keV]**	**I (W/cm^2)**	**Energy per pulse [mJ]**	**Laser rep. rate [Hz]**	**Conversion efficiency** $\eta_{k_\alpha}(2\pi)$
Chen [65]	Cu (29)	8.05	1×10^{18}	100	10	4×10^{-4}
Silies [87]	Cu (29) Fe (26)	8.05 6.40	1×10^{17} 9×10^{16}	~3.5 ~3	1000	5×10^{-6} 7×10^{-6}
Kutzner [88] (tapes)	Cr (24) Fe (26)	5.41 6.40	4×10^{15}	0.40	1000	4.35×10^{-7} 2.56×10^{-6}
Kutzner [22]	Fe (26)	6.40	2.8×10^{15}	0.45	1000	3.15×10^{-6}
Fourmaux [74]	Mo (42)	17.48	8×10^{17}	90	100	1.5×10^{-5}
Hagedorn [21]	Ti (22) Cr (24) Fe (26) Ni (28) Cu (29) Cu (29) Zn (30)	4.51 5.41 6.40 7.48 8.05 8.05 8.64	2×10^{14} 2×10^{14} 2×10^{14} 2×10^{14} 2×10^{14} 4×10^{15} 2×10^{14}	0.1 0.1 0.1 0.1 0.1 0.9 0.1	1000	2.85×10^{-9} 2.1×10^{-9} 1.05×10^{-9} 1.95×10^{-9} 2.6×10^{-9} 1.5×10^{-8} 5.0×10^{-10}

Reference	**Atomic number (Z)**	k_α **X-ray Energy [keV]**	**I (W/cm^2)**	**Energy per pulse [mJ]**	**Laser rep. rate [Hz]**	**Conversion efficiency** $\eta_{k_\alpha}(2\pi)$
	Mo (42)	17.48	3.6×10^{15}	0.9		3.0×10^{-10}
Chen [26]	Ag(47)	22.2	4×10^{18}	460/260	10	2.0×10^{-5}
Lu [89]	Cu (29) Ti(22)	8.05 4.51	1.5×10^{17} 1.5×10^{17}	100	10	2.4×10^{-5} 6.4×10^{-5}
Zhavoronkov [70]	Cu (29)	8.05	$\sim 10^{17}$	5	1000	1.0×10^{-5}
Rousse [25]	Fe (22)	6.4	3×10^{16}	1.5	10	4×10^{-5}
HOU [67]	Cu (29) Ge (32) Mo (42) Ag (47) Sn (50)	8.05 9.9 17.48 22.2 25.3	2.2×10^{18}	0.8	400	1.71×10^{-5} 1.80×10^{-5} 4.08×10^{-5} 3.06×10^{-5} 1.27×10^{-5}
Rettig [66]	Ti (22) V (23) Fe (26) Ni (28) Cu (29) Zn (30)	4.51 4.95 6.40 7.48 8.05 8.63	4×10^{16}	1.8	1000	1.1×10^{-5} 4.9×10^{-6} 8.6×10^{-6} 2.4×10^{-6} 4.6×10^{-6} 3.1×10^{-6}

Reference	**Atomic number (Z)**	k_α **X-ray Energy [keV]**	**I (W/cm^2)**	**Energy per pulse [mJ]**	**Laser rep. rate [Hz]**	**Conversion efficiency** $\eta_{k_\alpha}(2\pi)$
HOU [68]	Mo (42)	17.48	2×10^{18}	1.07	400	3×10^{-5}
Zamponi [72]	Cu (29)	8.05	10^{18}	5	1000	1.5×10^{-5}
Liao [73]	Ni (28)	7.48	2.8×10^{15}	.05	1000	5×10^{-8}
Toth [19]	Ag (47)	22.2	$\sim10^{18}$	240	10	9×10^{-6}
Serbanescu [24]	Cu (29)	8.05	4×10^{16}	.290	1000	3.2×10^{-5}
Chakera [17]	Cu (29)	8.05	4×10^{16}	.260	1000	4×10^{-5}
Eder [77]	Cu (29)	8.05	$\sim10^{17}$	200	10	1×10^{-4}
Park [90]	Ag (47)	22.2	1.7×10^{19}	161×10^{3} (10 ps)		5.0×10^{-5}
Park [27]	Ag (47)	22.2	1.9×10^{19}	192×10^{3} (70 ps)		5.0×10^{-5}
Ziener [91]	Si (14) Ti (22) Co (27)	1.74 4.51 6.93	5×10^{17}	240	10	7.5×10^{-6} 6.0×10^{-6} 3.5×10^{-6}
Khattak [92]	Cu (29)	8.05	$\sim10^{19}$	~300		2.75×10^{-4}

2.8 Phase Contrast Imaging

X-ray imaging based on absorption contrast is currently a standard for clinical applications, which is due to small differences in absorption of X-rays passing through the tissue sample. This conventional imaging technique is unable to provide high resolution with high contrast images particularly for soft tissues. In the last decade significant improvements have been made by employing phase properties of X-rays to enhance the image contrast particularly in low Z materials. The detection of low contrast details in weakly absorbing samples makes the phase contrast technique a powerful tool in imaging applications.

Three different approaches can be used in phase contrast imaging which are interferometric imaging, diffraction enhanced imaging (DEI) and propagation or in-line imaging. The propagation based imaging is a simple technique as compared to the other two, because no complex alignment of sophisticated optics are used in the experimental setup. The simplicity of this technique can make it more practical to use for radiological applications. Micro-focus X-ray tubes, plasma focus devices, synchrotron sources and laser plasma X-ray sources can be used for in-line based imaging. All these sources have various limitations such as spectral range, pulse duration, repetition rate and high maintenance cost, but laser produced plasma X-rays can be an alternative to the other sources due to its small sources size, high repetition rate and decreasing cost. These properties of laser based X-ray sources make them suitable for high resolution imaging and have the ability to replace the conventional technology already used in clinical

applications. The basic theory of phase contrast imaging can be explained in terms of complex refractive index (n) when electromagnetic radiation interacts with matter. The refractive index is given by

$$\eta = 1 - \delta - i\beta \tag{2.48}$$

Where δ is the phase term and β describes absorption term. The different behavior of δ and β for different wavelength makes the absorption effects negligible for some material like tissues, but the phase shift δ makes it possible to detect the features even though the imaginary term β is very small or even zero. In case of the conventional technique the image is entirely due to absorption effects β and contributions due to the real part are not observable. The absorption term β can be used to give the mass attenuation μ coefficient as

$$\mu = \frac{4\pi\beta}{\lambda\rho} \tag{2.49}$$

Where λ and ρ are wavelength and mass density respectively. For an X-ray beam propagating through a medium the phase change and attenuation over a distance z is given by

$$\varphi = \frac{2\pi}{\lambda}\int \delta(z)dz \qquad \text{and} \qquad -\log(\frac{I}{I_o}) = \frac{4\pi}{\lambda}\int \beta(z)dz \tag{2.50}$$

Where I_o and I are the incident and transmitted intensity. X-ray radiation while traveling through medium of varying refractive index, modified by the net electron density, experiences attenuation and phase shift due to photoelectric absorption, coherent and incoherent scattering. The coherent scattering of X-rays

results in a phase change due to refraction and diffraction effects at the boundaries (edges) of various media in a sample. The interference of these different phase components appears at the edges of the object to form an interference pattern also known as the edge effect and can be observed in practice by using an appropriate geometry between the source to object and object to detector. If the detector is very close to the object no phase effects can be observed and image will be due to absorption effects. The phase effects can be recorded only if there is a sufficient distance between the object and detector to see the interference patterns. However if this distance is too large then it will result in degradation of the image resolution. To achieve the best result the source should have spatial coherence, because enhancement is due to small deflection of X-rays from edges within the object. The laser produced plasmas X-rays and synchrotron sources have the ability to provide spatial and temporal coherence which can be used for these experiments. A schematic diagram shown in Figure 2.11 provides a picture of principle of the phase contrast imaging using laser plasmas X-rays in our experimental arrangement.

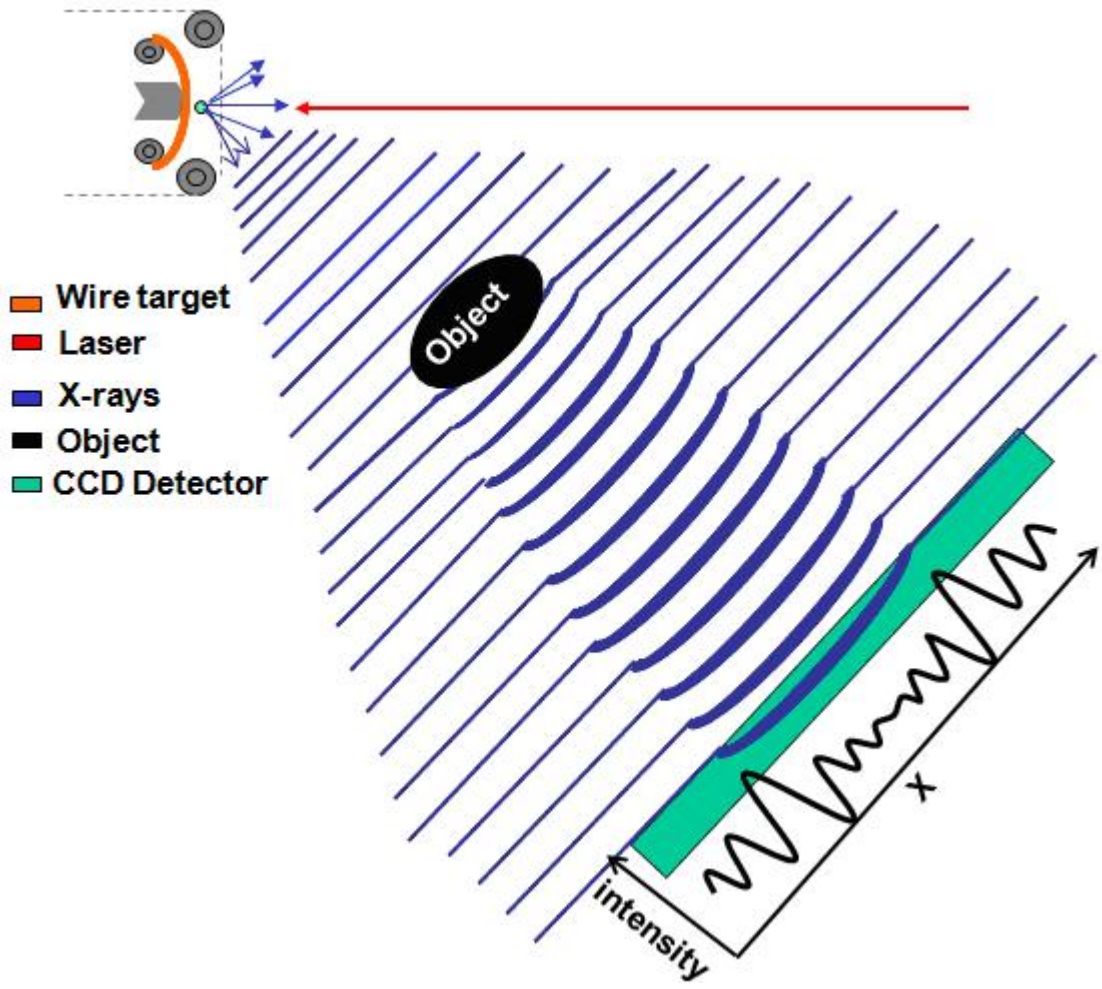

Figure 2.11 Schematic of the principle of phase contrast imaging using X-ray sources.

Chapter 3 EXPERIMENTAL SETUP

3.1 Laser parameters

The experiments are performed using a 130 fs (FWHM) Ti:Sapphire commercial laser system (Spectra Physics, model Hurricane) at 800 nm. The laser consists of a Ti:Sapphire laser oscillator followed by a grating pulse stretcher, regenerative amplifier and a grating pulse compressor. The system can be operated at variable repetition rate starting from single shot to 1 kHz. The maximum laser pulse energy from the system under ideal condition is 750 μJ in TEM_{oo} mode.

Low energy pre-pulses prior to main pulse are a normal consequence of the regeneration amplifier in femtosecond lasers. The laser system generates pre-pulses before the switch out of main pulse by itself in the regenerative Ti: Sapphire amplifier stage as a result of leakage through the Pockels cells. This leakage laser light is intense enough to form pre-plasma in front of target material, which is an important factor to consider and understand in the case of laser matter interaction. The round trip time between two consecutive pulses is 8.5 ns, therefore the pre-pulse leaks out 8.5 ns before the main pulse. The ratio of energy of pre-pulse to main pulse is known as the contrast ratio and is used to characterize the pre-pulse. A contrast ratio of about 8×10^{-4} is observed using a fast photodiode (FND-100) and varies depending on laser operating parameters.

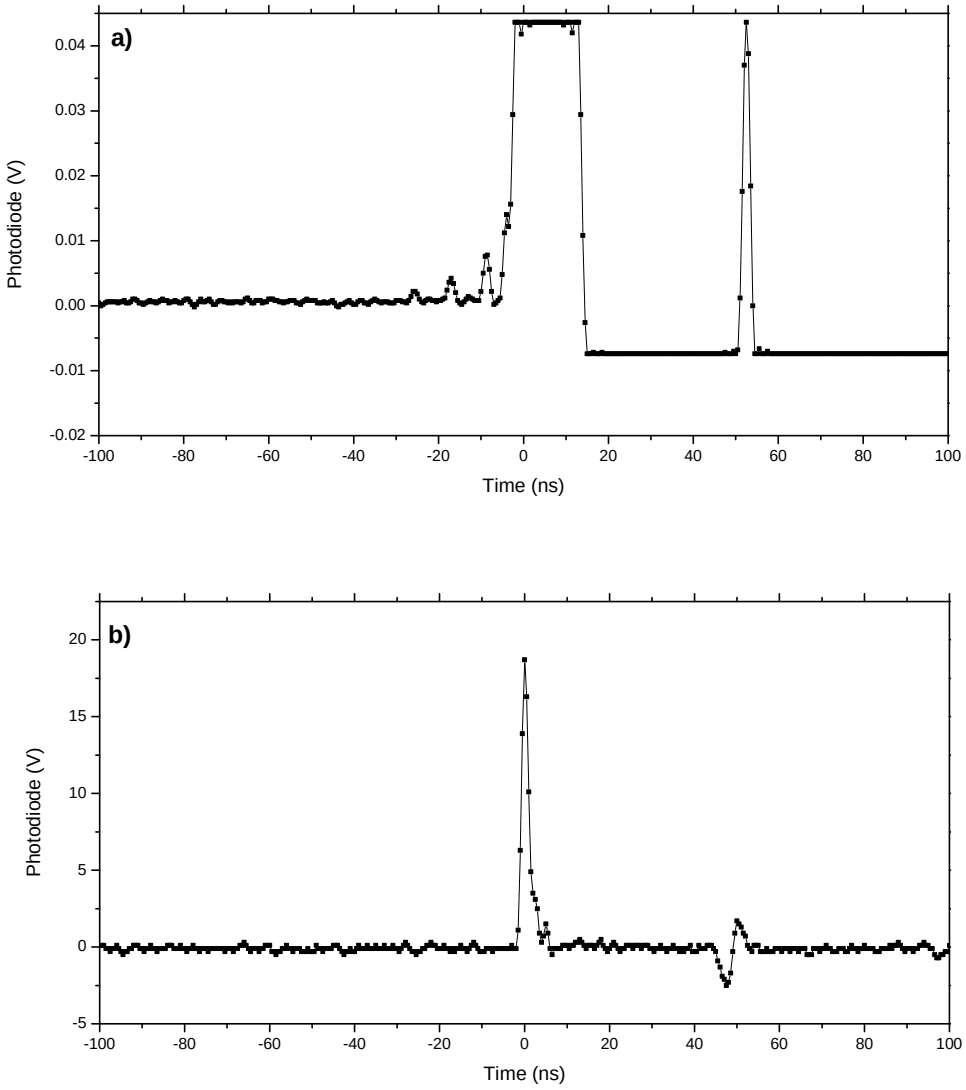

Figure 3.1 Laser Pre-pulse measurements using photodiode a) Pre-pulse train b) Main pulse. The measurement provides a contrast ratio of 4.6×10^{-4} between the pre-pulse and main pulse.

The most recent measurements provide a contrast of about 4.6×10^{-4} with a prepulse of 8.5 mV and a scaled main pulse 18.7 V. The measurements of prepulse and main pulse using photodiode are shown in Figure 3.1. To monitor shot to shot fluctuation of laser energy on metal targets, we employed a

photodiode performed cross-calibration a power meter (Spectra physics Model 407A). A single shot autocorrelator was used to measure pulse duration (FWHM) of the femtosecond pulse assuming the temporal profile has a Gaussian pulse shape.

3.2 Laser focal spot measurement

A 10X microscope objective (Newport), with numerical aperture of 0.25, working distance of 5.5 mm and focal length of 17 mm was used to focus laser pulses onto the metal wire targets. The spot size measurement of input laser beam (laser beam in front of objective) have been done in the past within the University of Alberta group using the knife edge technique providing a beam radius (ω_{01}) of 3.56 mm which gives a spot size of 4.20 mm at full width half maximum (FWHM). The new beam radius (ω_{02}) at lens focus can be calculated using the equation 3.1.

$$\omega_{02} = \frac{\lambda}{\pi} \cdot \frac{f}{\omega_{01}} \frac{1}{\sqrt{1+\left(\frac{f}{z_{R1}}\right)^2}} \tag{3.1}$$

Where λ is the wavelength of the laser, f is the focal length of the microscope objective and $z_{R1} = \frac{\pi \cdot \omega_{01}^2}{\lambda}$ is the Rayleigh range of the incoming laser beam.

The beam diameter at full width half maximum (FWHM) is given by

$$d_{FWHM} = \sqrt{2\ln(2)} \cdot \omega_{02} \tag{3.2}$$

Using the input laser beam waist (ω_{01} = 3.56 mm) we expect a beam diameter at FWHM $d_{FWHM} = 1.4\mu m$.

The measurement of laser spot size at focus was carried out with 10X microscope objective (Newport) as shown in Figure 3.2. The Newport microscope objective has a clear aperture of 8 mm to pass the Gaussian laser beam without severe power losses. The spatial distribution of laser was measured using an imaging source CCD (DMK 31BF03) which has 4.56 μm × 4.56 μm pixel size. The CCD was attached further attached to a 16 cm beam tube and a 10X, 0.25 numerical aperture (NA) Edmund microscope objective to obtain a ~16 times magnified image of focused laser spot. The laser intensity at the focus was high enough to damage the CCD chip. In order to make it acceptable for CCD, we used neutral density filters (Schott NG) to reduce the intensity of laser beam.

A calibration was performed to measure the resolution of our diagnostic CCD camera using a USAF 1951 test target (Edmund) as shown in Figure 3.2 (d). The element 7 in group 6 is resolved at 228 lines pairs per mm corresponding to a line spacing of 4.38 μm. The vertical and horizontal line out profile along 228 line pairs per mm is shown in Figure 3.2 (e) and (f) respectively providing an average of 7.75 pixels between two lines. Dividing the spatial separation of 4.38 μm by 7.75 pixels provide a calibration of 0.56 μm/pixels. We use this calibration number to calculate the focal spot size of the laser beam. The measured spot size (FWHM) along the x-axis and y-axis is 2.44±0.15 μm and 2.43±0.15 μm respectively as shown in Figure 3.2 (c) and (d). The laser pulse energy of 290 μJ

with a 130 fs pulse duration provides a peak laser intensity of ~ 4×10^{16} W/cm^2 for a focal spot size (FWHM) of 2.44 μm.

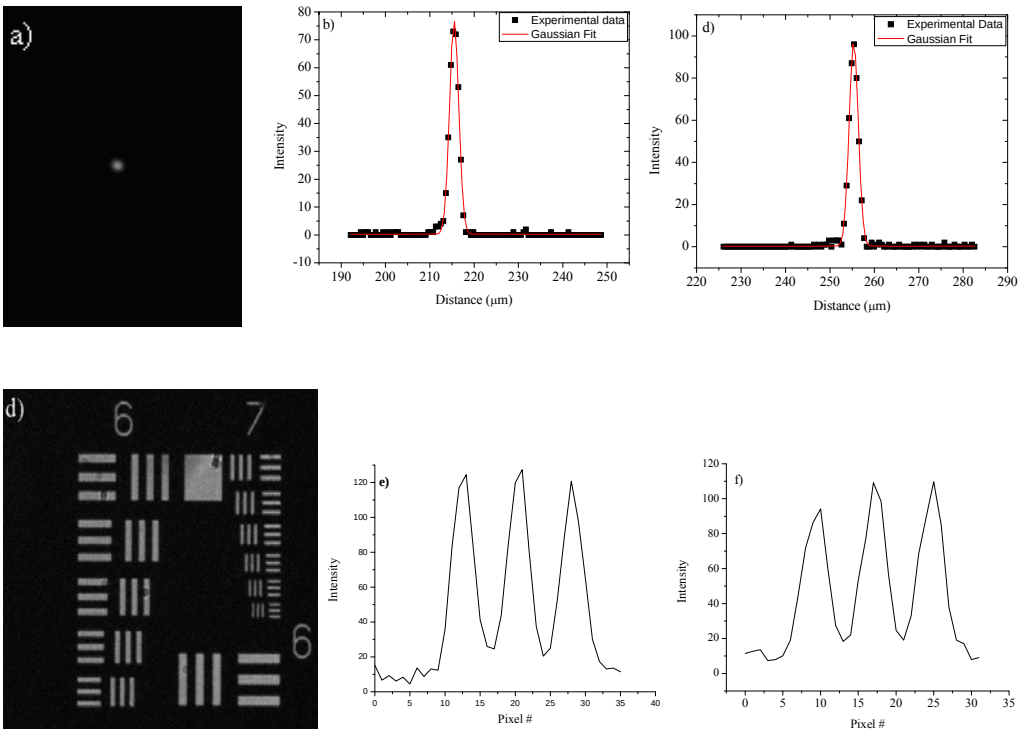

Figure 3.2 Laser beam spot size measurement (a) Laser focal spot size with ~ 16 times magnification onto the CCD (b) The beam profile along x-direction fitted with a gaussian function to get an focal spot size (FWHM) 2.44±0.15 μm. (c) The beam profile along y-direction fitted with a gaussian function to get an focal spot size (FWHM) 2.43±0.15 μm. (d) USAF Resolution test target element 7 used which is 228 lines pairs/mm (4.38 μm) (e) Vertical scan along 228 line pairs per mm of USAF 1951 resolution targets gives an average of 7.75 pixels per line spacing. (f) Horizontal scan along 228 line pairs per mm of USAF 1951 resolution targets gives an average of 7.75 pixels per line spacing.

3.3 Description of Experimental system

The experiment was designed to study K_α emission using a target system which can be operated continuously at 1 kHz. The design of the target system has

different considerations for single shot and high repetition rate laser systems. It is difficult to replace the target for each laser shot, but in the meantime the target should be moveable to provide fresh surface for each laser shot. The tight focusing of laser on target is very sensitive due to the small depth of focus and requirement to maintain it within the scale of few microns. So the target position had to be stable to ensure laser intensity and spot size would not change for each laser shot.

The copper wire had a diameter of 250 μm and it was continuously spooled on a motorized drive through a guide. The guide has a slot, which allows the wire to move smoothly without much wobbling. An additional tension is applied to one of the spools to guide the wire with a lateral movement of less than 10 μm. A 10x microscope objective has been used to focus the laser beam on the wire to an intensity of ~ 4 x10^{16} W/cm^2 for a laser energy of 290 μJ on the target. Given the wobble of the target of approximately 10 microns and the F/4 focusing giving a Rayleigh range of approximately 8 microns, the real laser intensity would vary in the range of 4 x10^{16} W/cm^2 down to approximately 1 x10^{16} W/cm^2 with an average value of 2.5 x10^{16} W/cm^2 for the X-ray measurements.

The tight focusing of laser pulses onto metal surfaces results in emission of plasma and debris, which is target material expelled by the laser pulses. The emission of this material is a real issue in terms of damage to sensitive optical surfaces and coatings on the focusing optics and reduces the laser transmission of these optics. This problem was resolved by continuously running a plastic tape of

30 μm thickness between the target and the focusing objective to avoid debris deposition onto the objective lens. The plastic tape also has a motorized spooling mechanism, which allows for fresh shield surface for the objective lens and thus provides a clean path to every single incident laser shot on the target. The wire speed is adjusted so that the incident beam interacts with a fresh surface on the target even at 1 kHz laser repetition rate. The wire target, plastic tape shield, and the objective lens are housed in a vacuum chamber, which is evacuated to a pressure of 0.1 torr. An x-ray pin diode (Quantrad: 100-PIN-125) is mounted inside the chamber to measure x-ray flux on the sample. It was placed at a distance of 51 mm from the source in the direction of 57^{o} from the target normal. The pin diode is covered with a pair of 15 μm Ni and 9 μm Al filter foils. This will ensure the x-ray flux measurement at Cu-K_{α} energy. The Pin diode also had two identical permanent magnets of strength 0.3 T in front of diode assembly to deflect fast electron and avoid their contribution along with X-ray photons.

Fig. 3.3 shows the experimental setup used for this study. X-rays from the source exit the vacuum chamber via a 75 μm thick Mylar window. An Andor X-ray CCD camera (model: DO 420) has been used to record the phase contrast images of the object. It is mounted on a small vacuum chamber evacuated by a turbo molecular pump to avoid oil contamination on the CCD camera detector chip face. This chamber also has a small entrance window of Mylar film (thickness 50 μm) for the X-rays. The CCD detector is covered with a 15 μm

thick Ni foil to allow exposure by Cu K_α emission and it also blocks room light falling on the CCD.

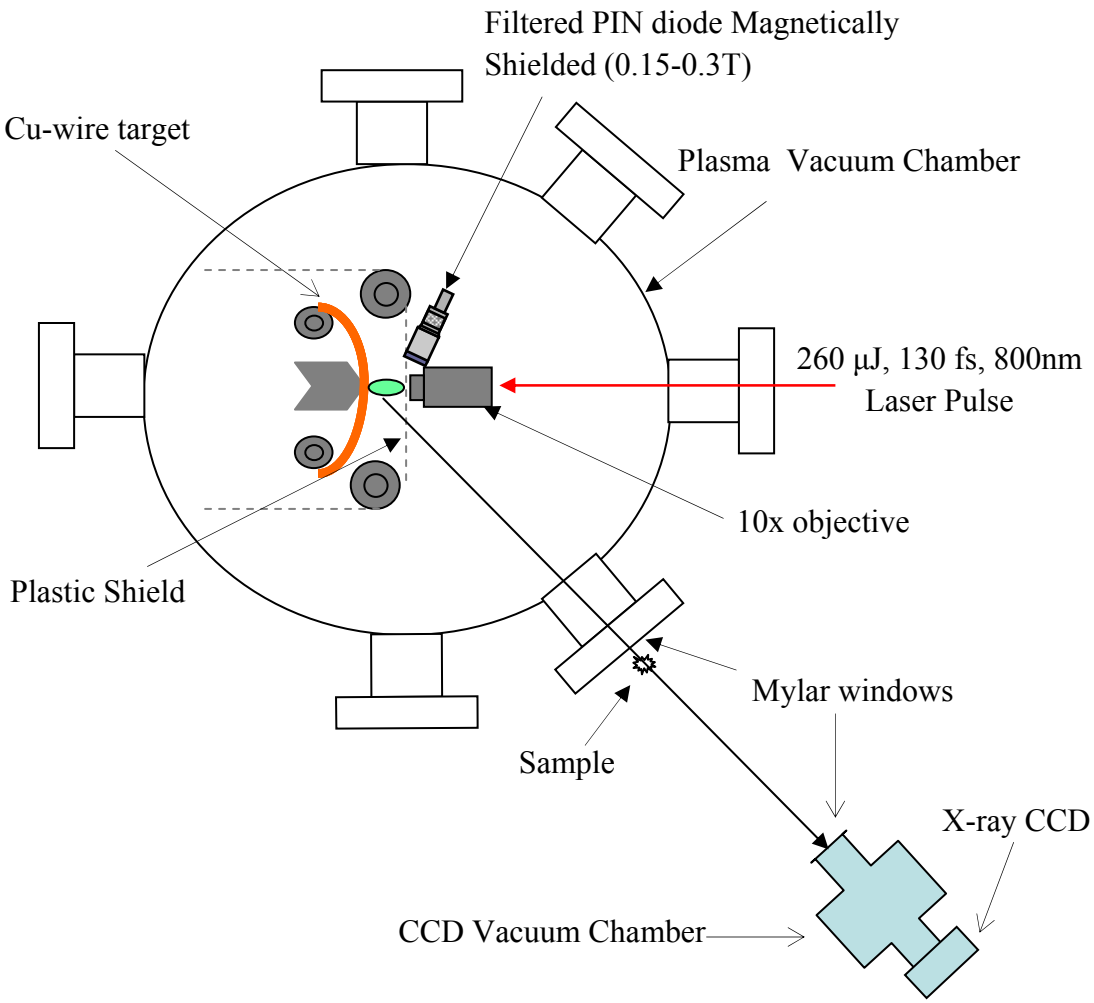

Figure 3.3 Schematic representation of experimental setup

The Ni filter was replaced by 25 μm Al foil for the Fe K_α source and later on was replaced with a light tight 9 μm Al foil permanently to block the room light. The camera is cooled to - 20^{o}C in order to reduce the dark counts and therefore it is necessary to operate it in vacuum to avoid water condensation on the CCD array.

3.4 X-ray Detectors and their diagnostics

The measurements of X-ray emission from laser interaction with matter were carried out with a Silicon Pin diode detector, a pulse height analysis system using a Cadmium Telluride (CdTe) diode detector with multi channel analyzer (MCA) attached and an Andor Charge Coupled device (CCD) detector. All these detectors are based on semiconductor technology and the fundamental principle is the same for all except with different photon sensitivity based on the quantum efficiency of the semiconductor chips. The Pin diode detector consists of an active layer of 250 μm of silicon along with 0.3 μm thick silicon entrance window. The interaction of X-ray photons with silicon atoms produces electron-hole pairs (requiring an average 3.62 eV photon energy to create one electron hole pair) through photoelectric effect and Compton scattering mechanisms depending on X-ray energy. The peak sensitivity of the Pin-photodiode detector is 0.276 C/J for X-ray photons as given by the manufacturer data sheet and theoretical response of the detector versus photon energy is calculated from the Silicon absorption data given at National Institute of Standards and Technology (NIST) [93] and Lawrence Berkeley National Laboratory [94] websites as graphed in Figure 3.4. The detector was covered with appropriate filters to block the unwanted spectrum of X-rays. The sensitivity S(E) of Pin diode covered with metal foils can be calculated using basic sensitivity of detector (s(E) = 0.276 C/J for Pin-photodiode) and transmission of the foil filter corresponding to the given photon energy.

$$S(E) = s(E) \cdot T(E) \tag{3.3}$$

The transmission of metal foils was calculated using the exponential absorption law given by

$$T = \frac{I}{I_o} = \exp(-\alpha \cdot m_A) \tag{3.4}$$

Where I_o is the incident intensity and I is the transmitted intensity through a layer of material with areal mass density m_A which is the product of density ρ and material thickness l i.e $m_A = \rho \cdot l$ and α is mass attenuation coefficient defined as the quotient of the attenuation coefficient μ and density ρ of material. So the above relation can be written as

$$T = \frac{I}{I_o} = \exp\left[-\left(\frac{\mu}{\rho}\right)\cdot(\rho \cdot l)\right] \tag{3.5}$$

For the detection of Cu K_α X-rays a pair of metal filters of 9 μm Al and 15 μm Ni were used, which provide a window from 6.5 to 8.3 keV around the Cu K_α (8050 eV) energy line. The sensitivity of the bare Pin diode and when corrected for a combination of 9 μm Al and 15 μm Ni filters are shown in Figure 3.4 a) and b). In some experiments a 25 μm Fe foil was also used in front of pin diode to block the low energy photons as well as the Cu K_α and K_β lines emitted from laser produced copper X-ray source. The response curve of the pin diode filtered with 25 μm Fe is plotted as function of X-ray photon energy shown in Figure 3.5.

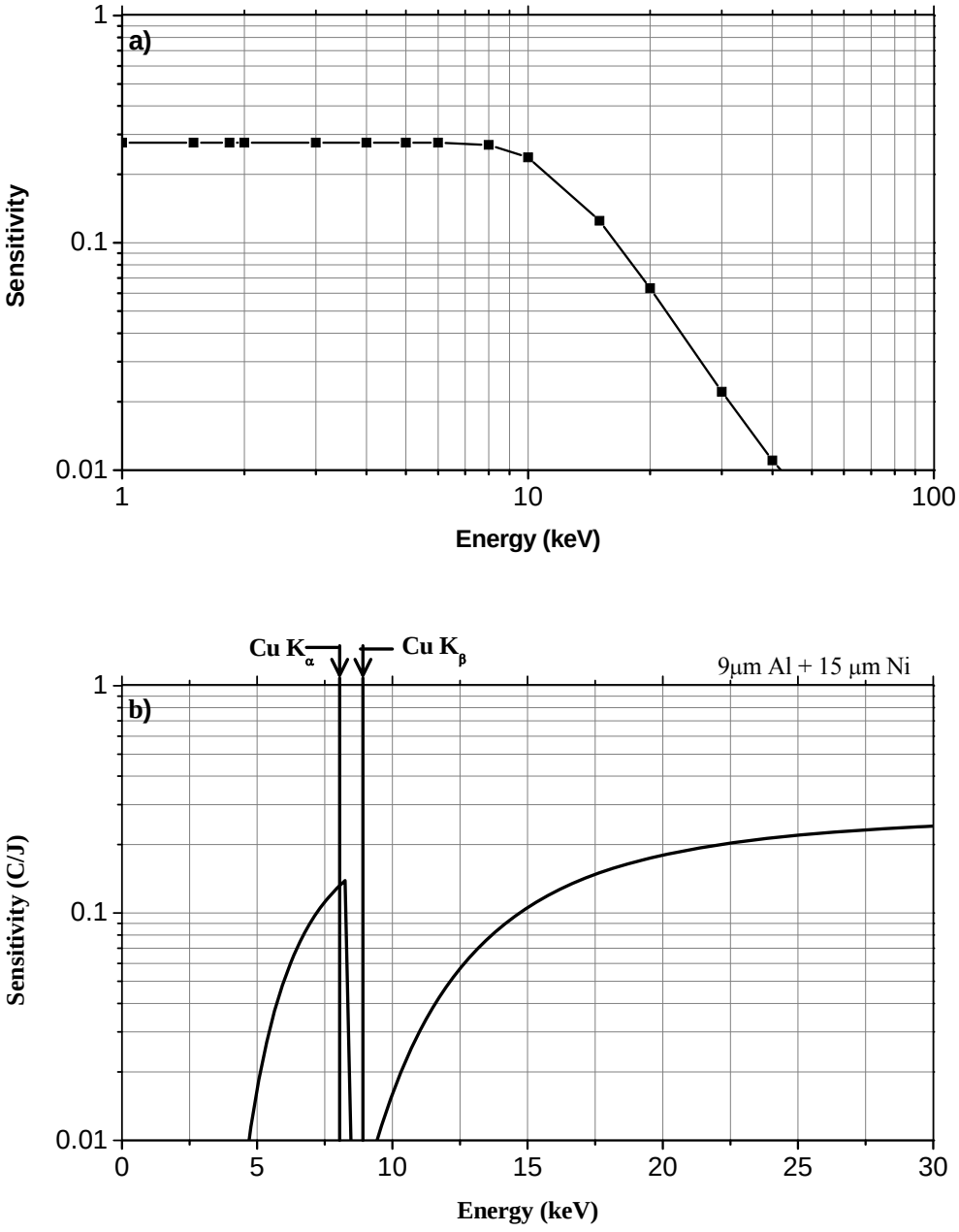

Figure 3.4 The response function of a) pin diode without filtering and b) Pin diode with a combination of 9 μm Al and 15 μm Ni foil filters. The Cu K_α and K_β lines are also shown for reference in (b)

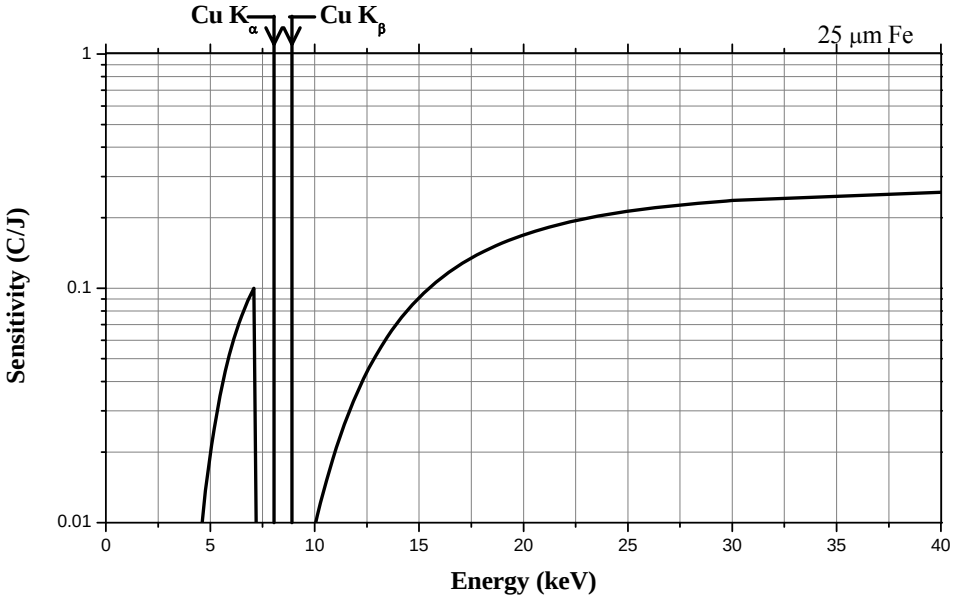

Figure 3.5 Spectral sensitivity of the pin diode covered with 25 μm Fe foil. The Cu K_α and K_β lines are also plotted for comparison.

The experiments performed in this work also used a solid-state detector (XR-100T-CdTe, AMPTEK, Inc) to record the X-ray spectrum of different metal targets. This is a diode type Cadmium Telluride (CdTe) detector with a thickness of 1 mm. The X-ray photons create one electron-hole pair per 4.43 eV of energy deposited when they interact with the CdTe crystal. The energy loss process depends on the photon energy and is dominated either by photoelectric effect or Compton scattering. A high voltage of about 400 to 500 volts is applied across the detector to collect of these electron/hole pairs at room temperature. This high voltage operation at room temperature can result in excessive leakage current and cause breakdown. To minimize these effects, the detector is thermoelectrically cooled and thus can be operated at high voltage. The detector is then attached to

Rise Time Discrimination (RTD) circuit to avoid charge collection time fluctuations due to electron/hole interaction with the CdTe close to back contact of detector. These fluctuations generate a spectrum with huge background and lower resolution. The function of RTD is to filter out these fluctuations and only pass the full charge collection events to Multichannel Analyzer (MCA) for acquisition and analysis. This MCA is further connected to a PC to generate data in the form of a pulse height histogram.

The detector is covered with a 100 μm (4mil) thick Be window to block the low energy photons and background light. The Figure 3.6 and 3.7 show the transmission of 100 μm Be window and efficiency of CdTe detector as a function of photon energy respectively. The efficiency of CdTe detector for 4mil (100 μm) Be window is almost constant (98 to 100%) for the energy range between ~ 8 to 60 keV and starts to drop down around 60 keV. The beauty of CdTe detector is that it operates on the principle of single photon detection. If more than one photon reaches the detector during the readout time, the histogram shows this as a multiple of the original photon energy. For example, Cu K_α has its peak at 8.05 keV, but if two photons arrive at the detector at the same time a second peak will appear at $2 \times 8.05 = 16.1$ keV and so on. Such double or triple photon peaks are known as 'pile up' and make experimental interpretation difficult. It is necessary to avoid this pile up in order to get accurate experimental data. It is possible to achieve good single photon spectra by reducing the size of detector through the

use of a small pinhole in front of detector, by filtering high photon flux rate and by increasing the distance of the detector from the source.

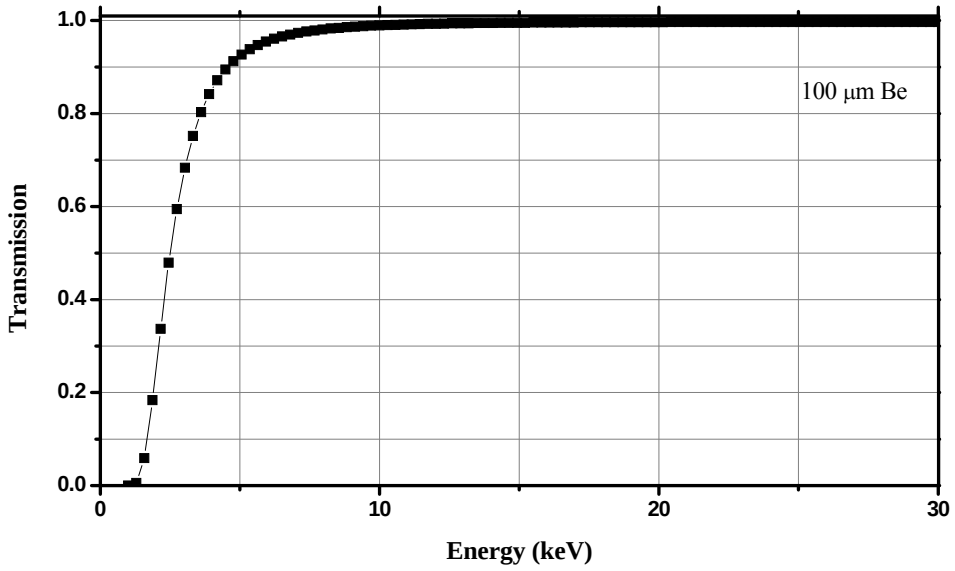

Figure 3.6 Transmission of 100 μm beryllium window versus X-ray photon energy

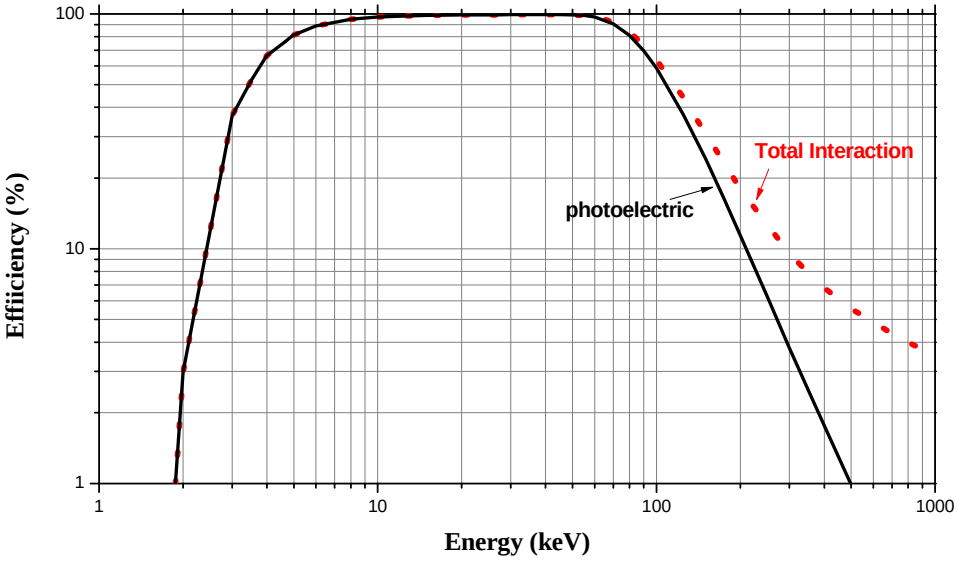

Figure 3.7 CdTe detection efficiency for a 1 mm thick detector [95]

We normally optimized the X-ray K_α source by scanning the microscope objective and target up to a point, when the filtered Pin-diode (reference) detector gives highest photon flux. After determining the optimum condition the X-ray spectrum was recorded using the CdTe detector. The spectrum obtain from detector provide data in the form of counts as a function of channel numbers (bin #). A calibration is required to convert these channel numbers into corresponding photon energies. For this purpose a ^{241}Am X-ray emitter was used to record the spectrum. The spectroscopic data of ^{241}Am source provide standard peaks at 13.95 and 59.54 keV. We utilized these peaks for calibration of Iron (6.4 keV), Copper (8.05 keV) and Silver (22.2 keV) K_α peak energy. The measured calibration spectrum of ^{241}Am radioactive source is shown in Figure 3.8.

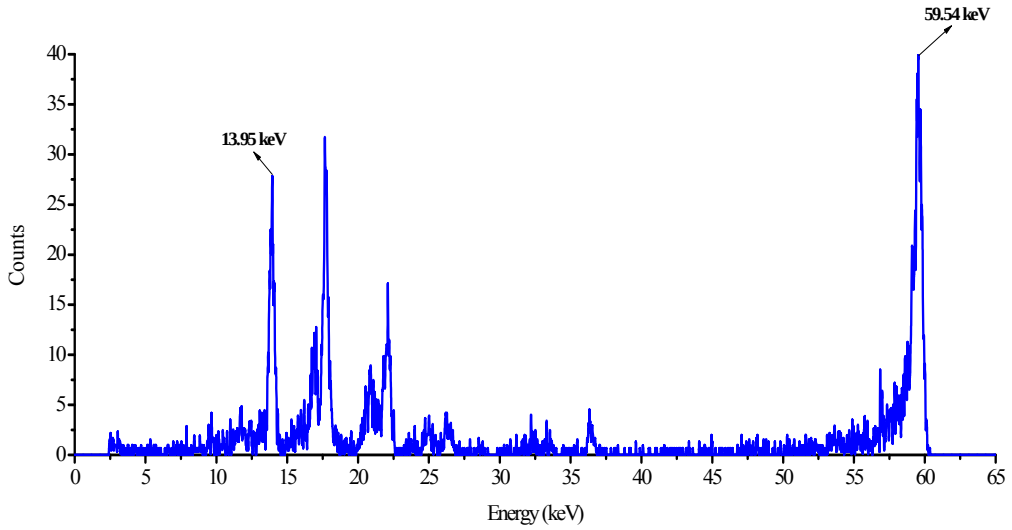

Figure 3.8 ^{241}Am spectrum taken with the XR-100T-CdTe detector for calibration

The Amptek detector has a variable gain setting and calibration is valid only if K_α source measurements were done at the same analog gain setting. The energy resolution of the spectrum is of hundred of the order of electron volts (eV), which is approximately 390 and 600 eV for 13.95 and 59.54 keV respectively. This resolution is not enough to distinguish the double structure of K_α line but it can be resolved using an X-ray diffraction crystal and a CCD detector. To record a spectrum of the silver X-ray source using the Amptek detector a combination of 381 μm Al and 25 μm Fe filter foils was used for filtering. This pair of foils was able to block the low energy part (<10 keV) of the spectrum as indicated in the transmission plot of Figure 3.9.

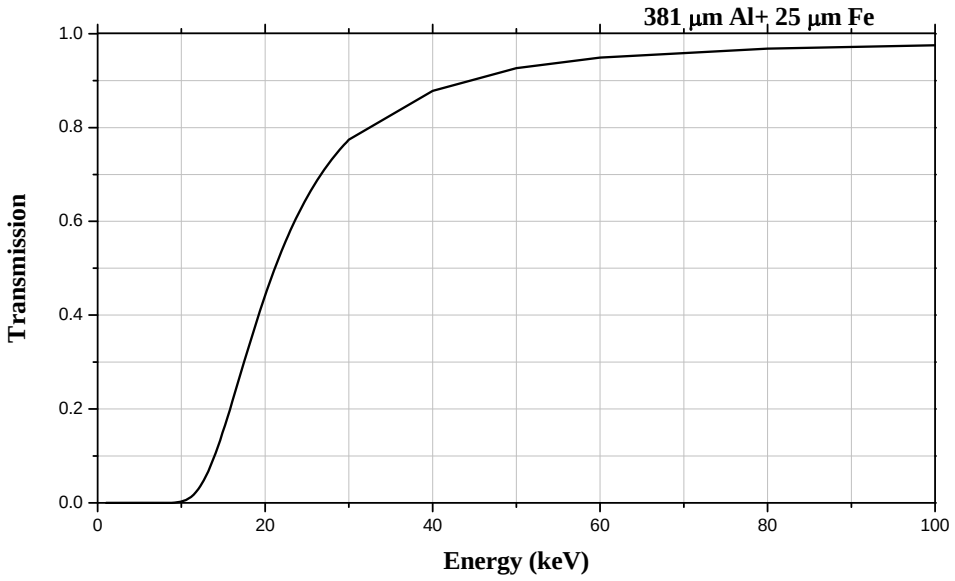

Figure 3.9 Transmission of combination of 381 μm Al and 25 μm Fe foils

A CCD detector (Andor Model DO420) was also used for the detection and characterization of the K_α sources and its application in phase contrast imaging. The basic principle of detection of for the CCD is similar to the other semiconductor detectors. The high quantum efficiency, digital signal output and fast data processing make these devices an excellent alternative to imaging plates and photographic films. The working principle of this device is to capture and collect the photoelectrons into individual cells (pixels) by an electrode structure when the incident photons interact with sensitive depletion region to generate electron-hole pairs. A schematic of front illuminated (FI) CCD is shown in Figure 3.10.

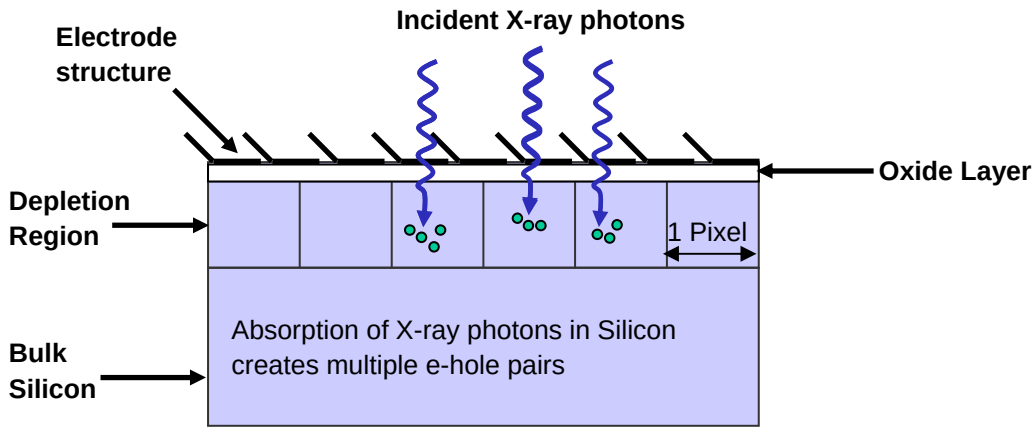

Figure 3.10 Schematic diagram of direct detection of X-ray photons.

The CCD used in our experiments is back illuminated (BN) which is reverse in structure in the way that X-ray photons interact with the thin silicon layer (~20 μm) and electrode assembly is on the back of the silicon to store and move these photoelectrons. The BN-CCD detectors have advantage over FI-CCD due to

higher efficiency and provide better protection against damage by hard X-rays. The quantum efficiency of BN, FI and FI-DD (front illuminated deep depletion) is given in Figure 3.11 as per manufacturer specification [96].

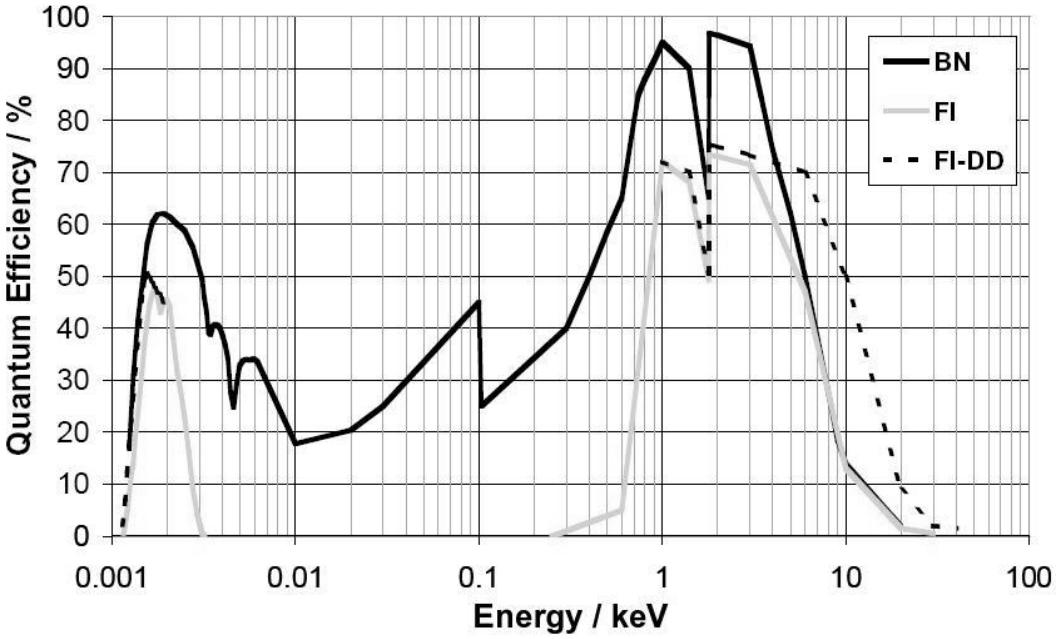

Figure 3.11 Quantum efficiency curves of BN (back illuminated), FI (front illuminated) and FI-DD (front illuminated deep depletion) CCD taken from manufacturer specifications.

The detection efficiency of the BN detector is higher than other two types and reaches maximum (> 95%) at 1 keV and between 2 and 3 keV. The probability of detection of X-ray photons above 6 keV up to 20 keV is same for BN and FI CCD, because at higher energy photons can penetrate up to the depletion layer and attenuation by the electrode is negligible. The direct detection of X-ray single photons is limited to photon energies up to approximately 20 keV and indirect

methods such as additional fluorescer layers are required to detect harder X-ray photons using CCD's.

The important parameters of a charge couple device for X-ray detection are quantum efficiency and dark current. The dark current is a function of temperature as shown in Figure 3.12. The BN type CCD has two-times higher dark current than the FI, but 100 times less than FI-DD type detector. We were operating CCD at –20 ^{o}C with a dark current of 3 electrons per pixel per second. The Andor model DO420 BN CCD used in our experiment has 1024 x 256 active pixels with each pixel 26 x 26 μm in size. The CCD is mounted on a separate small vacuum chamber to avoid the contamination of the chip from water vapor, organic vapor and debris from target material. The CCD vacuum chamber has a 50 μm Mylar entrance window facing towards X-ray source chamber, which has another 75 μm Mylar film to separate the vacuum and air. The air path between the source and the CCD is ~ 74 cm. The transmission of 125 μm Mylar film and air path is plotted in Figure 3.13 and 3.14 respectively.

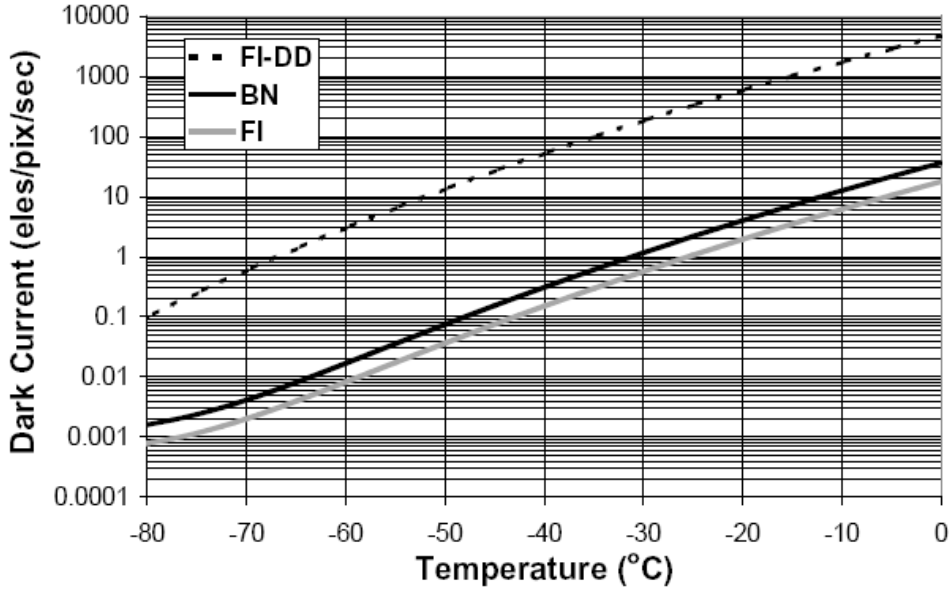

Figure 3.12 Dark current as a function of temperature of BN (back illuminated), FI (front illuminated) and FI-DD (front illuminated deep depletion) Andor CCD.

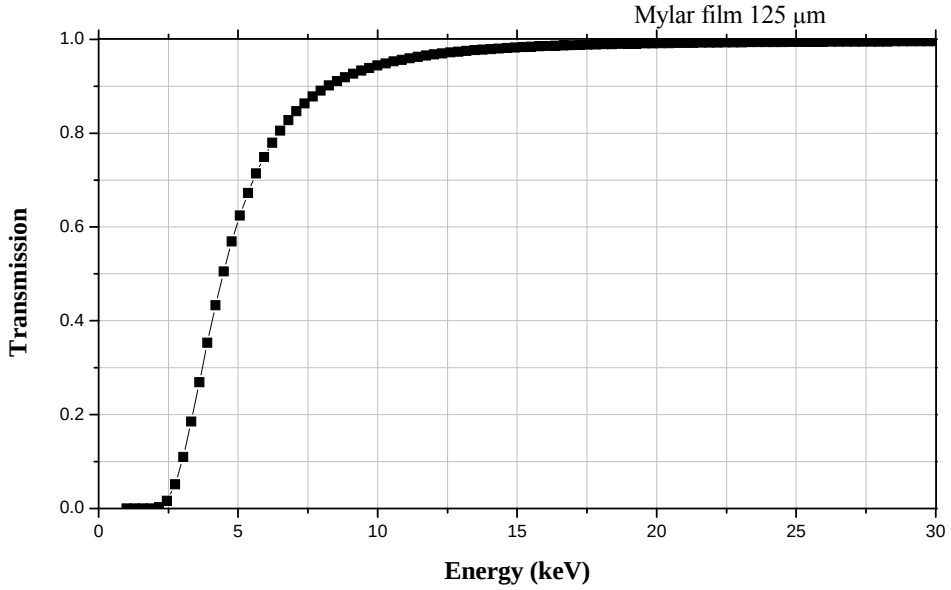

Figure 3.13 Transmission of (75+50 = 125μm) Mylar film used in the path of CCD.

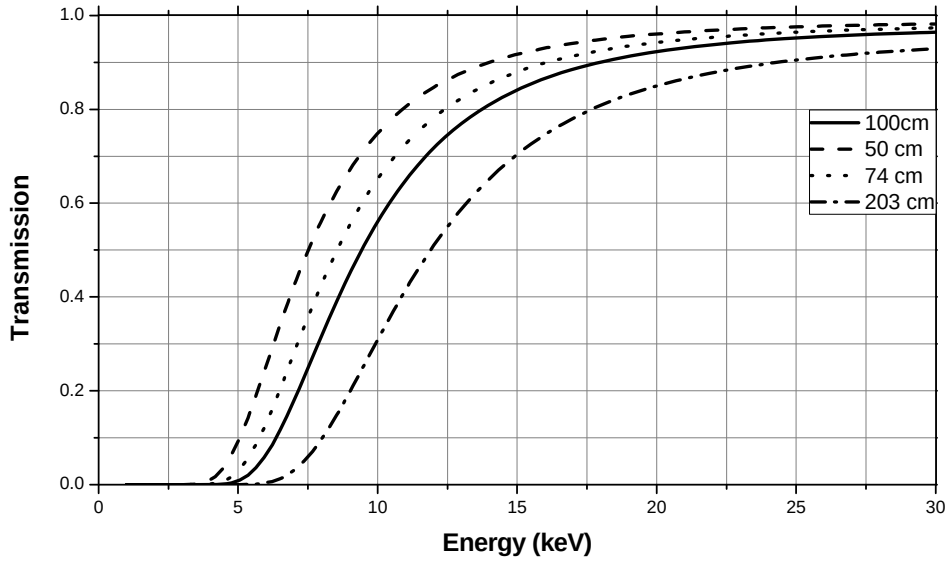

Figure 3.14 Transmission of air path of 50, 74, 100 and 203 cm used in experiments for the CCD and Amptek detectors.

Chapter 4 EXPERIMENTS RESULTS AND DISCUSSION

The main objective of this work is to develop a stable, quasi-continuous hard X-ray source using femtosecond laser pulses at a kilohertz repetition rate. The description of the laser system along with experimental setup has been discussed in detail in chapter 3. The Characteristic and continuum emission from different metal wire targets such as copper, iron (Stainless Steel) and silver were measured using three different detector systems. The measurement of these X-ray sources included analysis of the spectrum to obtain photon numbers and conversion efficiency. This chapter also includes a detailed discussion of short pulse laser generated line and bremsstrahlung spectra from different metals along with its application to phase contrast imaging.

4.1 Copper K_α Source

The development of Cu K_α Source has been studied extensively using flat and rotating disc targets in past experiments within the University of Alberta group [97]. The laser pulse absorption and X-ray conversion efficiency in vacuum and air was also characterized by the laser wavelength, focusing condition, irradiance, polarization and angle of incidence.

The present study of X-ray emission has been performed using different metal wires of different size instead of using disk targets. For the first series of experiments, copper wire with 250 μm diameter was used as a target to shine laser beam using focusing optics to generate particles and X-rays. Iron (Stainless Steel) and Silver wires having diameters of 250 μm and 400 μm respectively were used as targets for the generation of laser produced X-rays at different wavelengths and will be discussed later in the chapter. The study of X-rays includes continuum bremsstrahlung, recombination and line radiation using charge coupled device, Amptek XR-100T-CdTe and pin-diode detectors. The plasma X-ray source is produced by focusing the 1 kHz laser pulses of energy between 35 to 300 μJ onto the Cu, Fe and Ag wire targets. Measurements carried out using p-polarized laser light focused with 10x microscope objective (Newport) and at an angle of $0^{o}\pm5$ from target normal. K_{α} conversion efficiency scaling with laser energy is investigated using the pin-diode, CCD and Amptek detectors and the hot electron temperature was determined from the continuum spectrum of X-rays measured with the Amptek detector. The pin-diode was used as our reference detector for optimization of the X-ray emission. We will discuss K_{α} conversion efficiency along with broadband continuum spectrum in detail. A strong scaling of Cu K_{α} emission efficiency was observed as a function of laser energy using the pin-diode detector. The laser could be operated at different repetition rates from 1 Hz to 1 kHz and the laser energy could be varied by rotating a half-wave plate before a polarizer. The laser was focused using a 10x microscope objective to obtain a

spot size of less than 10μm, which gives an intensity of few times $10^{16} W / cm^2$ on target for a 250 to 300μJ pulse energy. In this intensity regime, laser pulses can deposit significant energy on target to generate fast electrons through multiple absorption processes. Most important in this irradiance regime is resonance absorption and vacuum heating. Pin-diode filtered with 15 μm Ni and 9 μm Al was used to measure a spectral range from ~ 6.5 - 8.3 keV around K_α line. It was placed at a distance of 51 mm from the source in the direction of 57^o from the target normal. The Cu K_α and keV conversion efficiency is well defined by a power law dependence on laser pulse energy. A scaling exponent of ~ 1.87 is observed for the K_α yield with the laser operating at 50 Hz as shown in Figure 4.1, which is consistent with the expected strong scaling [66, 26, 68, 70] for keV X-rays from the plasma.

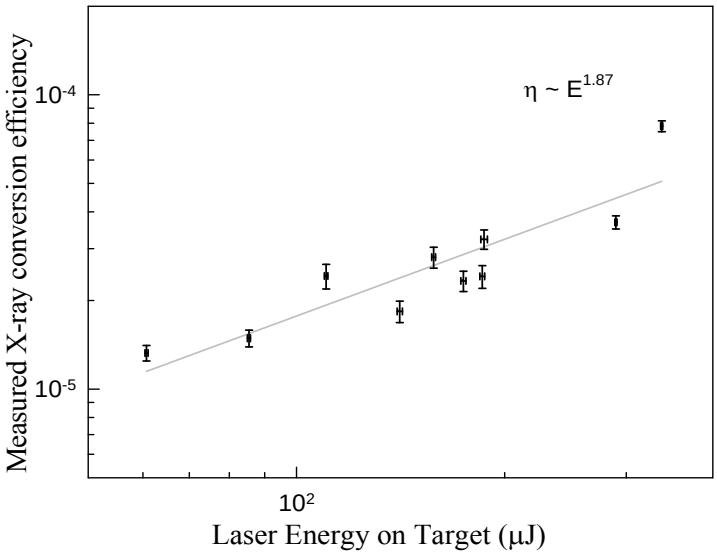

Figure 4.1 Scaling of Cu K_α X-ray conversion efficiency as a function of laser energy on target

The last two data points in the scaling curve were taken at 1 kHz rather than 50 Hz, this increase in conversion efficiency could be due to overlap of laser pulses on wire target giving rise to an increased X-ray yield [22] at 1 kHz.

An average of 4×10^{-5} conversion of Ti:sapphire laser pulse energy into K_α photons was observed assuming isotropic emission in a solid angle of 2π [17].

Spectral characterization of the Cu Kα source has been performed using a CdTe Amptek detector. The X-ray emission is mostly confined to line radiation at 8.05 keV and 8.91 keV corresponding to the well known Cu-K_α and Cu-K_β lines respectively as shown in Fig. 4.2.

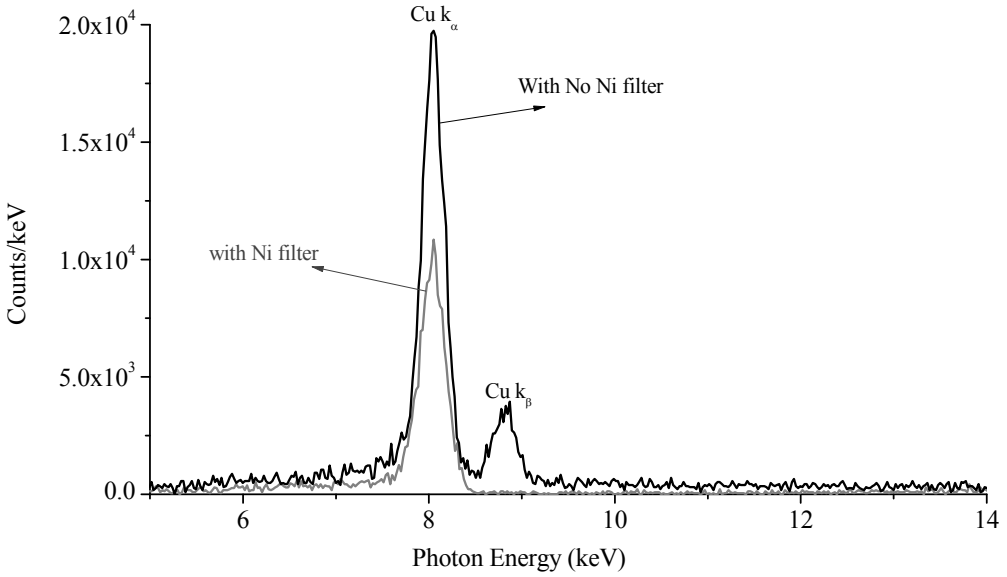

Figure 4.2 Measured X-ray spectrum from a Cu target at E= 290 μJ (with Ni filter) for a 30 sec. exposure at 35 cm from the target and E = 300 μJ (without Ni filter) for a 120 sec. exposure at 84 cm from the target on target.

The detector was at 35 and 84 cm away from micro X-ray source to record K_α and K_β emission spectrum integrated for ~ 30 sec and 120 sec respectively. The emission at Cu-K_β can be cut using a 15 μm Ni-filter (Fig. 4.2), which has an absorption edge at 8.33 keV. The measurements including correction for transmission of the 15 μm Ni filter and air path gives a photon flux of 2.4×10^{9} ph/s into 2π srad with a conversion efficiency of ~ 1.1×10^{-5} at a laser energy of 290 μJ on target and without the Ni filter a photon flux and conversion efficiency of 2.5×10^{9} ph/s and ~ 1.1×10^{-5} with laser energy of 300 μJ on target respectively. These are less than the case of the filtered pin-diode. This is due to two factors: The first is the overlap of broadband radiation along with the K_α line into the pin diode, because the filters allow a spectral window of ~ 6.5 - 8.3 keV to pass through. The fraction of broadband continuum detected by pin-diode can be subtracted using the spectrum of X-rays recorded by the CdTe Amptek detector. The second factor is a saturation which is observed for the CdTe detector at these higher photon fluxes as will be discussed later.

The spectra observed in this laser energy range show that emission of characteristic radiation is primarily due to knock out of bound K-shell electron from neutral atoms within the wire target and these inner shell excitations are mainly due to accelerated high energy electron generated by the short, intense (~ 10^{16} W/cm^2) laser pulses. The continuum component accompanying the characteristics lines of K_α and K_β extends to much higher photon energies. The electron energy distribution characterize by hot electron temperature can be

inferred using Maxwellian distributions. A maximum temperature T_h = 8.74± 0.1 keV was obtained, when the X-ray signal in the range of 10.5 keV to 24 keV is fitted to that from a Maxwellian electron distribution as shown in Figure 4.3. The spectrum was recorded for 600 sec second with 290 μJ pulse energy on target and these high energy photons are the direct contribution from higher kinetic energy electrons. A second spectrum shown in Figure 4.4 was obtained from a Cu target integrated for 900 sec with a laser energy of 300 μJ on target to extract an effective electron temperature of laser energy of 300 μJ on target to extract an effective electron temperature of $T_{hot} = 9 \pm 0.1 keV$ from the linear fit extended to photon energies of maximum 40 keV. The estimated electron temperatures using our laser parameters are consistent with the scaling of hot electron generation from resonance absorption for the non-relativistic regime [63] as shown in Figure 2.7.

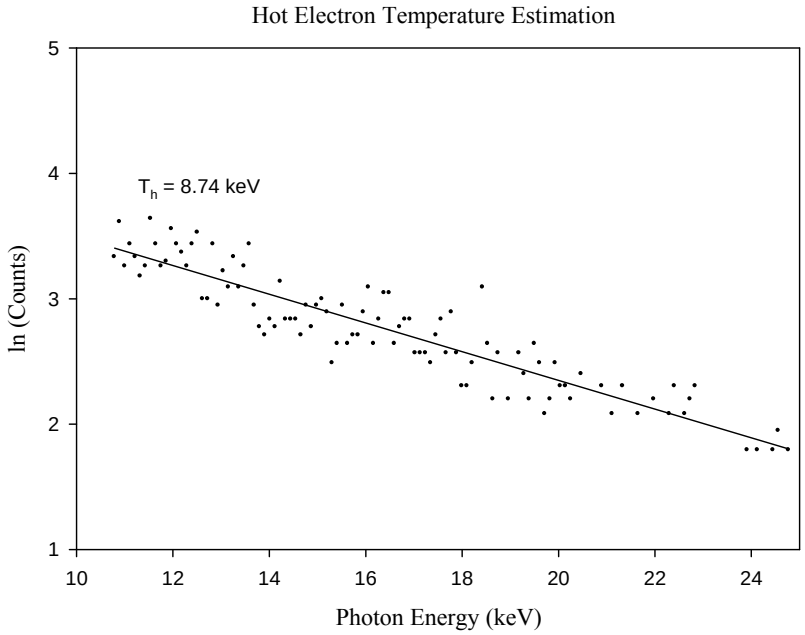

Figure 4.3 High energy tail signal from a Cu target for photon energies from 10 to 24 keV have been fitted by Maxwellian distribution with a characteristic temperature of $T_h \sim 8.74 \pm 0.1$ keV.

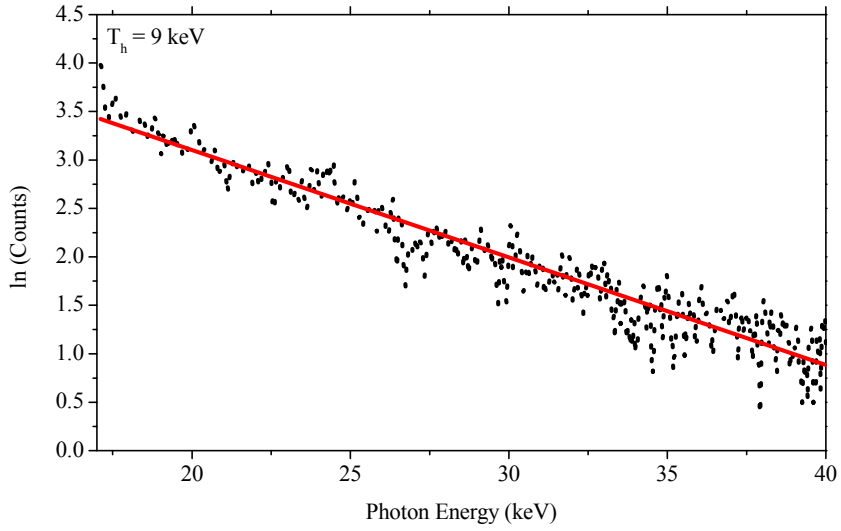

Figure 4.4 High energy tail signal has been fitted by Maxwellian distribution from photon energies 17 to 40 keV with a characteristic temperature of $T_h \sim 9 \pm 0.1$ keV for a Cu target.

The CCD based single photon counting mode technique was also used to detect K-shell radiation spectra with high resolution. The measurements were made with the Andor DO420 CCD detector consisting of a 1024 × 256 array of pixels with 26 μm^2 pixels and operated under a vacuum of 10^{-6} torr. The CCD detector was placed at 134 cm away from the source which includes 74 cm of air path. These measurements were made with 25 μm Al filter to block visible light and low energy continuum emission and to avoid pile-up at higher intensity due to overlap of more than one photon in one pixel. Single photon integrated spectra dominated by emission at 8.05 keV Cu K_α and 8.91 keV Cu k_β line obtained for an exposure time of 1 sec are shown in Figure 4.5. The Cu K_α photon flux corrected for Mylar, Al, air transmission factors and quantum efficiency using this single hit detector for an exposure of 1 second gives 5.3×10^9 ph/s in 2π srad which corresponds to a conversion efficiency of 2.7×10^{-5} into 2π srad with ~260 μJ of energy on target. We also used a 15 μm Ni filter to block the K_β peak at 8.91 keV which gives a clean Cu K_α peak as shown in Figure 4.5 with a photon flux of 7.3×10^9 ph/s for an exposure of 1sec with an average pulse energy of 290 μJ on target. The measured Cu K_α flux corresponds to a conversion efficiency of 3.2×10^{-5}. The calibration of CCD was performed using the manufacturer's data sheet [96] to convert the scale from raw counts to energy (eV) scale. All CCD X-ray measurements were carried out with a read out time 16 μs which results in a gain of 7 e^-/counts. Using this gain of 7 e^-/counts the CCD camera produces 1

count for every 7 recorded electrons. For silicon 3.62 eV photon energy is required to create one electron hole pair. The photon energy and gain factor gives a calibration unit in the form of eV/counts i.e. 3.62 eV/e^-h × 7 e^-/counts = 25.34 eV/counts. The measured peaks of 7.98 keV and 8.84 keV determined from this calibration of CCD are in agreement within experimental error with the expected values of 8.05 keV and 8.91 keV values. This slight shift in peak can be due to drifts in dark current and amplifier gain factors in the CCD camera.

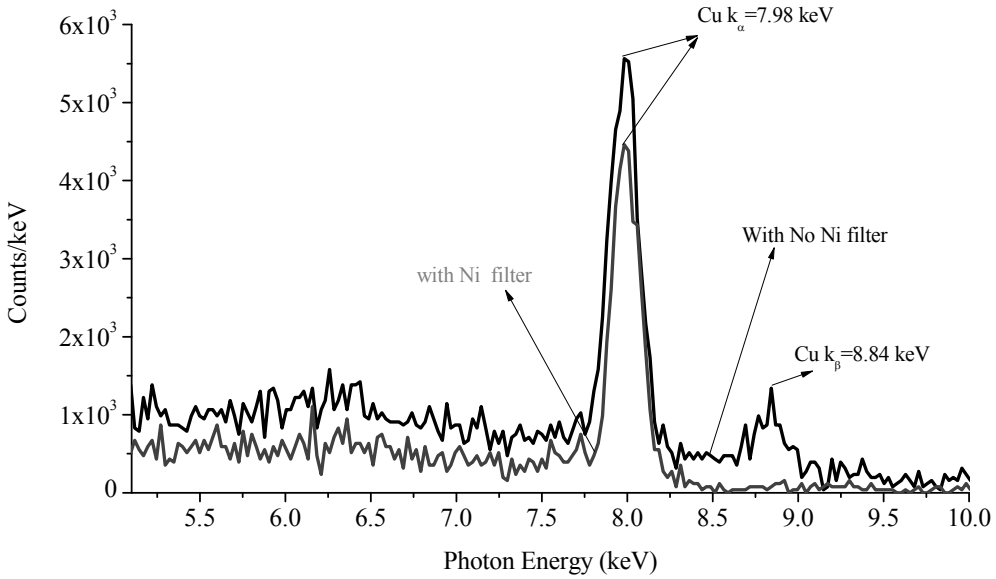

Figure 4.5 The X-ray spectrum showing the Cu K_α and K_β lines measured with a CCD camera in the single-photon counting mode, located at a distance of 134 cm from the X-ray source.

4.2 Iron K_α Source

The single hit CCD camera was used also to measure the spectrum from steel wire targets. The integrated X-ray emission in the Fe K_α line at 6.4 keV and K_β

line at 7.06 keV was determined correcting for attenuation factors and quantum efficiencies. The correction included corrections for the 125 μm transmission of the mylar windows, the 74 cm transmission of air, the 25 μm transmission of the aluminum filter and the 0.46 net quantum efficiency at the 6.4 keV Fe K_α line of the single hit detector. A conversion efficiency of 1.1×10^{-5} from a photon flux of 2.9×10^{9} ph/s into 2π srad is determined for the K_α line of the spectrum given in Figure 4.6.

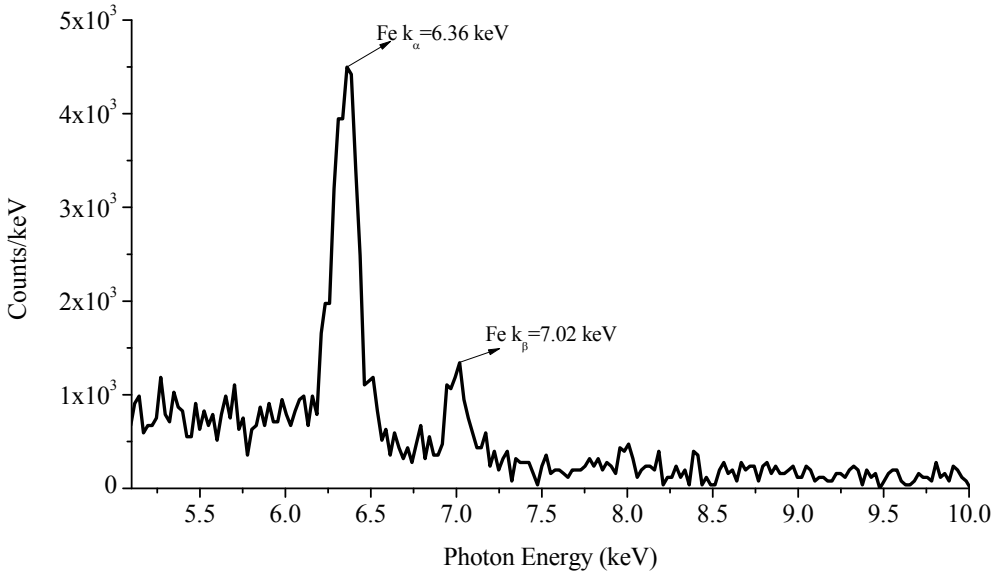

Figure 4.6 The X-ray spectrum showing the Fe K_α and K_β lines is measured with a CCD camera in the single-photon counting mode, located at a distance of 134 cm from the X-ray source.

The spectrum was recorded for an exposure of 1 sec with laser pulse energy of 275 μJ on target. The measured Fe characteristic radiation is dominated by the 6.36 keV K_α line and 7.02 keV K_β line as expected from K-shell emission. The Fe

X-ray spectrum was also recorded using the CdTe detector operating in single photon count mode for an exposure of 30 seconds as shown in Figure 4.7. About 1×10^{9} Photons/s into 2π srad were detected from the Fe K_α line giving a conversion efficiency of 4×10^{-6} for an average laser pulse energy 258 μJ on target operated 1 kHz. The conversion efficiencies measured for Fe K_α source with CCD detector is 3 times higher than CdTe Amptek detector.

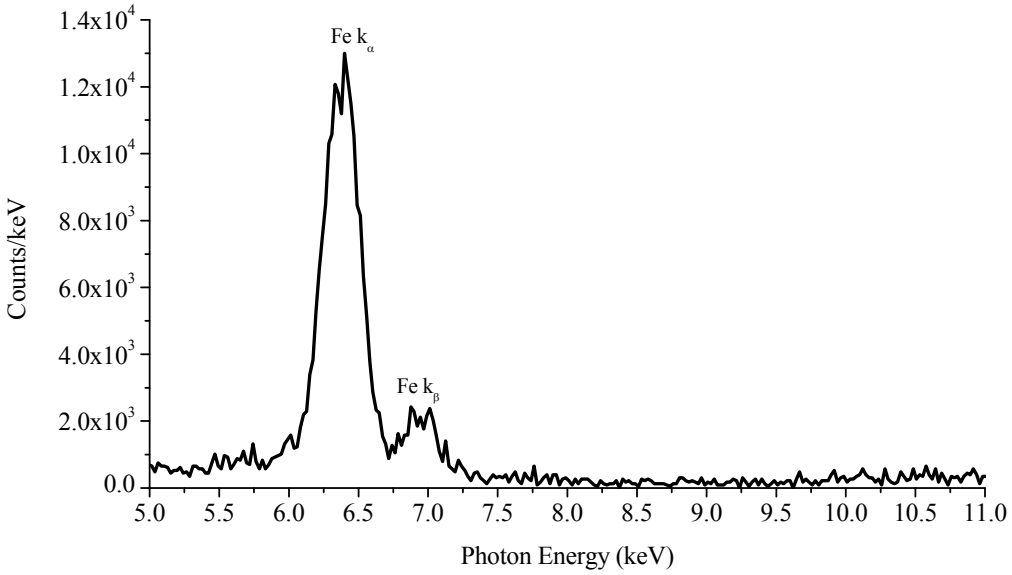

Figure 4.7 X-ray spectrum obtained from a Fe target using CdTe Amptek detector at E=258 μJ for a 30 sec.

The measurements were not performed at the same time and the lower K_α flux obtained from CdTe Amptek detector is due to poor mode quality and focal spot conditions of laser beam for this particular run as clear from the lower Cu K_α conversion efficiency results for the same laser conditions as shown in Figure 4.10. The K_α X-ray yield measured with the CdTe detector and calculated conversion efficiency are plotted as a function of laser pulse energy as shown in

Figure 4.8 and 4.9 respectively for this same run. The Fe K_α X-ray flux (photon/s) grows rapidly with the laser pulse energy operating at 1 kHz repetition rate and reaches up to a maximum of 1×10^9 Photon/s at a pulse energy of 258 μJ on target. Maximum conversion of laser energy into Fe K_α photons of about 4×10^{-6} was observed as shown in Figure 4.9.

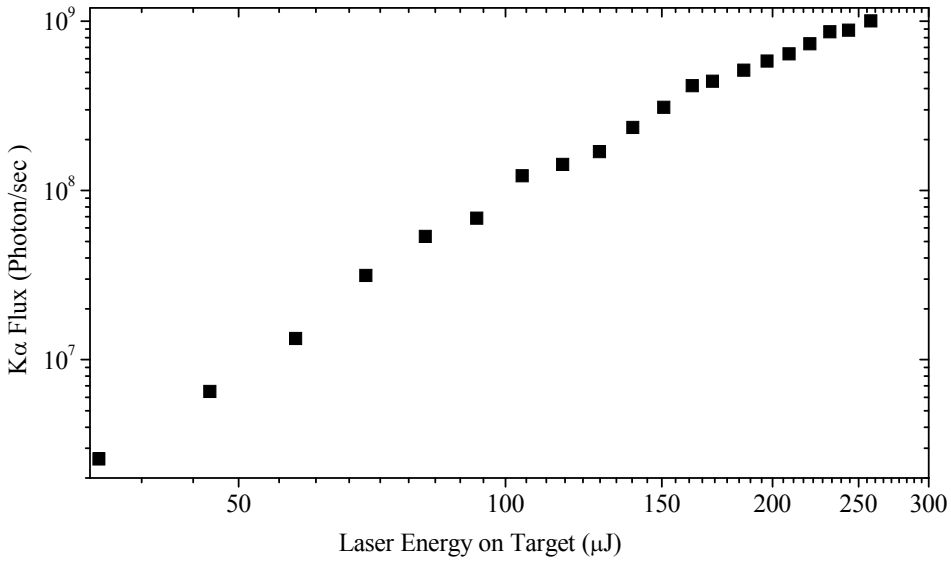

Figure 4.8 Fe K_α yield as a function of laser energy resulting a maximum of 1×10^9 photons/sec.

A power law scaling exponent of 2.52 from 30 μJ to 100 μJ and 0.98 from 160 μJ to 260 μJ is observed for the conversion efficiency from Fe K_α source. This result indicates that the conversion efficiency for iron is starting to reach its maximum values as an optimum intensity is reached. However this optimum intensity is still higher than the few times 10^{16} W/cm^2 employed here.

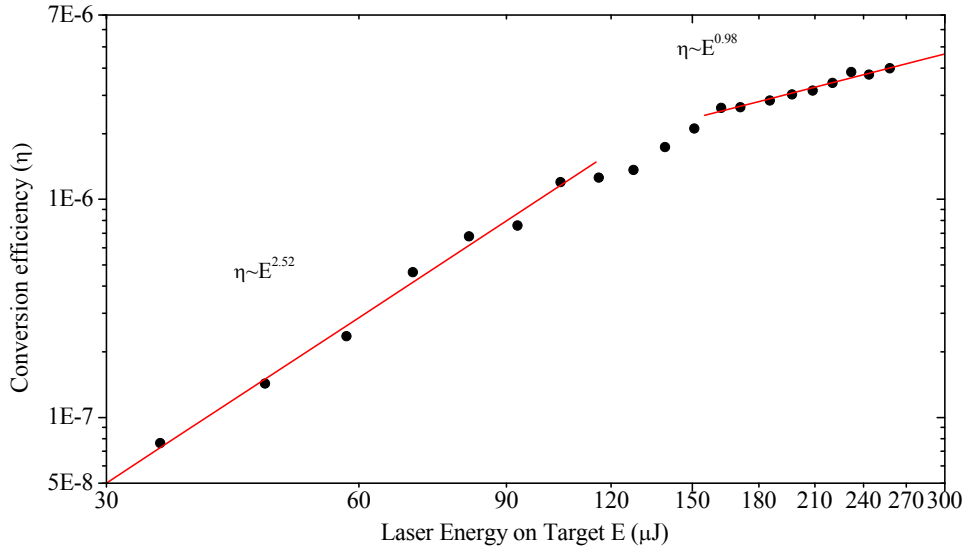

Figure 4.9 Scaling of Fe K_α conversion efficiency as a function of incident laser energy.

The Cu K_α X-ray spectra recorded using CdTe detector for the runs taken with the same poor quality laser conditions to compare with the lower conversion efficiency results obtained for Fe K_α. The scaling of Cu K_α is plotted as a function of laser pulse energy as shown in Figure 4.10. In the Cu K_α line, about 5.7×10^{8} photons/second were generated at a laser pulse energy of 253 μJ corresponding to a K_α conversion efficiency of 2.9×10^{-6} into 2π srad. The results of Cu K_α provide evidence that Fe K_α source could potentially improved up to experimentally reported conversion efficiency 4×10^{-5} (10^{7} photon/sr [25]) in the Fe K_α line using better laser mode and focal spot conditions.

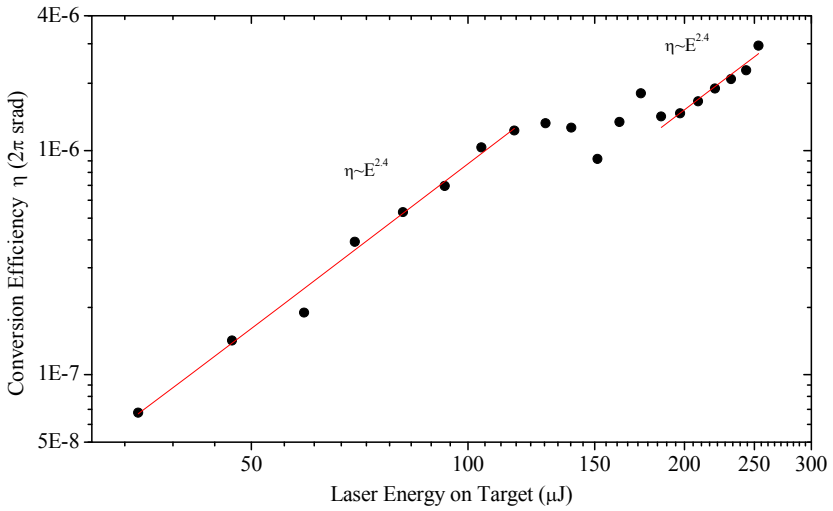

Figure 4.10 Scaling of Cu K_α conversion efficiency as a function of incident laser energy as measured with the CdTe detector to compare it with Fe K_α conversion efficiency numbers under similar laser conditions.

4.3 Silver K_α Source

A spectrum from the silver (Ag) laser-plasma X-ray source was recorded for a counting time of 30 seconds using the CdTe Amptek detector showing the K_α and K_β lines at 22.2 keV and 24.95 keV respectively. At 1 kHz repetition rate and laser pulse energy of 255 μJ on target a maximum Ag K_α yield of 1.4×10^{7} photons/s into 2π steradian was measured which corresponds to an energy conversion efficiency of about 2×10^{-7}.

The spectrum (Fig. 4.11) of laser produced plasmas Ag X-rays consists of continuum along with characteristic emission lines and data from this spectrum has been used to obtain the hot electron temperature.

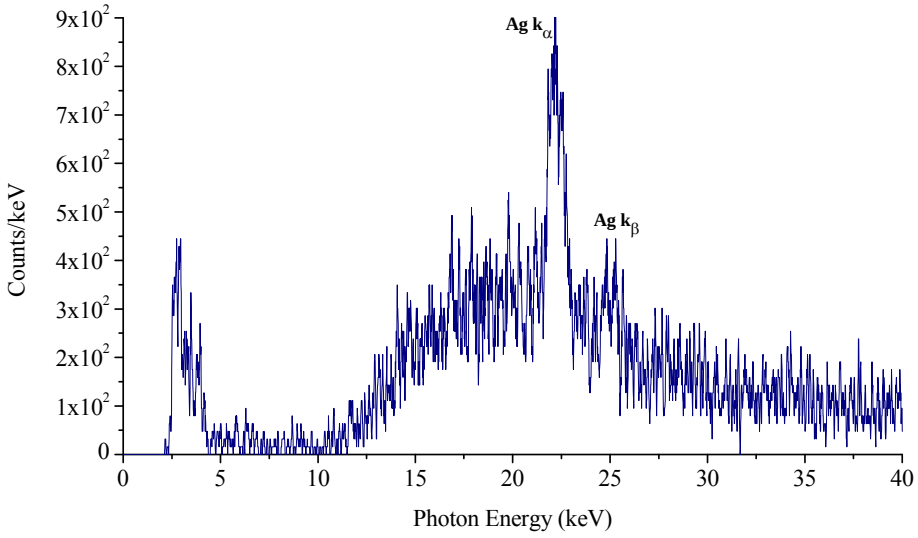

Figure 4.11 Raw X-ray spectrum obtained from an Ag target using the CdTe Amptek detector at a laser energy of E=255 μJ for a 30 second exposure at 1 kHz.

The effective electron temperature of $T_h \sim 7.1\pm 0.1$ keV is extracted assuming Maxwellian electron energy distribution function fitted over experimentally measured bremsstrahlung spectrum from 10 to 35 keV as shown in Figure 4.12. The detector was covered with 381 μm Al and 25 μm Fe filters for this measurement. Figure 4.13 shows the dependence of Ag K_α conversion efficiency on incident laser pulse energy. The Ag K_α conversion increases very rapidly with the incident laser pulse energy as expected when near the threshold for K_α excitation. A maximum conversion efficiency of 2×10^{-7} is observed by focusing the laser pulse energy of 255 μJ on target. We observed emission of Ag K_α peak down to a laser pulse energy of 116 μJ on target with a flux of 5.2×10^5 photon/s into 2π srad which corresponds to a conversion efficiency of 1.6×10^{-8} into 2π srad.

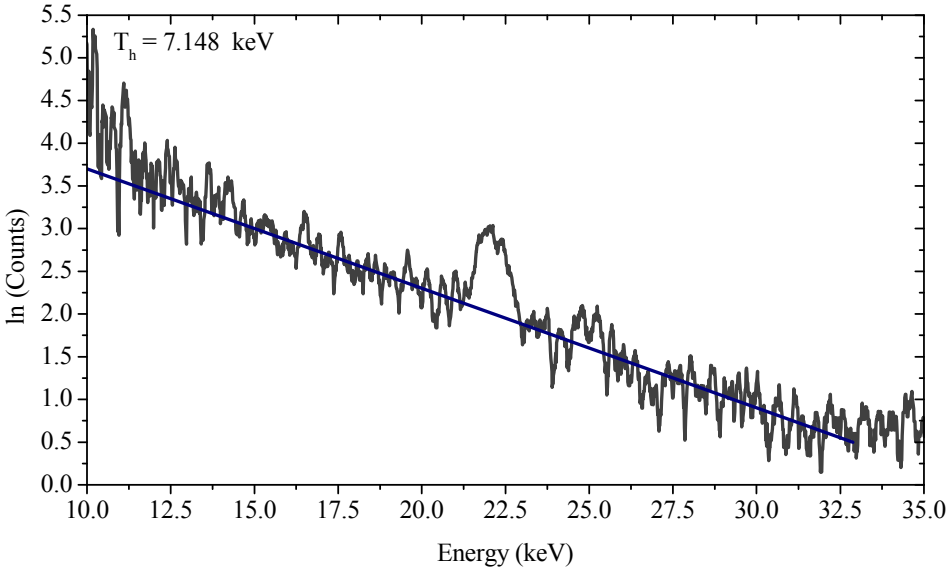

Figure 4.12 High energy tail signal (corrected for filter factors) taken during the Ag measurements has been fitted by a Maxwellian distribution from photon energies 10 to 35 keV with a characteristic temperature of $T_h \sim 7.1 \pm 0.1$ keV.

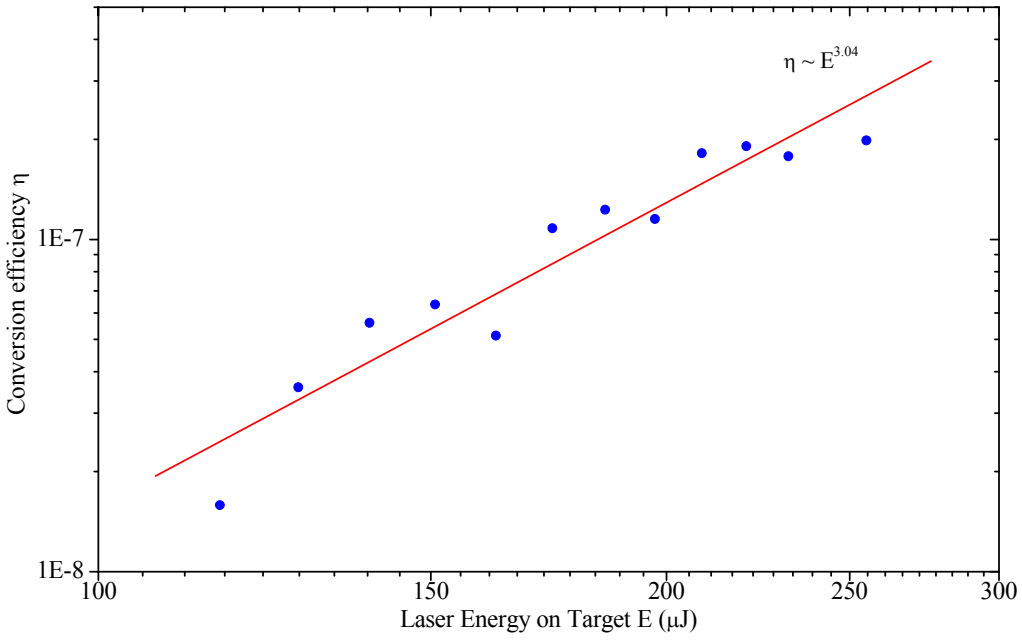

Figure 4.13 Scaling of Ag K_α conversion efficiency as a function of incident laser energy as measured with the CdTe detector.

4.4 Scaling of Cu K_α with laser energy

The measurements of the Cu K_α X-ray source emission have been performed more systematically employing all three detectors simultaneously to improve the accuracy of the results for photon flux and conversion efficiency as a function of incident laser energy. The laser energy was varied using a half-wave plate/polarizer attenuator. The pulses were focused on the Cu wire target using a 10x microscope objective (Newport) to obtain an intensity of a few times 10^{16} W/cm^2. The laser position and focus was fixed to maintain the same experimental condition for this run of experiments. Three detectors, the pin-diode, CdTe Amptek and CCD, were employed for the measurements. First the X-ray signal was optimized with the pin-diode detector which was a reference detector in this experiment for X-ray flux measurements. The pin-diode and CCD are at the same distance from the source as reported in chapter 3, but the distance of the CdTe detector was approximately 36 cm from the source. The CdTe Amptek detector was covered with different size pinholes and a 15 μm Ni filter at different laser pulse energies to avoid pile up events and cut the photon energy spectrum above the Ni K-edge at 8.33 keV. In Figure 4.14 the measured Cu K_α yield is plotted as a function of incident laser energy using three detectors at the same time. The X-ray flux scales smoothly with laser pulse energy up to 100 μJ beyond which we observed a steep increase in K_α X-ray yield from 100 μJ up to 130 μJ and then K_α photon flux grows continuously up to a maximum energy of ~290 μJ on target. The resultant conversion efficiency calculated from K_α counts is plotted as a

function of laser energy on target as shown in Figure 4.15. The result obtained from different detectors should match each other but all detector work on slightly different principles and charge collection procedures. The pin-diode has a larger spectral window (6.5 to 8.3 keV) than K_α line so contributions from high energy bremsstrahlung along with low energy X-ray photons are measured as part of the signal.

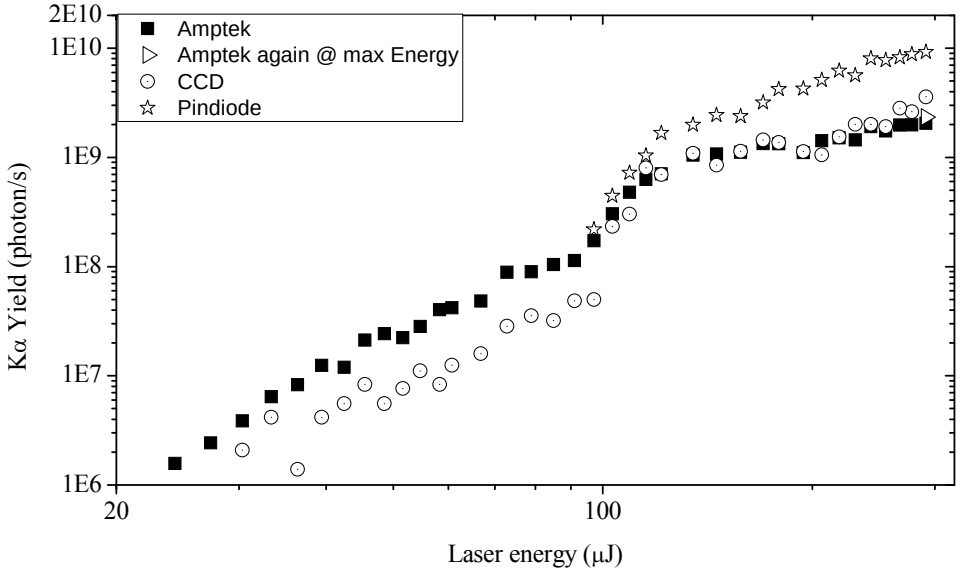

Figure 4.14 Raw Cu K_α flux into 2π srad as a function of laser energy energy before final correction factors and analysis were performed.

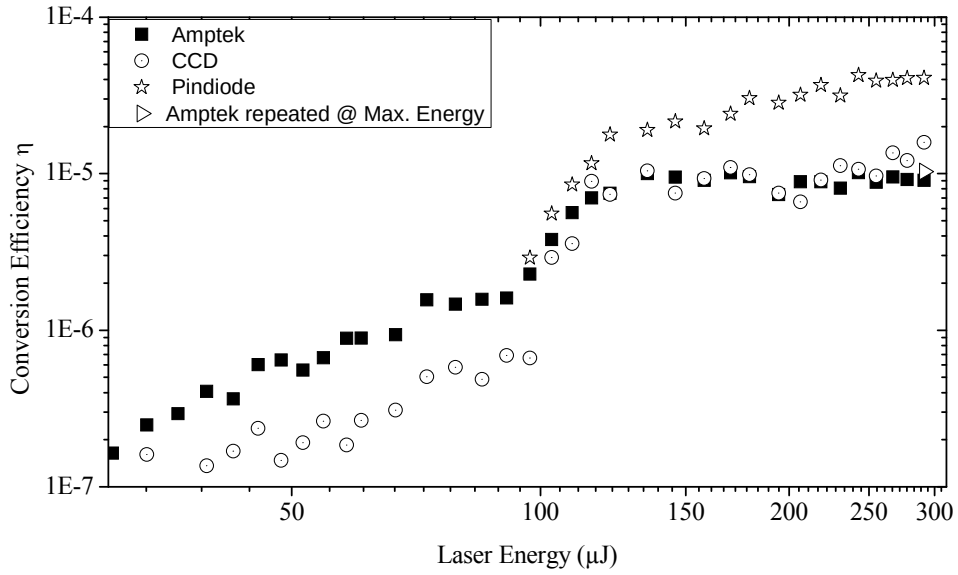

Figure 4.15 Raw Cu K_α conversion efficiency into 2π srad as a function of incident laser energy before final correction factors and analysis were performed.

To remove this unwanted photon flux we subtracted the contribution of X-ray photons (other than K_α) from pin-diode signal by using the measured spectra obtained from CdTe Amptek detector in the 1 to 100 keV range. In order to do this the measured CdTe Amptek spectrum was first corrected to give the real source spectrum and this was used to calculate the contribution to the pindiode spectrum taking into account all attenuation factors and response function. The spectrum window obtained from CdTe Amptek detector was used to correct the background in the measured emission from the pin diode detectors. Figure 4.16 shows the resultant measured K_α fraction (K_α line / Total X-rays spectrum) as a function of incident laser pulse energy. The analysis of K_α fraction to obtain the Cu K_α contribution includes the 15 μm Ni, 9 μm Al and 0.276 C/J sensitivity for a

pin-diode detector. It was found that the contribution of K_α decreases as compared to continuum with increasing laser energy. The fraction values obtained at different laser energies were multiplied with the photon flux from the pin-diode to obtain the corrected absolute K_α photon flux contribution.

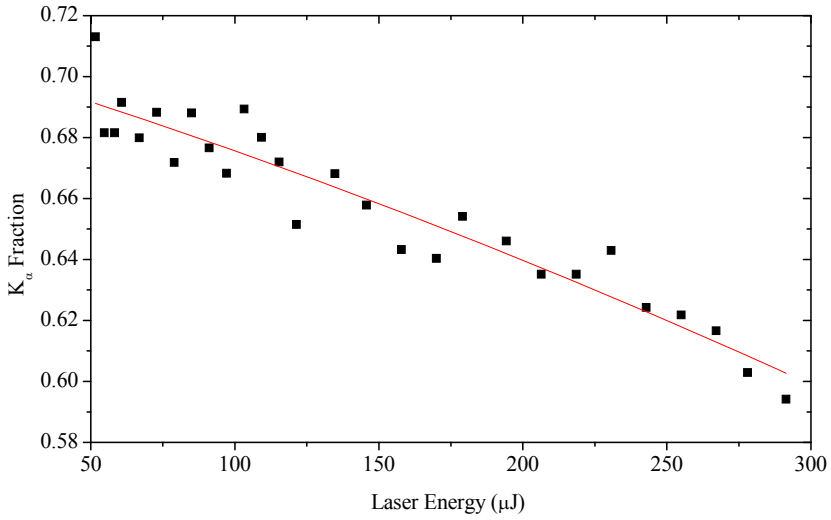

Figure 4.16 Calculated fraction of K_α flux signal as a function of laser energy for the pin-diode detectror based on the measured spectrum measured with the Amptek CdTe.

Secondly the CCD detector was operating as a single X-ray photon hit detector which gives a spectrum proportional to incident individual photon energy. In our experiment while operating at 1 kHz it is difficult to avoid pile-up problems. The raw CCD signal was not corrected for overlap of photons or K_α photons where energy was split between two pixels. This results in an underestimation of absolute number of K_α photons. To extract an absolute K_α photons flux a statistical analysis of exposed images has been performed which gives an average fraction of clean single pixels to multiple pixel deposition events

[single pixel hit / (single pixel hit + split pixels)] of 0.473. The absolute contribution of K_α photons can be obtained by dividing the measured photon flux and conversion efficiency by this fraction number. To improve this analysis further one has to carry out calibrations with known radioactive sources to measure these correction factors. Figure 4.17 and 4.18 shows K_α yield and conversion efficiency as a function of incident laser energy with the correction factors applied for the CCD and pin-diode data. The K_α yield for the pin-diode and CCD detectors match but the CdTe Amptek detector gives lower K_α photon flux at higher energies. It appears that above 150 μJ of laser energy the CdTe Amptek detector suffers an additional saturation effect. This may be due to pulse pileup or a difficulty in the PC data acquisition system in keeping up with the high count rates. This will be explored in future work. The X-ray flux obtained from pin-diode, CCD and Amptek (repeated) at maximum pulse energy 290 μJ are $5.5\pm1\times10^{9}$, $7.6\pm1.5\times10^{9}$ and $2.05\pm0.4\times10^{9}$ ($2.34\pm0.5\times10^{9}$) which corresponds to a conversion efficiency of $2.5\pm0.5\times10^{-5}$, $3.4\pm0.7\times10^{-5}$ and $9.1\pm2\times10^{-6}$ ($1.0\pm0.2\times10^{-5}$) into 2π srad respectively. From the corrected pin-diode and CCD camera measurements a final average conversion efficiency of 3.0×10^{-5} is obtained for a laser pulse energy of 290 μJ.

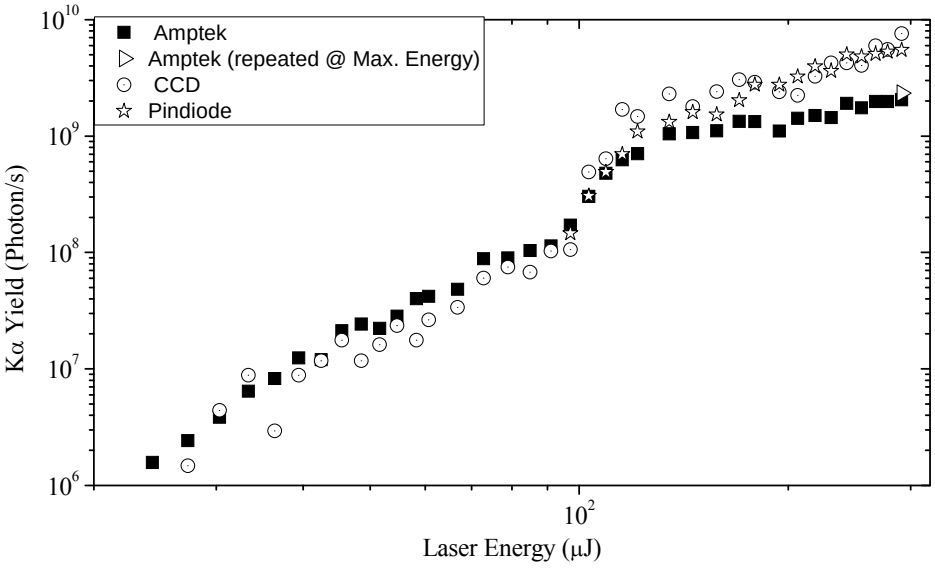

Figure 4.17 Measured Cu K_α flux into 2π srad after all detector corrections as a function of laser energy for the CdTe Amptek, Pin-diode, and CCD detectors.

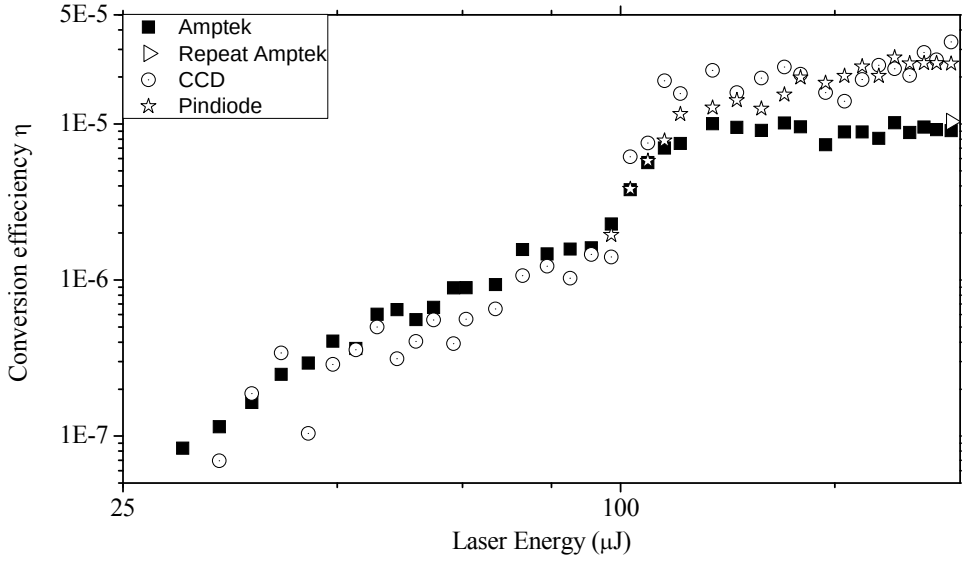

Figure 4.18 Cu K_α conversion efficiency into 2π srad after all detector corrections as a function of incident laser energy using the CdTe Amptek, Pin-diode, and CCD detectors.

4.5 Discussion

The X-ray conversion efficiency using sub-millijoule laser pulses focused on wire targets are in agreement with previously published results of bulk targets [24]. These are comparable to our earlier reported conversion efficiencies of 3.2×10^{-5} [24] and ~ 4×10^{-5} [17] based on Ross pair and filtered pin diode measurement respectively, Which are still the highest K_α yields measured from high repetition rate (1 kHz) sub-millijoule laser pulses. A summary of experiments performed by other groups and their published results along with conversion efficiency numbers are presented in detail in chapter 2. In an experiment by Hagedorn et al. [21] conversion efficiencies of 2.6×10^{-9} and 1.5×10^{-8} were reported from Cu K_α source into a half space by focusing 30 fs, sub-millijoule laser pulses at intensities of 2×10^{14} and 4×10^{15} W/cm^2 with pulse energies of 100 and 900 μJ respectively. The present results presented in this dissertation are 3 to 4 four orders of magnitude higher than those reported by Hagedron at 100 μJ. Similarly they reported a lower conversion efficiency for Fe of 2.1×10^{-9} using about 100 times lower laser intensity as compared to our experiment. It is expected that the optimum intensity range for highest conversion efficiencies is in the range of 10^{16} to 10^{18} W/cm^2, as calculated by Reich [84]. The results of Hagedon et al. [21] and current results are consistent with this conclusion indicating a very strong scaling with intensity up to the range of optimum intensities. A reported increase of Fe K_α yield is observed by applying

prepulse and multipule exposure conditions using 400 μJ, 25 fs laser pulses focused on tape targets up to an intensity of ~ 10^{15} W/cm^2 with a conversion efficiency of 2.56×10^{-6} [22]. In the sub-millijoule laser pulse regime our higher conversion efficiency results are due to optimized focusing to smaller of laser spots (~ 4 μm diameter) which raises the intensity of laser by an order of magnitude higher than the reference [21, 22] where they have roughly 25 μm and 40 μm spot sizes respectively.

The effect of prepulse is quite important since even a small preformed plasma can increase both the absorption and hot electron energy. In the present case we expect that the prepulse will form a small preplasma staring at ~ 100 μJ main pulse energy where the 4.6×10^{-4} prepulse energy leads to ~ 4×10^{12} W/cm^2 intensity on the target surface. This preplasma formation may explain the step increase in X-ray yield shown in plots 4.16 and 4.17 above 100 μJ laser energy. The dependence of X-ray conversion efficiency on pulse duration has been reported using 10 Hz laser systems. Chen et al. [26] using millijoule laser pulses observed a decrease in K_α efficiency with shorter pulse duration at constant laser intensity but the K_α efficiency was roughly constant when varying the pulse duration with a fixed laser fluence. The experiment of Hou et al. [68] indicates a reduction of K_α photons with respect to continuum as pulse duration is increased. They empirically scaled X-ray conversion efficiency and hot electron temperature (T_h) proportional to $\exp(-\tau/\beta)$, where β is slightly different for total X-rays,

K_α and T_h. Retting et al. [66] focused 1.8 mJ laser pulses up to a peak intensity of 4×10^{16} to produce K_α and broadband spectrum of different elements. They obtained Cu and Fe K_α conversion efficiencies of 4.6×10^{-6} and 8.6×10^{-6} respectively along with a power-law scaling exponent of 1.75 for Cu X-ray source which is in agreement with our current results [17] and some other experiments [21, 26, 68, 70]. There is a discrepancy in X-ray yield results of reference [22] and [66] where [22] found an increase in X-ray flux with the overlap of laser spot on target but [66] reported a reduced X-ray yield with multiple exposures on target. A conversion efficiency of 1.0×10^{-5} was reported by Zhavoronkov et al. [70] using millijoule laser pulses of intensity ~ 10^{17} W/cm^2 with no saturation of Cu X-ray yield [72]. The results presented in this dissertation also appear to be limited by maximum pulse energy and not by saturation in our intensity range as shown in Figure 4.1. The distance between the exact best focus point and the target surface is also a critical parameter of interest for the optimization of X-ray yield, but there are striking differences in experimental results where Silies et al. [87], Lu et al. [89] and Khattak et al. [92] showed optimum X-ray yield around best focus and Eder et al. [77] reported both theoretical and experimentally that highest K_α photons can be obtained by placing the focusing optics a few micron away from the location of best focus. This discrepancy could be explained by the high levels of preplasma in the experiment of Eder et al. [77] resulting in an expansion of the target surface and formation of an extended expansion plasma. In comparison to above mentioned results Zamponi et al. [72] reported

experimentally a constant X-ray yield over a distance larger than the Rayleigh length for the case of 5 mJ, 35 fs pulses focused up to intensities of 10^{18} W/cm^2 using a 75 mm focal length parabolic mirror. The experimental work of Lu et al. [89] also shows different optimum focusing conditions for different target (Z) material. The X-ray scaling with laser intensity or pulse energy shows s steady increase within the range of $\sim 10^{16} - 10^{18}$ W/cm^2 as shown in experiments [72, 89] but Silies et al. [87] showed a steady increase of X-ray flux up to pulse energies of 3 mJ (~ 9×10^{16} W/cm^2) and then found a decrease in X-ray yield with higher laser intensity. A reduction and saturation of K_α X-ray flux has been reported by number of groups [26, 68, 77, 86] above laser intensity of few times 10^{18} W/cm^2. These experimental investigations of K_α yield show a similar trend as that predicted by Reich et al. [84] but with optimum intensity for peak conversion to X-rays almost 10 times higher than predicted by Riech, $I_{opt} = 7\times10^9 \cdot Z^{4.4}$ [84]. This discrepancy could be due to simple assumptions made by Reich in his scaling model which did not include ionization and plasma heat conduction effects. According to this calculation the optimal intensities for Fe (26) K_α (6.40 keV), Cu (29) K_α (8.05 keV) and Ag (47) K_α (22.2 keV) are 1.2×10^{16}, 2×10^{16} and 1.6×10^{17} W/cm^2 respectively. Our results at a peak intensity of 3×10^{16} W/cm^2 indicate that the conversion efficiency for Fe is starting to saturate while those for Cu and Ag are still climbing. Thus, it would appear that the optimum intensities are higher than those predicted by Reich et al. [84]. This may not be unexpected

given the many simplifying assumptions in the model of Reich et al. [84]. Some reported experiments [23, 87] have been performed with higher repetition laser systems than used in our experiments. Using 2-kHz millijoule laser pulses with an intensity of ~ 10^{17} W/cm^2 Jiang et al. [23] obtained a conversion efficiency ~ 10^{-8} which is significantly lower than our result at 1 kHz with a sub-millijoule laser and other high repetition rate experiments [22, 66, 70, 72, 87, 88]. Silies et al. [87] used a multi-kilohertz (1-10 kHz) laser with a large focal spot to compare to 1 kHz experiments to measure the X-ray flux as a function of repetition rate. They found an increase of K_α yield by increasing the repetition rate up to a certain point and then it started to saturate around 8 kHz up to 10 kHz for Fe, Al and a decrease of K_α yield in the case of Cr targets.

The experimental results presented in Table 2.2 of laser plasmas X-ray conversion efficiencies are plotted as a function of laser intensity Fig. 4.19. The highest conversion of laser pulse energy into X-rays have been reported by Eder et al. [77], Chen et al. [65] and Khattak et al. [92] using millijoule laser pulses focused on Cu target. Chen et al. [65] used 100 mJ laser pulses to focus up to an intensity of about 1×10^{18} W/cm^2 to obtain a conversion efficiency of 4×10^{-4}. A conversion efficiency of 2.75×10^{-4} is obtained at a much higher pulse energy of ~ 300 mJ focused up to a higher intensity of ~10^{19} W/cm^2 by Khattak et al. [92]. With 200 mJ laser pulses and an order of magnitude lower intensity of ~10^{17} W/cm^2 Eder et al. [77] reported a conversion efficiency of 1×10^{-4}. These reported results together with our results fit a trend line given by the dotted curve in Figure

4.19 which indicates a peak conversion efficiency of ~ 4×10^{-4} at an intensity of ~ 10^{18} W/cm^2. The peak conversion efficiency for Cu K_α of 4×10^{-4} observed by Chen et al. [65] is close to that of 5.6×10^{-4} predicted by Reich et al. [84]. However, this was obtained at a much higher intensity of 1×10^{18} W/cm^2 compared to 2×10^{16} W/cm^2 predicted by Reich. A higher K_α conversion efficiency of 1.2×10^{-3} (0.5×10^{12} photon/shot/2π) was obtained using a Ti target for X-ray generation with laser pulses of ~300mJ at a laser intensity of 3×10^{17} W/cm^2 and 2×10^{19} W/cm^2 by Ewald et al. [86]. They observed an increase of X-ray flux up to maximum 10^{12} photon per pulse at an intensity 3×10^{17} W/cm^2 with an electron temperature of 60 keV and then X-ray yield start to decrease with minimum around 2×10^{18} W/cm^2 at an electron temperature 900 keV. Above 2×10^{18} W/cm^2 they found a growth in X-ray yield up to an intensity of 2×10^{19} W/cm^2 with a maximum 10^{12} photon per pulse due to the contribution of relativistic electron at much higher electron temperature. This complex scaling behavior is due to change in absorption mechanisms from non-relativistic to relativistic regimes which gives increasing absorption above few times 10^{18}W/cm^2 and the increasing cross-section for generation of K_α X-rays from electrons above 900 keV. A hot electron temperature of 8-12 keV were expected by Gibbon and Forster [4] and Forslund et al. [63] for an irradiance of about $10^{16} W \cdot cm^{-2} \cdot \mu m^2$ which is in agreement with our results. Rousse et al. [25] reported a Fe K_α yield of about 10^7 photon/sr which corresponds to a conversion efficiency of 4×10^{-5} in 2π srad using 1.5 mJ, 100 fs laser pulses focused to intensities of 3×10^{16} W/cm^2 along with

amplified spontaneous emission (ASE) pedestal effects on X-ray yield. The Fe K_α results reported by Rousse et al. [25] are comparable with our Cu K_α conversion efficiency results, but our Fe K_α source needs to be optimized further with optimum laser parameters. Chen et al. [26] observed a scaling of Ag K_α conversion efficiency as function of laser intensity with an exponent of ~ 2.2 below 10^{18} W/cm^2. A maximum Ag K_α conversion efficiency of 2×10^{-5} was obtained in 2 π sr using ~ 240 mJ, 70 fs laser pulses with a focal spot diameter of 10 μm (FWHM). The saturation of K_α conversion efficiency is observed above a laser intensity of 10^{18} W/cm^2, which is not consistent with the theoretical model calculations of Ag reported by Reich et al. [84]. This discrepancy in result can be due to simple assumption made by Reich in their model calculation or different absorption mechanisms depending on the scale length of plasma as explained by Chen et al. [26]. An Ag K_α conversion efficiency of 9×10^{-6} into 2π srad were reported by Toth et al. [19] using high contrast 400 nm laser pulses to minimize the plasma expansion due to prepulse effects. A lower conversion efficiency by a factor of 2 times is observed with no saturation of Ag K_α line efficiency around 10^{18} W/cm^2 as compared to the result presented by Chen et al. [26] at 800 nm laser pulses. This decrease in K_α conversion efficiency can be due to lower K-shell ionization cross-section for hot electrons at a relatively lower electron temperature of 16 keV [19] as compared to 25 keV [26] at 10^{18} W/cm^2. The experimental reported results by different groups along with University of Alberta

K_α experimental results and theoretical predicted curves of Reich et al. [84] are plotted as a function of laser intensity in Fig. 4.19.

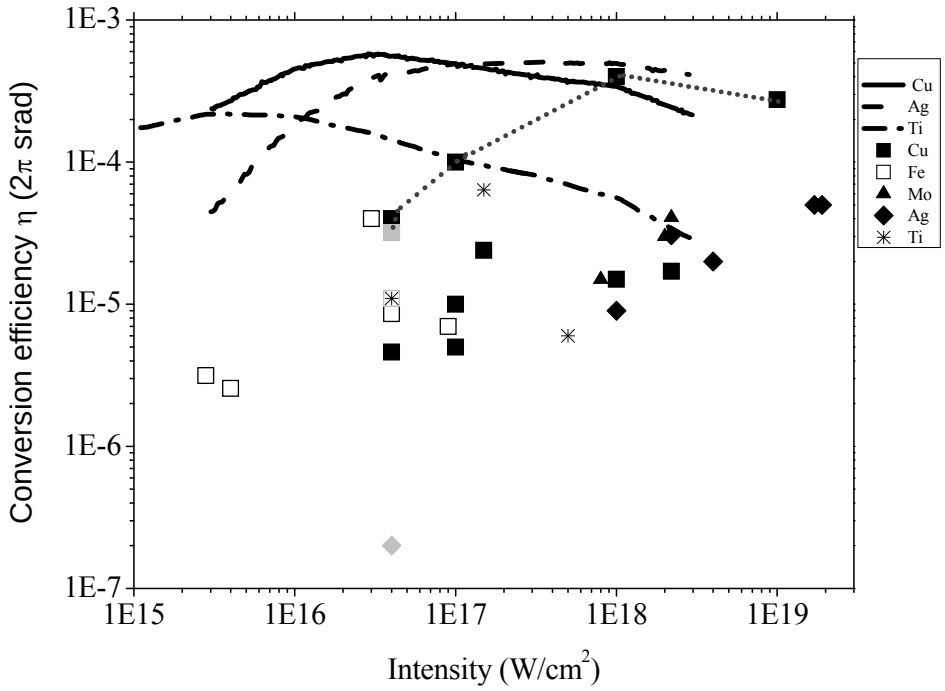

Figure 4.19 Experimental results (black) of conversion efficiency given in table 2.2 are plotted as a function of laser intensity, together with results measured by the University of Alberta (gray) and the scaling results predicted by Reich et al. [84].

4.6 Application of laser plasmas X-rays sources

The Laser produced Cu and Fe K_α X-ray sources have been applied to applications in phase contrast imaging due to their high degree of spatial and spectral coherence used to record the images of a number of test samples. The in-line phase contrast imaging geometry has been used in the present experiment to record both absorption and phase information, which make it possible to observe

boundaries of different structures within objects due to diffraction or edge effects. The laser based X-ray sources have been applied to imaging of low atomic number objects [17, 18, 19] and thin biological samples [17, 18, 98] with a large object to detector distance to provide an enhancement in the image due to phase contrast effect as compared to images recorded with the object much closer to the detector.

The phase contrast images were recorded using high repetition rate 1 kHz, 120 fs laser based Cu and Fe X-ray sources. Due to operation at 1 kHz this source has the capability to produce images in a short duration of recording time with a photon fluence of few times 10^7 photons/cm^2 at the detector. Images are recorded at two different magnifications viz. 4.32 and 10.4. For the first case, the object was at a distance of 31 cm and for the latter it was at 13 cm from the source. The corresponding object to detector distances were 103 and 121 cm respectively. Well-defined samples like optical glass fibers and plastic strips were imaged to characterize the imaging process. Fig. 4.20(a) shows the phase contrast image of a glass fiber with plastic cladding of a total diameter of 200 μm recorded at the higher magnification of 10.4 times. The object was kept inside the vacuum chamber at a distance of 13 cm from the source. The diameter of the fiber without the plastic jacket was 125 μm. The image was recorded in an exposure of 5 minutes. This corresponds to an x-ray flux of ~ 2.7x10^7 ph/cm^2 on the CCD detector after all attenuation factors are taken into account. In this case 15 μm Ni filter, 125 μm Mylar and 74 cm of air path were used. The corresponding line

profile across the fiber is shown in Fig. 4.20(b). Contrast enhancement at the interfaces of the glass fiber and plastic jacket, and of the plastic jacket and air is clearly seen in the profiles.

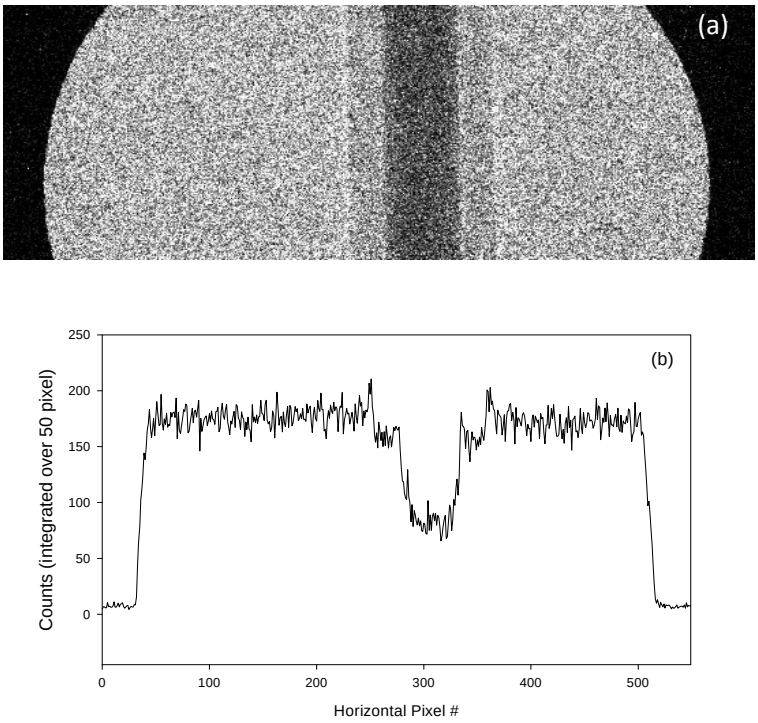

Figure 4.20 (a) Phase contrast image of a 200 μm diameter plastic coated glass fiber recorded at high magnification of 10.4 times using the Cu K_α source. (b) line out across the image integrating 50 pixels vertically.

Similarly, Fig. 4.21(a) shows the images of glass fibers mounted in a cross geometry, recorded at low magnification of 4.32 times. The left vertical fiber does not have a plastic jacket on it. In this case the sample was kept outside the plasma vacuum chamber (Fig. 3.3). The intensity profile (Fig. 4.21(b)) is for the vertical fiber with plastic cladding indicating the refraction and edge diffraction of X-rays at the boundaries of fiber. The horizontal and vertical fibers have similar profiles

and fringe intensity modulation thus confirming the equal coherence of the source in both the vertical as well as the horizontal directions.

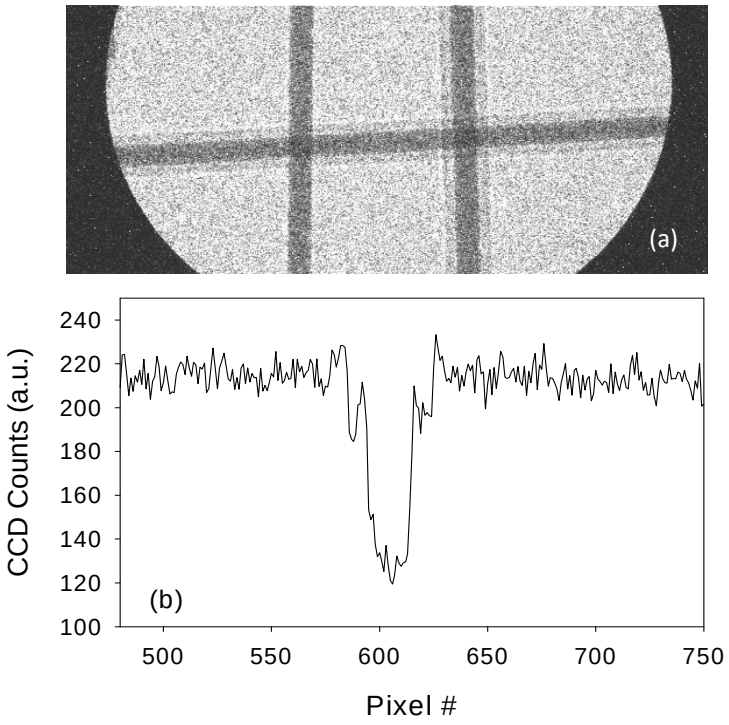

Figure 4.21 (a) Phase contrast images of plastic coated glass fibers and an uncoated glass fiber using the Cu Kα source in a crossed geometry recorded at low magnification of 4.32 times. (b) Line out across the right fiber.

The glass fibers with cross geometry were also exposed to the Fe X-ray source for an exposure of 300 seconds at the low magnification distance. Figure 4.22 shows the image of fibers with and without plastic cladding along with a leg of an insect on the top left side under the fiber without plastic jacket. Filtering of 25 μm along with 125 μm mylar and 74 cm air path were used in this case. The effect of in-line phase shift edge enhancement is clearly visible in the image and line profiles of the horizontal and vertical fibers. An X-ray photon fluence of 1.0×10^7

ph/cm^2 was observed on CCD detector. The small, ~ 80 μm diameter insect leg also visible in the Figure 4.22 gives a striking example of the edge enhancement effect making an otherwise transparent object very visible.

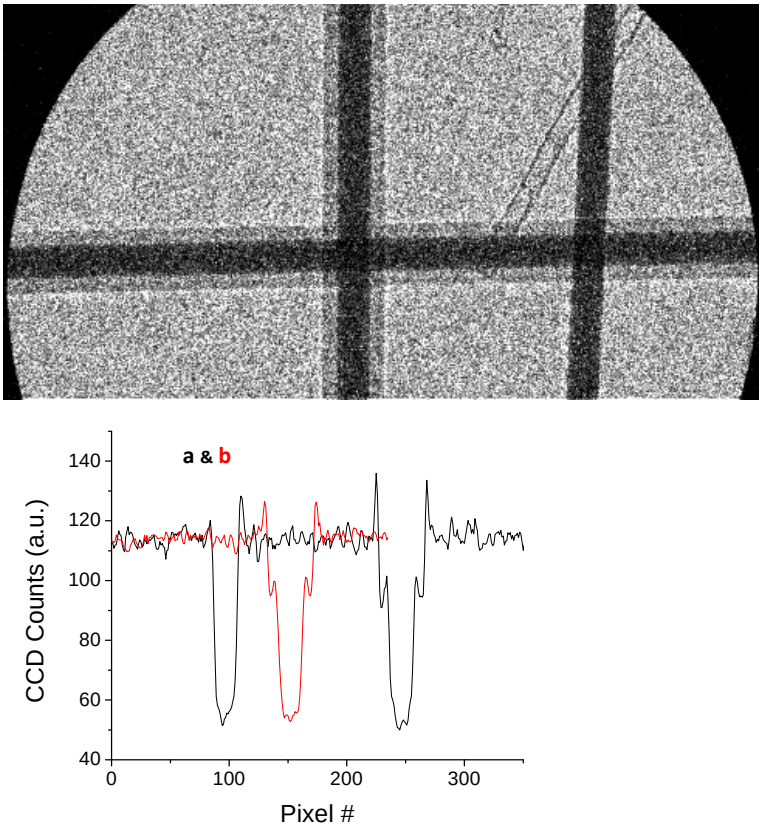

Figure 4.22 Phase Contrast Image of Glass Fibers with and without plastic jacket using the Fe X-ray Source. a) Intensity line out across the vertical fiber. b) Intensity line out across the horizontal fiber.

Mylar foils of two different thickness 50 μm on left side and 25 μm on right side with a air gap in between the two films were used as an object and exposed for 15 minutes using Cu K_α X-rays with 4.32 times magnification as shown in Fig. 4.23 (a). The measured X-ray photon flux on CCD for this image is about ~ 5x10^7 ph/cm^2. The intensity modulation due to the film edges is clearly seen in the

lineouts of the image (Fig. 4.23(b)), which would otherwise not be easily seen in the absorption image due to low absorption (4% and 8%) of the films for the keV X-rays. From the FWHM of the positive fringe peaks (12 μm) equivalent. The intensity profile across the fringes at the Mylar foil edges is in reasonable agreement with the previously measured source size of 8 μm (FWHM) [24].

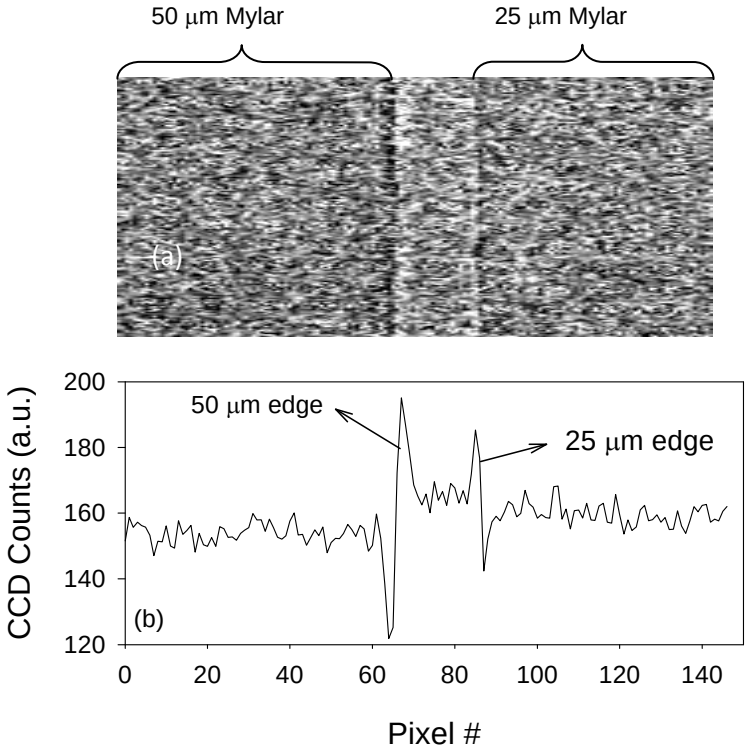

Figure 4.23 Phase contrast images of Mylar foils recorded for an exposure of 15 minutes using Cu K_α X-rays at the low magnification position.

Next, the phase contrast image of a microscopic biological specimen, namely a mosquito was recorded. The mosquito was kept at the exit window of the plasma chamber (Fig.3.3) thus providing convenience in operation. At the same time one could image the biological samples in vivo condition if they remain fixed in space. Fig. 4.24 shows the image of the Mosquito recorded with an

exposure of 15 minutes. The corresponding x-ray photon flux was ~ $8.0x10^7$ ph/cm^2. The fine details of the internal structure of the mosquito are clearly visible in the phase contrast image. The CCD counts in the images recorded for various objects are in good agreement with the x-ray flux estimated from the pin-diode signals thus confirming the high x-ray flux of the source.

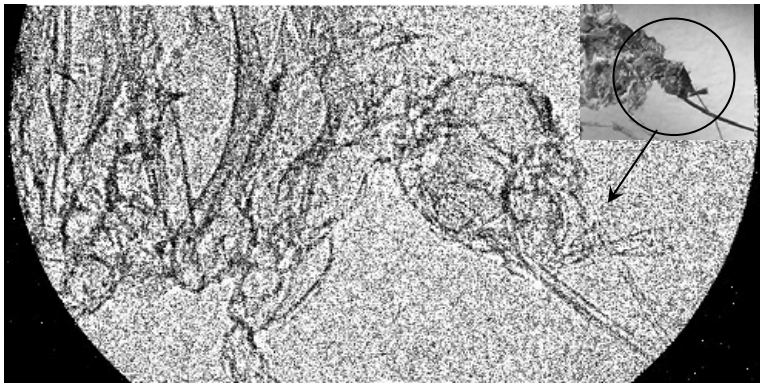

Figure 4.24 Phase Contrast Image of a Mosquito recorded for an exposure of 15 minutes using the Cu X-ray Source. The inset shows an optical image of the mosquito. The full area shown in the X-ray image is 2.91 by 1.54mm.

The Phase contrast image of Mosquito was also recoded for an exposure of 600 seconds using the Fe source giving a photon flux of $1.70x10^7$ ph/cm^2 on the CCD detector as shown in Fig. 4.25. The image shown in Fig. 4.25 provides details of the fine structures of the Mosquito, Similar to the Cu K_α image which are difficult to achieve with conventional X-ray radiography. The Fe X-ray flux on the CCD is 4 times lower than used for the Mosquito image exposed by Cu K_α source. The Mosquito image taken using Fe X-ray source is a little fainter as compared to Figure 4.24 taken with the Cu K_α source due to exposure to a broadband background X-ray flux. Appropriate filters are required for future

exposures in front of detector to block the broadband continuum emission from laser produced Fe X-ray source and use only high intensity, coherent K_α line for phase contrast imaging.

Figure 4.25 Phase Contrast Image of Mosquito recorded for an exposure of 10 minutes using the Fe X-ray Source under similar conditions to Figure 4.24.

Laser based K_α sources [17, 18, 19, 98] and synchrotron sources [99] have been applied successfully in the past for application in phase contrast imaging. Experimental investigation of in-line phase contrast imaging has been reported with variations in object to detector distances by Toth et al. [18] using 240 mJ, 60 fs laser based Mo K_α source. The results of this study [18] demonstrated a significant edge enhancement for a larger object to detector distance as compared to object placed close to detector with a K_α photon flux ranges from $5x10^7$ to $5x10^8$ ph/cm^2 on detector. Toth et al. [19] demonstrated a qualitative agreement between experimental and theoretical model calculation of in-line phase contrast imaging of test samples using Mo K_α and La K_α sources. They observed an increase of enhancement in edge contrast with the large distance between object to

detector and a decrease in phase contrast with the increase of X-ray energy from Mo K_α (17.5 keV) to La K_α (33.4) both theoretically and experimentally. Chen et al. [98] used 2 TW, 70 fs laser based Ar K_α (2.96 keV) source with a flux of $5x10^6$ ph/cm^2 to record a phase contrast image of biological sample. The K_α flux on detector is 2 orders of magnitude lower than one used by Toth et al. [18, 19] and few times lower than used by Chakera et al. [17] to record the biological specimens.

Chapter 5 Conclusion and Future Work

The aim of this dissertation was to further develop and characterize compact, durable and qausi-continuous hard X-ray sources from a sub-millijoule femtosecond laser plasma. Laser pulses of < 300 μJ, 120 fs were focused with a 10x microscope objective onto Cu, Fe and Ag wire targets reaching a peak intensity of ~ 4×10^{16} W/cm^2 to generate hot electrons and X-rays. Previous work on the development of a Cu K_α source has been extended by carrying out a more definitive measurement of X-ray conversion efficiency using three detector systems, i.e. a pin-diode, a CdTe pulse height analysis system and a single hit CCD camera system. In particular the scaling of X-ray conversion efficiency for Fe and Ag K_α emission have been carried out. Finally, initial studies comparing phase contrast imaging using the Cu K_α and Fe K_α sources have been carried out.

Investigation of K_α line emission from three target materials Fe, Cu and Ag from 6.4 keV up to 22.2 keV photon energies have been measured together with broadband continuum using the CCD and CdTe Amptek detector. The laser operating at 1 kHz with a contrast ratio of 4-8×10^{-4} was focused onto a moving wire target to generate K_α radiation in the non-relativistic regime. The K_α yield driven at kilohertz repetition rate reached ~ 7×10^9 photon/s for Cu K_α, 3×10^9 photon/s for Fe K_α and 1.4×10^7 photon/s for Ag into 2π srad. The corresponding energy conversion efficiency were approximately 3×10^{-5}, 1.06×10^{-5} and 2×10^{-7}

respectively. A decrease in conversion efficiency of 3 times for Fe (stainless steel) K_α and over two orders of magnitude for the silver K_α line is observed relative to the copper emission. These relatively high K_α conversion efficiencies are be achieved by optimizing the focus, preplasma and target surface conditions when using sub-millijoule laser pulses. A power law scaling exponent of 1.87 is obtained for the conversion efficiency of Cu X-ray source as a function of laser pulse energy. The hot electron temperature of 8-9 keV obtained from Cu targets is in good agreement with the resonance absorption mechanism, but a lower hot electron temperature 7.1 keV extracted from Ag could be due to lower laser intensity for the Ag and Fe series of measurements which does not generate enough electrons with kinetic energies higher than K-shell ionization energy of silver. Further research is required in the future in order to study the scaling of the Fe and Ag K_α emission over a wider intensity range and to find the optimum intensity for K_α generation for Fe, Cu and Ag. Further improvements are required on the theoretical modeling starting from the original scaling laws developed by Reich et al. [84] but including more accurate models of laser pulse absorption, hot electron generation and K_α emission excitation in order to reconcile current differences between experimentally measured conversion efficiencies and those theoretically predicted. A more systematic study of edge enhancement form phase contrast imaging as a function of sample geometry, imaging distance and source wavelength should be carried out and compared to numerically calculated edge

diffraction features. Finally more precise measurements are required of the exact source size and X-ray pulse duration.

Such hard X-ray sources show considerable promise both to study the dynamics of the plasma formation process and for applications in ultra-fast probing. This compact, high repetition rate X-ray source has been applied to material and biological samples to obtain phase contrast enhanced images using the in-line geometry. The fine edge details of structures within an object down to the order of 10 μm are visible due to the high spatial resolution of the micron size laser produced X-ray source. Commercially available ultrafast lasers with repetition rates currently up to 10 kHz and perhaps higher in the future can potentially be used to generate K_α X-ray sources with even higher average flux which could be utilized to for clinical and other applications with low dose rate and shorter acquisition times. Such sources are promising alternatives to x-ray tube and synchrotron sources and are worthy of further study and optimization.

REFERENCES:

1. A. M. Lindenberg, I. Kang, S. L. Johnson, T. Missalla, P. A. Heimann, Z. Chang, J. Larsson, P. H. Bucksbaum, H. C. Kapteyn, H. A. Padmore, R. W. Lee, J. S. Wark, and R. W. Falcone, "Time-Resolved X-Ray Diffraction from Coherent Phonons during a Laser-Induced Phase Transition" Phys. Rev. Lett. 84, 111 - 114 (2000).

2 . Christoph Rose-Petruck, Ralph Jimenez, Ting Guo, Andrea Cavalleri, Craig W. Siders, Ferenc Rksi, Jeff A. Squier, Barry C. Walker, Kent R. Wilson and Christopher P. J. Barty, "Picosecond–milliångström lattice dynamics measured by ultrafast X-ray diffraction" Nature 398, 310-312 (1999).

3 . Christian Rischel, Antoine Rousse, Ingo Uschmann, Pierre-Antoine Albouy, Jean-Paul Geindre, Patrick Audebert, Jean-Claude Gauthier, Eckhart Fröster, Jean-Louis Martin and André Antonetti, "Femtosecond time-resolved X-ray diffraction from laser-heated organic films" Nature 390, 490-492 (1997)

4. P. Gibbon and E. Förster, "Short-pulse laser-plasma interactions" Plasma Phys. Control. Fusion 38, 769-793 (1996)

5. Klaus Sokolowski-Tinten and Dietrich von der Linde, "Ultrafast phase transitions and lattice dynamics probed using laser-produced x-ray pulses" J. Phys.: Condens. Matter 16, R1517–R1536 (2004).

6. J. Hares, J. D. Kilkenny, M. M. Key and J. G. Lunney, "Measurement of Fast-Electron Energy Spectra and Preheating in Laser-Irradiated Targets" Phys. Rev. Lett. 42, 1216 - 1219 (1979)

7. N. H. Burnett, G. D. Enright, A. Avery, A. Loen, and J. C. Kieffer, "Time-resolved K_α spectra in high-intensity laser-target interaction" Phys. Rev. A 29, 2294 - 2297 (1984)

8. E. M. Campbell, "The physics of megajoule, large-scale, and ultrafast short-scale laser plasmas" Phys. Fluids B 4, 3781-3799 (1992)

9 . Feng Gai, et al.," Chemical Dynamics in Proteins: The Photoisomerization of Retinal in Bacteriorhodopsin" Science 279, 1886 (1998)

10. J. Arthur, "Status of the LCLS x-ray FEL program (invited)" Review of Scientific Instruments, 73, 1393 (2002).

11. A. J. Nelson, S. Toleikis, H. Chapman, S. Bajt, J. Krzywinski, J. Chalupsky, L. Juha, J. Cihelka, V. Hajkova, L. Vysin, T. Burian, M. Kozlova, R.R. Fäustlin, B. Nagler, S. M. Vinko, T. Whitcher, T. Dzelzainis, O. Renner, K. Saksl, A. R. Khorsand, P.A. Heimann, R. Sobierajski, D. Klinger, M. Jurek, J. Pelka, B. Iwan, J. Andreasson, N. Timneanu, M. Fajardo, J.S. Wark, D. Riley, T. Tschentscher, J. Hajdu, and R.W. Lee, "Soft x-ray free electron laser microfocus for exploring matter under extreme conditions" Opt. Express 17, 18271 (2009)

12. D.P. Bernstein, Y. Acremann, A. Scherz, M. Burkhardt, J. Stöhr, M. Beye, W.F. Schlotter, T. Beeck, F. Sorgenfrei, A. Pietzsch, W. Wurth, and A. Föhlisch, "Near Edge X-ray Absorption Fine Structure Spectroscopy with X-Ray Free Electron Lasers" Appl. Phys. Lett. 95,134102 (2009)

13. Eric Hand, "X-ray free-electron lasers fire up" Nature 461, 708 (2009)

14. C. J. Gaeta, H. Rieger, I. C. E. Turcu, R. A. Forber, S. M. Campeau, K. L. Cassidy, M. F. Powers, A. Stone, J. R. Maldonado, S. Mrowka, G. French, J. Naungayan, C. Kelsy, P. Hark, J. H. Morris, R. M. Foster, J. C. Carosella, D. Fleming, R. Selzer, and H. Siegert, "High-power collimated laser-plasma source for proximity x-ray nanolithography" J. Vac. Sci. Technol. B 21, 280 (2003)

15. P. Forget, F. Dorchies, J.-C. Kieffer, and 0. Peyrusse, "Ultrafast broad band laser plasma X-ray source for femtosecond time-resolved. EXAFS" Chemical Physics, 299, 259 (2003)

16. P. A. C Takman, H. Stollberg, G. A. Johansson, A. Holmberg, M. Lindblom, H. M. Hertz, "High-resolution compact X-ray microscopy", Journal of Microscopy 226 (2), 175 (2007)

17. J. A. Chakera, A. Ali, Y. Y. Tsui, and R. Fedosejevs, "A continuous kilohertz Cu K_α source produced by submillijoule femtosecond laser pulses for phase contrast imaging" Applied Physics Letters 93, 261501 (2008)

18 . R. Toth, J. C. Kieffer, S. Fourmaux, T. Ozaki, A. Krol, "In-line phase-contrast imaging with a laser-based hard x-ray source" Review of Scientific Instruments 76, 083701 (2005)

19 . R. Toth, S. Fourmaux, T. Ozaki, M. Servol, J. C. Kieffer, R. E. Kincaid, Jr., A. Krol, "Evaluation of ultrafast laser-based hard X-ray sources for phase-contrast Imaging" Physics of Plasmas 14, 053506 (2007)

20. J. Thogersen, A. Borowiec, H. K. Haugen, F. E. McNeill and I. M. Stronach, "X-ray emission from femtosecond laser micromachining" Appl. Phys. A 73, 361 (2001).

21. M. Hagedorn, J. Kutzner, G. Tsilimis and H. Zacharias, "High-repetition-rate hard X-ray generation with sub-millijoule femtosecond laser pulses" Appl. Phys. B 77, 49 (2003).

22. J. Kutzner, M. Silies, T. Witting, G. Tsilimis, H. Zacharias, "Efficient high-repetition-rate fs-laser based X-ray source" Appl. Phys. B 78, 949 (2004).

23. Y. Jiang, T. Lee, W. Li, G. Ketwaroo, and C. G. Rose-Petruck, "High-average-power 2 kHz laser for generation of ultrashort x-ray pulses" Opt. Lett. 27 (11), 963 (2002).

24. C. G. Serbanescu, J. A. Chakera, and R. Fedosejevs, "Efficient K_α X-ray source from submillijoule femtosecond laser pulses operated at kilohertz repetition rate" Rev. Sci. Instrum. 78, 103502 (2007).

25. A. Rousse, P. Audebert, J. P. Geindre, F. Fallies, J. C. Gauthier, A. Mysyrowicz, G. Grillon, and A. Antonetti, "Efficient K_α x-ray source from femtosecond laser-produced plasmas" Phys. Rev. E 50, 2200-2207 (1994)

26. L. M. Chen, P. Forget, S. Fourmaux, J. C. Kieffer, A. Krol, C. C. Chamberlain, B. X. Hou, J. Nees, and G. Mourou, "Study of hard x-ray emission from intense femtosecond Ti:sapphire laser-solid target interactions" Phys. Plasmas 11, 4439 (2004)

27. H.-S. Park, N. Izumi, M. H. Key, J. A. Koch, O. L. Landen, P. K. Patel. T. W. Phillips, and B. B. Zhang, "Characteristics of high energy K_α and Bremsstrahlung sources generated by short pulse petawatt lasers" Rev. Sci. Instrum. 75, 4048 (2004)

28. A. Krol, A. Ikhlef, J. C. Kieffer, D. A. Bassano, C. C. Chamberlain, Z. Jiang, H. Pepin, and S. C. Prasad, "Laser- based microfocused X-ray source for mammography: Feasibility study" Med. Phys. 24, 725 (1997).

29. D. Strickland and G. Mourou, "Compression of amplified chirped optical pulses", Opt. Commun. 56, 219 (1985)

30. G. Korn, A. Thoss, H. Stiel, U. Vogt, M. Richardson, and T. Elsaesser, "Ultrashort 1-kHz laser plasma hard X-ray source" Optics Letters, 27, 866-868 (2002)

31. S. C. Wilks, W. L. Kruer, M. Tabak and A. B. Langdon, “Absorption of Ultra-Intense Laser Pulses” Phys. Rev. Lett. 69, 1383 (1992).

32. X. Liu and D. Umstadter, “Competition between Ponderomotive and Thermal Forces in Short-Scale-Length Laser Plasmas” Phys. Rev. Lett. 69, 1935 (1992).

33. J. C. Kieffer, P. Audebert, M. Chaker, J. P. Matte, H. Pépin, T. W. Johnston, P. Maine, D. Meyerhofer, J. Delettrez, D. Strickland, P. Bado, G. Mourou, “Short-Pulse Laser Absorption in Very Steep Plasma Density Gradients” Phys. Rev. Lett. 62, 760 (1989).

34. P. Mora, “Theoretical Model of Absorption of Laser Light by a Plasma” Phys. Fluids 25, 1051 (1982).

35. R. Fedosejevs, R. Ottmann, R. Sigel, G. Kühnle, S. Szatmari and F. P. Schäfer, Absorption of Femtosecond Laser Pulses in High-Density Plasma, Phys. Rev. Lett. 64, 1250 (1990).

36 . W. L. Kruer, “The Physics of Laser Plasma Interaction” Westview Press, Oxford (2003)

37. F. Brunel, “Not-So-Resonant, Resonant Absorption” Phys. Rev. Lett. 59 (1), 52-55 (1987)

38. S. C. Wilks, W. L. Kruer, “Absorption of ultrashort, ultra-intense laser light by solids and overdense plasmas” IEEE Journal of Quantum Electronics, 33, 1954-1968 (1997)

39. A. Pukhov and J. Meyer-ter-Vehn, “Laser Hole Boring into Overdense Plasma and Relativistic Electron Currents for Fast Ignition of ICF Targets” Phys. Rev. Lett. 79, 2686 - 2689 (1997)

40. D. D. Meyerhofer, H. Cheq, J. A. Delettrez, B. Soom, S. Uchida, and B. Yaakobi, “Resonance Absorption in High-Intensity Contrast, Picosecond Laser-Plasma Interactions” Phys. Fluids B 5, 2584 (1993).

41. M. K. Grimes, A. R. Rundquist, Y. S. Lee and M. C. Downer, “Experimental Identification of "Vacuum Heating" at Femtosecond-Laser-Irradiated Metal Surfaces” Phys. Rev. Lett. 82, 4010 (1999).

42. C. T. Hansen, S. C. Wilks, and P. E. Young, “Spectral Evidence for Collisionless Absorption in Subpicosecond Laser-Solid Interactions” Phys. Rev. Lett. 83, 5019 (1999).

43. Susanne Pfalzner “An Introduction to Inertial Confinement Fusion” Taylor & Francis, New York, (2006)

44. V. L. Ginsburg, “Propagation of Electromagnetic Waves in Plasmas” Gordon and Breach, New York, (1960)

45. S. Eliezer, “The Interaction of High-Power Lasers with Plasmas” Institute of Physics Pub., Bristol (2002)

46. R. Fedosejevs, R. Ottmann, R. Sigel, G. Kühnle, S. Szatmari, and F. P. Schäfer, “Absorption of subpicosecond ultraviolet laser pulses in high-density plasma” Applied Physics B: Lasers and Optics 50, 79 (1990)

47. S. Kato, B. Bhattacharyya, A. Nishiguchi and K. Mina, “Wave Breaking and Absorption Efficiency for Short Pulse P-Polarized Laser Light in a Very Steep Density Gradient” Phys. Fluids B 5, 564 (1993).

48. P. Gibbon and A. R. Bell, “Collisionless Absorption in Sharp-Edged Plasmas” Phys. Rev. Lett. 68, 1535 (1992).

49. P. Gibbon, “Efficient Production of Fast Electron from Femtosecond Laser Interaction with Solid Targets” Phys. Rev. Lett. 73, 664 (1994).

50. J. Denavit, “Absorption of High-Intensity Subpicoseconds Lasers on Solid Density Targets” Phys. Rev. Lett. 69, 3052 (1992).

51. Q. L. Dong, J. Zhang and H. Teng, “Absorption of Femtosecond Laser Pulses in Interaction with Solid Targets” Phys. Rev. E 64, 026411 (2001).

52. P. Gibbon, “Short Pulse Laser Interactions with Matter-An Introduction” Imperial College Press, London (2005)

53. T. P. Hughes, “Laser light in plasmas” Laser-plasma interactions: proceedings of the Twentieth Scottish Universities Summer School in Physics, St. Andrews, edited by R.A. Cairns and J.J. Sanderson, August (1979)

54. L. A. Gizzi, D. Giulietti, A. Giulietti, P. Audebert, S. Bastiani, J. P. Geindre, and A. Mysyrowicz, “Simultaneous Measurements of Hard X Rays and Second-Harmonic Emission in fs Laser-Target Interactions” Phys. Rev. Lett. 76, 2278 - 2281 (1996)

55. A. Bergmann, P. Mulser, “Breaking of resonantly excited electron plasma waves” Phys. Rev. E 47, 3585 (1993)

56. T. Tajima and J. Dawson, “Laser Electron Accelerator”, Phys. Rev. Lett. 43, 267 (1979)

57. S. P. D. Mangles, C. D. Murphy, Z. Najmudin, A. G. R. Thomas, J. L. Collier, A. E. Dangor, E. J. Divall, P. S. Foster, J. G. Gallacher, C. J. Hooker, D. A. Jaroszynski, A. J. Langley, W. B. Mori, P. A. Norreys, F. S. Tsung, R. Viskup, B. R. Walton and K. Krushelnick, “Monoenergetic beams of relativistic electrons from intense laser-plasma interactions." Nature 431, 535 (2004)

58. C. G. R. Geddes, Cs. Toth, J. van Tilborg, E. Esarey, C. B. Schroeder, D. Bruhwiler, C. Nieter, J. Cary and W. P. Leemans “High-quality electron beams from a laser wakefield accelerator using plasma-channel guiding”, Nature 431, 538 (2004)

59. J. Faure, Y. Glinec, A. Pukhov, S. Kiselev, S. Gordienko, E. Lefebvre, J.-P. Rousseau, F. Burgy and V. Malka “A laser–plasma accelerator producing monoenergetic electron beams” Nature 431, 541(2004)

60. Hiroaki Nishimura, “X-Ray Sources” Series in Plasma Physics Applications of Laser–Plasma Interactions edited by Shalom Eliezer, Kunioki Mima CRC press, Taylor and Francis Group 2008

61. M. Tabak, J. Hammer, M. E. Glinsky, W. L. Kruer, S. C. Wilks, J. Woodworth, E. M.

Campbell, M.D. Perry, and R. J. Mason, “Ignition and high gain with ultra-powerful lasers” Phys. Plasmas, 1, 1626, (1994)

62. P.P. Rajeev, S. Banerjee, A.S. Sandhu, R.C. Issac, L.C. Tribedi, and G.R. Kumar, “Role of surface roughness in hard-x-ray emission from femtosecond-laser-produced copper plasmas” Phys. Rev. A 65, 52903 (2002)

63. D. W. Forslund, J. M. Kindel, and K. Lee, “Theory of Hot-Electron Spectra at High Laser Intensity” Phys. Rev. Lett. 39, 284-288 (1977)

64. F.N. Beg, A.R. Bell, A.E. Dangor, C.N. Danson, A.P. Fews, M.E. Glinsky, B.A .Hammel, P. Lee, P.A. Norreys, and M. Tatarakis. "A study of picosecond laser-solid interactions up to 1019 Wcm-2" Physics of Plasmas 4, 447 (1997).

65. L. M. Chen, M. Kando, M. H. Xu, Y. T. Li, J. Koga, M. Chen, H. Xu, X. H. Yuan, Q. L. Dong, Z. M. Sheng,S.V. Bulanov, Y. Kato, J. Zhang, and T. Tajima, "Study of X-Ray Emission Enhancement via a High-Contrast Femtosecond Laser Interacting with a Solid Foil" Phys. Rev. Lett. 100, 045004 (2008)

66. C.L. Rettig, W.M. Roquemore, J.R. Gord, "Efficiency and scaling of an ultrashort-pulse high-repetition-rate laser-driven X-ray source" Appl. Phys. B 93, 365 (2008)

67. B. Hou, J. Nees, A. Mordovanakis, M. Wilcox, G. Mourou, L.M. Chen, J.-C. Kieffer, C.C. Chamberlain and A. Krol, "Hard X-ray generation from solids driven by relativistic intensity in the lambda-cubed regime" Appl. Phys. B 83, 81 (2006)

68. B. Hou, J. A. Nees, W. Theobald, G. A. Mourou, L. M. Chen , J. C. Kieffer, A. Krol and C. C. Chamberlain, "Dependence of hard x-ray yield on laser pulse parameters in the wavelength-cubed regime" Appl. Phys. Lett. 84, 2259 (2004)

69. P. P. Rajeev, P. Taneja, P. Ayyub, A. S. Sandhu, and G. Ravindra Kumar, "Metal Nanoplasmas as Bright Sources of Hard X-Ray Pulses" Phys. Rev. Lett. 90, 115002 (2003)

70. N. Zhavoronkov, Y. Gritsai, M. Bargheer, M. Woerner, T. Elsaesser, F. Zamponi, I. Uschmann, and E. Förster, "Microfocus Cu Kα source for femtosecond x-ray science" Optics Letters, 30, 1737 (2005)

71. Y. T. LI, X. H. Yuan, M. H. Xu, Z.Y. Zheng, Z. M. Sheng, M. Chen, Y. Y. Ma, W. X. Liang, Q. Z. Yu, Y. Zhang, F. Liu, Z. H. Wang, Z.Y. Wei, W. Zhao, Z. Jin, and J. Zhang, "Observation of a Fast Electron Beam Emitted along the Surface of a Target Irradiated by Intense Femtosecond Laser Pulses" Phys. Rev. Lett. 96, 165003 (2006)

72. F. Zamponi, Z. Ansari, C. v. Korff Schmising, P. Rothhardt, N. Zhavoronkov, M. Woerner, T. Elsaesser, M. Bargheer, T. Trobitzsch-Ryll and M. Haschke, "Femtosecond hard X-ray plasma sources with a kilohertz repetition rate" Appl Phys A 96, 51 (2009)

73. K. Liao, A. G. Mordovanakis, B. Hou, G. Chang, M. Rever, G. A. Mourou, J. Nees, and A. Galvanauskas, "Generation of hard X-rays using an ultrafast fiber laser system," Optics Express 15, 13942 (2007)

74. S. Fourmaux, C. Serbanescu, R. E. Kincaid Jr., A. Krol and J. C. Kieffer, "Kα x-ray emission characterization of 100 Hz, 15 mJ femtosecond laser system with high contrast ratio" Appl. Phys. B 94, 569 (2009)

75. H. Chen, B. Soom, B. Yaakobi, S. Uchida, and D. D. Meyerhofer, "Hot-electron characterization from K_ measurements in high-contrast, p-polarized, picosecond laser-plasma interactions" Phys. Rev. Lett. 70, 3431 - 3434 (1993)

76. S. Bastiani, A. Rousse, J. P. Geindre, P. Audebert, C. Quoix, G. Hamoniaux, A. Antonetti, and J. -C. Gauthier, "Experimental study of the interaction of subpicosecond laser pulses with solid targets of varying initial scale lengths" Phys. Rev. E 56, 7179 - 7185 (1997)

77. D. C. Eder , G. Pretzler, E. Fill, K. Eidmann, A. Saemann, "Spatial characteristic of Kα radiation from weakly relativistic laser plasmas" Applied Physics B 70, 211-217 (2000)

78. M Schnürer, R Nolte, T Schlegel, M P Kalachnikov, P V Nickles, P Ambrosi and W Sandner, "On the distribution of hot electrons produced in short-pulse laser – plasma interaction" J. Phys. B 30, 4653 (1997)

79. J. Yu, Z. Jiang, and J. C. Kieffer, A. Krol, "Hard X-ray emission in high intensity femtosecond laser–target interaction" Phys. Plasmas 6, 1318 (1999)

80. U. Teubner, I. Uschmann, P. Gibbon, D. Altenbernd, and E. Förster, T. Feurer, W. Theobald, and R. Sauerbrey, G. Hirst, M. H. Key, J. Lister, and D. Neely, "Absorption and hot electron production by high intensity femtosecond uv-laser pulses in solid targets" Phys. Rev. E 54, 4167 - 4177 (1996)

81. G. Pretzler, Th. Schlegel, and E. Fill, D. Eder, "Hot-electron generation in copper and photopumping of cobalt" Phys. Rev. E 62, 5618 - 5623 (2000)

82. J. D. Kmetec, C. L. Gordon, III, J. J. Macklin, B. E. Lemoff, G. S. Brown, and S. E. Harris "MeV X-ray generation with a femtosecond laser" Phys. Rev. Lett. 68, 1527 - 1530 (1992)

83. M. Schnürer, R. Nolte, A. Rousse, G. Grillon, G. Cheriaux, M. P. Kalachnikov, P. V. Nickles, and W. Sandner, "Dosimetric measurements of electron and photon yields from solid targets irradiated with 30 fs pulses from a 14 TW laser" Phys. Rev. E 61, 4394 - 4401 (2000)

84. Ch. Reich, P. Gibbon, I. Uschmann and E. Forster, "Yield Optimization and Time Structure of Femtosecond Laser Plasma Kα Sources" Phys. Rev. Lett. 84, 4846 (2000)

85. D. Salzmann, Ch. Reich, I. Uschmann, and E. Forster, "Theory of Kα generation by femtosecond laser-produced hot electrons in thin foils" Phys. Rev. E 65, 036402 (2002)

86. F. Ewald, H. Schwoerer and R. Sauerbrey, "Kα-radiation from relativistic laser-produced plasmas" Europhys. Lett. 60 710 (2002)

87. M. Silies, H. Witte, S. Linden, J. Kutzner, I. Uschmann, E. Förster and H. Zacharias, Table-top kHz hard X-ray source with ultrashort pulse duration for time-resolved X-ray diffraction Appl. Phys. A 96, 59 (2009)

88. J. Kutzner, H. Witte, M. Silies, T. Haarlammert, J. Huve, G. Tsilimis, I. Uschmann, E. Forster and H. Zacharias, "Laser-based, high repetition rate, ultrafast X-ray source" Surf. Interface Anal. 38, 1083 (2006)

89. W. Lu, M. Nicoul, U. Shymanovich, A. Tarasevitch, P. Zhou, K. Sokolowski-Tinten, and D. von der Linde, "Optimized Kα X-ray flashes from femtosecond-laser-irradiated foils" Phys. Rev. E 80, 026404 (2009)

90. H.-S. Park, D. M. Chambers, H.-K. Chung, R. J. Clarke, R. Eagleton, E. Giraldez, T. Goldsack, R. Heathcote, N. Izumi, M. H. Key, J. A. King, J. A. Koch, O. L. Landen, A. Nikroo, P. K. Patel, D. F. Price, B. A. Remington, H. F. Robey,R. A. Snavely, D. A. Steinman, R. B. Stephens, C. Stoeckl, M. Storm, M. Tabak, W. Theobald, R. P. J. Town, J. E. Wickersham, and B. B. Zhang, "High-energy Kα radiography using high-intensity, short-pulse lasers" Physics of plasmas 13, 056309 (2006)

91. Ch. Ziener, I. Uschmann, G. Stobrawa, Ch. Reich, P. Gibbon, T. Feurer, A. Morak, S. Dusterer, H. Schwoerer, E. Forster, and R. Sauerbrey, "Optimization of Kα bursts for photon energies between 1.7 and 7 keV produced by femtosecond-laser-produced plasmas of different scale length" Phys. Rev. E 65, 066411 (2002)

92. F. Y. Khattak, E. Garcia Saiz, T. Dzelzainis, D. Riley and Z. Zhai, "Scale-length optimizing of short pulse Cu K□ laser-plasma sources" Applied physics letters 90, 081502 (2007)

93. NIST database: Tables of X-Ray Mass Attenuation Coefficients and Mass Energy- Absorption Coefficients
http://physics.nist.gov/PhysRefData/XrayMassCoef/cover.html

94. http://henke.lbl.gov/optical_constants/

95. http://www.amptek.com/anczt1.html

96. http://www.lot-oriel.com/site/site_down/cc_do420_deen02.pdf

97. C. G. Serbanescu, J. Santiago and R. Fedosejevs, "Micro X-ray Sources from Femtosecond Laser Plasmas" SPIE 5196, 344-351 (2003)

98. L. M. Chen, M. Kando, J. Ma, H. Kotaki, Y. Fukuda, Y. Hayashi, I. Daito, T. Homma, K. Ogura, M. Mori, A. S. Pirozhkov, J. Koga, H. Daido, S. V. Bulanov,b_ T. Kimura, T. Tajima, and Y. Kato, "Phase-contrast x-ray imaging with intense Ar Kα radiation from femtosecond-laser-driven gas target" Applied physics letters 90, 211501 (2007).

99. A. Snigirev, I. Snigireva, V. Kohn, S. Kuznetsov, and I. Schelokov, "On the possibilities of x-ray phase contrast microimaging by coherent high-energy synchrotron radiation", Rev. Sci. Instr. 66 5486 (1995).